
The full shape of the large-scale galaxy power spectrum: modelling and cosmological implications

Francesco Montesano



München 2011

The full shape of the large-scale galaxy power spectrum: modelling and cosmological implications

Francesco Montesano

Dissertation
an der Physik
der Ludwig–Maximilians–Universität
München

vorgelegt von
Francesco Montesano
aus Varese, Italien

München, den 21. Juli 2011

Erstgutachter: Prof. Dr. Ralf Bender

Zweitgutachter: Prof. Dr. Hans Böhringer

Tag der mündlichen Prüfung: 28. Oktober 2011

Contents

Zusammenfassung	xi
Abstract	xiii
1 Introduction	1
2 General relativity and cosmology	5
2.1 Homogeneous and isotropic universe	5
2.2 Cosmological perturbation theory	9
3 Observational evidence	17
3.1 Large Scale Structure	17
3.2 Additional observations	23
3.2.1 Type Ia supernovae	23
3.2.2 Hubble parameter	25
3.2.3 Cosmic microwave background	26
3.3 Combining experiments	27
4 A new model for the full shape of the matter power spectrum	29
4.1 N-body simulations and the computation of the power spectrum	29
4.1.1 The L-BASICC II N-Body simulations	29
4.1.2 Power spectrum computation and shot noise	30
4.2 Modelling the full shape of the power spectrum	32
4.3 Model in practice and discussion	35
4.3.1 Testing the model	35
4.3.2 Non-linear evolution	37
4.3.3 Redshift space distortions	41
4.3.4 Halo bias	43

5	Cosmological Parameters	49
5.1	The galaxy sample and the mock catalogues.	49
5.1.1	The luminous red galaxy sample from the 7th data release of SDSS	49
5.1.2	The mock catalogues	51
5.2	The power spectra	52
5.2.1	The LRG power spectrum	52
5.2.2	The mock power spectra and covariance matrix	53
5.3	Methodology	55
5.3.1	Parameter spaces	55
5.3.2	Practical issues	57
5.3.3	Testing the model	58
5.4	Results: the cosmological parameters	61
5.4.1	The concordance cosmology	61
5.4.2	Curvature	65
5.4.3	Beyond the cosmological constant	68
5.4.4	Curvature and dark energy equation of state as free parameters . .	70
5.4.5	Time varying dark energy equation of state parameter	72
5.5	Comparison with previous studies	75
6	Conclusion and outlook	79
A	Power spectrum	83
A.1	Fast Fourier transform and corrections	83
A.2	The galaxy power spectrum	85
B	Impact of weights on power spectra and cosmological constraints	89
B.1	Testing the luminous red galaxies power spectrum	89
B.2	Testing the power spectra of the mock catalogues	92
B.3	Impact on the cosmological parameters	93
	Bibliography	95
	Aknowledgments	109

List of Figures

2.1	Time evolution of the Universe	8
2.2	Standard versus renormalized perturbation theory	14
3.1	Galaxy correlation function and power spectrum	22
3.2	SNIa luminosity-distance relation	24
3.3	WMAP7: CMB map and angular power spectrum	26
3.4	Cosmological constraints combining experiments	28
4.1	Exclusion effect in the correlation function and in the power spectrum. . .	32
4.2	Linear and first loop power spectra.	34
4.3	Real space dark matter correlation matrix at $z = 0, 0.5$ and 1	36
4.4	Real space total halo sample correlation matrix at $z = 0, 0.5$ and 1	37
4.5	Dark matter real and redshift space power spectra.	38
4.6	Dark matter real and redshift space power spectra divided by a smooth reference one.	38
4.7	Constraints on α as function of the k_{\max}	39
4.8	$k_{\star} - \alpha$ 2D marginalised constraints for dark matter at $z = 0, 0.5$ and 1 . . .	40
4.9	$k_{\star} - A_{\text{MC}}$ 2D marginalised constraints for dark matter at $z = 0, 0.5$ and 1 . .	41
4.10	Halo real and redshift space power spectra at $z = 0$ divided by a smooth reference one.	45
4.11	$k_{\star} - \alpha$ 2D marginalised constraints for the haloes at $z = 0$	46
5.1	Footprint of the LRG sample	50
5.2	Radial distribution of the LRG sample	50
5.3	LRG power spectrum and window matrix	54
5.4	LasDamas power spectrum	55
5.5	LasDamas correlation matrix	56
5.6	LasDamas: constraints on the model parameters as function of k_{\max}	59
5.7	LasDamas: $k_{\star} - \alpha$ 2D marginalised constraints	60
5.8	wCDM: cosmological parameters constraints as function of k_{\max}	61
5.9	Λ CDM: $\Omega_{\text{M}} - H_0$ and $\Omega_{\text{M}} - \sigma_8$ 2D marginalised constraints	63

5.10	k Λ CDM: $\Omega_{\text{DE}} - \Omega_{\text{M}}$ 2D marginalised constraints	66
5.11	k Λ CDM: $\Omega_{\text{DE}} - H_0$ 2D marginalised constraints	67
5.12	wCDM: $\Omega_{\text{DE}} - w_{\text{DE}}$ 2D marginalised constraints	69
5.13	kwCDM: $w_{\text{DE}} - \Omega_{\text{k}}$ and $w_{\text{DE}} - \Omega_{\text{DE}}$ 2D marginalised constraints	72
5.14	waCDM: $w_0 - w_{\text{a}}$ and $w_0 - \Omega_{\text{DE}}$ 2D marginalised constraints	74
5.15	waCDM: $w_{\text{DE}}(z)$	75
A.1	Ratio of power spectra computed with FFT and standard FT.	86
B.1	Test of the LRG power spectrum against p_{w} , w_{i} and estimator	90
B.2	Test of the LRG window function against p_{w} , w_{i} and estimator	91
B.3	Test of the LasDamas power spectrum against p_{w}	92
B.4	Test of the LasDamas covariance matrices against p_{w}	93

List of Tables

4.1	Cosmological parameters and specifications of the L-BASICC II simulations.	30
4.2	Mass limits of the halo sub catalogues	30
4.3	Number of haloes and shot noise amplitude at $z = 0, 0.5$ and 1	31
4.4	One-dimensional constraints on the stretch factor α	40
4.5	Theoretical and recovered large scale bias and Kaiser boost factors.	43
5.1	Cosmological parameters and specifications of the LasDamas simulations .	51
5.2	Prior ranges for the fundamental cosmological and the model parameters .	57
5.3	Λ CDM: 1D marginalised constraints	62
5.4	Λ CDM: 1D marginalised constraints with alternative SNIa samples	64
5.5	k Λ CDM: 1D marginalised constraints	65
5.6	wCDM: 1D marginalised constraints	67
5.7	wCDM: 1D marginalised constraints with alternative SNIa samples	70
5.8	kwCDM: 1D marginalised constraints	71
5.9	waCDM: 1D marginalised constraints	73

Zusammenfassung

Die dunkle Energie, die ungefähr 73% der gesamten Energiedichte des Universums ausmacht und dessen Ausdehnung beschleunigt, ist eines der größten ungelösten Probleme der modernen Physik. Auf ihre Natur kann aus ihrem Einfluss auf die Entwicklung des Universums und das Strukturwachstum geschlossen werden, welches die Verteilung von Galaxien und Gas auf kosmologischen Maßstäben beeinflusst. Akkurate Modelle, die die Effekte von nicht-linearer Entwicklung, Bias und Rotverschiebungsverzerrungen mit einbeziehen, sind notwendig, um präzise Informationen aus dem großskaligen Leistungsspektrum der Galaxien abzuleiten. In dieser Dissertation präsentiere ich ein Modell des Leistungsspektrums, das mithilfe von 50 Simulationen der Dunklen Materieverteilung getestet wird. Die Ergebnisse zeigen, dass dieses einfache Modell eine akkurate Beschreibung des Leistungsspektrums für $k \lesssim 0.15 h \text{ Mpc}^{-1}$ sowohl der Dunklen Materie als auch der Halos, im reellen und im Rotverschiebungsraum, darstellt. Obwohl das Modell nur auf großen Skalen Gültigkeit besitzt, ist die Bestimmung der Zustandsgleichung der Dunklen Energie w_{DE} präziser, als wenn nur die Baryonischen akustischen Oszillationen alleine berechnet werden, und die in der Form des Leistungsspektrums beinhaltete Information vernachlässigt wird. Das Modell wird dann auf das Leistungsspektrum von circa 90000 hellen roten Galaxien (LRGs) aus den 7646 deg^2 der nördlichen Galaktischen Hemisphäre der siebten Datenveröffentlichung des Sloan Sky Digital Survey angewandt. Die Fehler und die Korrelationsmatrizen werden aus den 160 LasDamas Katalogen gerechnet, welche die LRGs und die Geometrie der Himmelsdurchmusterung simulieren. Um kosmologische Parameter in fünf verschiedenen Parameterräumen zu messen, benutze ich die LRG Verteilung zusammen mit der neuesten Messung von Temperatur- und Polarisationsfluktuationen im kosmischen Mikrowellenhintergrund, die Relation zwischen Leuchtkraft und Distanz von Typ 1a Supernovae, und die präzise Messung des lokalen Hubble Parameters. Die Analyse zeigt, dass unser Universum geometrisch flach ist und dass es aus 4% Baryonen, 23% Dunkler Materie und 73% Dunkler Energie besteht. Ich messe $w_{\text{DE}} = -1.025^{+0.066}_{-0.065}$ ohne Zeitsabhängigkeit: das ist vereinbar mit einer Kosmologischen Konstante. In den nächsten Jahren werden neue Experimente die Verteilung der Galaxien mit viel höherer Präzision, als es heutzutage möglich ist, messen und Modelle, wie das hier benutzte, werden erlauben, das gesamte Potenzial von Beobachtungen auszunutzen, um akkurate Bestimmungen der kosmologischen Parameter zu erhalten.

Abstract

Dark energy, which constitutes about 73% of the total energy density and causes the Universe expansion to accelerate, is one of the most important open problems in physics. The nature of dark energy can be inferred from its effects on the evolution of the Universe and the growth of structures as it influences the distribution of galaxies and gas at cosmological scales at low and intermediate redshifts. To extract unbiased information from the large scale galaxy power spectrum, accurate models, encoding the distortions due to non-linear evolution, bias and redshift space distortions, are needed. In this thesis I present a model for the full shape of the power spectrum and test its validity against a suite of 50 large volume, moderate resolution N-body dark matter simulations. My results indicate that this simple model provides an accurate description of the full shape of the dark matter and halo power spectrum, both in real and redshift space, for $k \lesssim 0.15 h \text{ Mpc}^{-1}$. Even though its application is restricted to large scales, this prescription can provide tighter constraints on the dark energy equation of state parameter w_{DE} than those obtained by modelling the baryonic acoustic oscillations signal only, where the information of the broad-band shape of the power spectrum is discarded. I then apply this model to a measurement of the power spectrum of the distribution of about 90000 luminous red galaxies (LRGs) across 7646 deg² in the Northern Galactic Cap from the seventh data release of the Sloan Sky Digital Survey. The errors and mode correlations are estimated from the 160 LasDamas mock catalogues, created in order to simulate the LRG galaxies and the survey geometry. Using the galaxy distribution, in combination with the latest measurement of the temperature and polarisation anisotropy in the cosmic microwave background, the luminosity-distance relation from the largest available type 1a supernovae dataset and a precise determination of the local Hubble parameter, I obtain cosmological constraints for five different parameter spaces. The analysis performed in this thesis shows that the Universe is geometrically flat and composed by about 4% of baryons, 23% of cold dark matter and 73% of dark energy. I measure w_{DE} to be $-1.025^{+0.066}_{-0.065}$ without any evidence of time dependence, which is compatible with a cosmological constant. In the next years new experiments will allow to measure the clustering of galaxies with a precision much higher than today, and models like the one used here will provide valuable tools in order to achieve the full potentials of the observations and obtain unbiased constraints on the cosmological parameters.

Chapter 1

Introduction

The publication of the equations of general relativity (Einstein, 1915, 1916) revolutionised our understanding of the nature of gravitation and of the Universe. Their first cosmological solutions, together with the realisation that galaxies are large objects outside the Milky Way and receding from us, (e.g., Einstein, 1917; Friedmann, 1922; Opik, 1922; Friedmann, 1924; Lemaître, 1927; Hubble, 1929) showed that our Universe is not static but expanding.

Just before the second world war, Zwicky (1937) proved that the mass associated to light in clusters of galaxies is much smaller than the one inferred from dynamics. This showed that standard, light emitting matter, usually referred to as *baryons*, only constitutes about 15% of the gravitational matter and that the majority of it is *dark matter*. In the last decade of the 20th century, it became evident that dark and ordinary matter were insufficient to describe accurately a variety of cosmological observations. It was at the end of that decade that the relation between luminosity and distance of Type 1a supernovae (SNIa) revealed that in the Universe about 73% of the total energy density comes from an extra component, which causes the cosmic expansion to accelerate (Riess et al., 1998; Perlmutter et al., 1999). The combination of SNIa observations (see Kowalski et al., 2008; Amanullah et al., 2010, for more recent results) with other independent experiments, like the measurements of the temperature fluctuations in the cosmic microwave background (CMB, e.g. Hinshaw et al., 2003; Spergel et al., 2003, 2007; Komatsu et al., 2009, 2011), the analysis of distribution of the galaxies on large scales (e.g. Efstathiou et al., 2002; Percival et al., 2002; Tegmark et al., 2004; Eisenstein et al., 2005; Sánchez et al., 2006, 2009; Percival et al., 2010; Reid et al., 2010a; Blake et al., 2011) and the number density of clusters as function of mass (e.g., Vikhlinin et al., 2009), draw a picture of a nearly flat universe dominated by an exotic component, called *dark energy*, with about 23% of the total energy content in the form of dark matter and with only 4% of baryons.

The nature of dark energy is one of the most important open problems in physics today and its understanding has deep implications in the comprehension of the fundamental laws of nature. The most basic model of dark energy describes it as a *cosmological constant* Λ , for which density and pressure are constant and related by the *equation of state* parameter $w_\Lambda = p_\Lambda/\rho_\Lambda = -1$. The only known mechanism that can produce a cosmological constant

is the *vacuum energy*, but its density is, with a cut-off at the Planck scale, about 120 orders of magnitude larger than the measured one. A large number of alternative models has been explored in recent years. They are mostly separated in two groups: one where dark energy is modelled as an evolving field, like *quintessence* (for reviews see, e.g., Peebles & Ratra, 2003; Copeland et al., 2006), the other in which the equations of general relativity are modified in order to describe the acceleration as a dynamic effect (for a review see, e.g., Tsujikawa, 2010).

Many present day and future galaxy redshift surveys, like the Baryonic Oscillation Spectroscopic Survey (BOSS, Schlegel et al., 2009; Eisenstein et al., 2011), the Panoramic Survey Telescope & Rapid Response System (Pan-STARRS, Kaiser et al., 2002), the Dark Energy Survey (DES, Abbott et al., 2005), the Hobby Eberly Telescope Dark Energy Experiment (HETDEX, Hill et al., 2004) and, on a longer time scale, the space based Euclid mission (Laureijs, 2009), have been designed to constrain the dark energy equation of state parameter and its time evolution with very high accuracy. Some of these surveys are also optimised to measure the *baryonic acoustic oscillations* (BAO), a signature imprinted in the galaxy distribution by the acoustic fluctuations in the baryon-photon fluid in the young and hot universe.

In this work I will concentrate on the distribution of galaxies on large scales as a means to study the evolution and composition of the universe. The *large scale structure* of the universe (LSS) is usually analysed statistically, in particular through the two-point correlation function and its Fourier transform the power spectrum. Cosmological information is extracted from the broad band shape of those functions as well as the BAOs. The latter shows up in the power spectrum as a quasi-harmonic series of damped oscillations at wave numbers $0.01 h \text{ Mpc}^{-1} \lesssim k \lesssim 0.4 h \text{ Mpc}^{-1}$ (Sugiyama, 1995; Eisenstein & Hu, 1998, 1999), and in the two-point correlation function as a unique broad and quasi-gaussian peak at scales $r \sim 100 - 110 h^{-1} \text{ Mpc}$ (Matsubara, 2004). The BAOs were first detected in the correlation function of the *luminous red galaxies* (LRG) sample drawn from the Sloan Digital Sky Survey (SDSS) by Eisenstein et al. (2005) and the power spectrum of the two-degree Field Galaxy Redshift Survey (2dFGRS) by Cole et al. (2005). The BAO feature has been object of intensive studies as a powerful tool to probe the geometry of the Universe. The acoustic scale is related to the sound horizon scale at the *drag epoch*, i.e. when the baryons were released from the photons. Because of the very high photon to baryon ratio, this happened slightly later than the epoch in which these two components decoupled (Komatsu et al., 2009). As this scale depends only on the plasma physics after the big bang and can be calibrated using CMB data, it is in principle possible to use the BAO scale as a standard ruler. Measuring the apparent size of the BAO in the directions parallel and perpendicular to the line of sight, it is possible to measure the redshift dependence of the Hubble parameter H and the angular diameter distance D_A and thus constrain cosmological parameters (Blake & Glazebrook, 2003; Hu & Haiman, 2003; Linder, 2003; Seo & Eisenstein, 2003; Wang, 2006; Guzik et al., 2007; Seo & Eisenstein, 2007; Seo et al., 2008; Shoji et al., 2009; Seo et al., 2010; Percival et al., 2010). It has been shown, however, that the use of the BAOs alone comes at the price of discarding important information encoded in the broad band shape of the power spectrum and correlation function (Sánchez

et al., 2008; Shoji et al., 2009; Blake et al., 2011). For more recent cosmological analyses based on the LSS see, e.g. Percival et al. (2007); Cabré & Gaztañaga (2009a); Gaztañaga et al. (2009); Sánchez et al. (2009); Percival et al. (2010); Reid et al. (2010a); Kazin et al. (2010); Blake et al. (2011); Tinker et al. (2011).

The shape of the power spectrum and of the correlation function, as well as the amplitude and position of the BAO feature (Crocce & Scoccimarro, 2008; Sánchez et al., 2008; Smith et al., 2008), are affected by: i) non-linear evolution of the clustering; ii) bias, caused by the fact that galaxies, that we observe, do not trace perfectly the matter distribution (e.g. McDonald, 2006; Matsubara, 2008b; Jeong & Komatsu, 2009); iii) redshift space distortions, that arise when deriving the distance of an object from its observed redshift, which is the sum of a cosmological part and the doppler shift due to the peculiar velocity of the emitter (e.g. Scoccimarro, 2004; Cabré & Gaztañaga, 2009a,b; Jennings et al., 2011; Reid & White, 2011).

The increasing accuracy and volume of the present day and future galaxy redshift surveys will allow to measure with very high precision the signal from galaxy clustering and the BAO feature. In order to extract unbiased and accurate cosmological information, in particular the characteristics of dark energy, systematic effects and the impact of non-linear evolution, bias and redshift space distortions need to be carefully analysed and modelled. The two main frameworks in which it is possible to model the large scale structure of the universe are the *halo model* (HM, see Cooray & Sheth, 2002, for a review) and *perturbation theory* (PT, see Bernardeau et al., 2002, for a review). Neither PT nor HM are accurate enough for next generation of galaxy surveys. In particular, it has been proved that PT can describe the power spectrum accurately only on very large scales or at high redshift, when contributions up to third order are included (Jeong & Komatsu, 2006, 2009). In the past few years different schemes to improve PT have been proposed. In this work I will concentrate on one of these approaches, *renormalised perturbation theory* (RPT, Crocce & Scoccimarro, 2006a,b). The basic idea of RPT is to reorganise all the contributions in the standard PT such that each term is always positive and dominant in a small range of scales. Matarrese & Pietroni (2007, 2008) proposed a method based on the renormalisation group equations and their findings are analogous to RPT. An alternative approach within PT is to truncate the expansion series and introduce a physically motivated closure equation in order to obtain a closed system (e.g., Pietroni, 2008; Taruya & Hiramatsu, 2008; Taruya et al., 2009), similarly to what is done in fluid dynamics introducing the equation of state. It is possible to improve PT also through the renormalisation of the model parameters, relating them to observable quantities (e.g., McDonald, 2006, 2007; Smith et al., 2009). The analysis of perturbations in Lagrangian space, i.e. following the trajectories of the particles instead of the density and velocity fluctuations (Euclidean approach), leads naturally to a partial resummation of the terms in the standard PT and an improvement over it (Matsubara, 2008a,b).

With the exception of, e.g., Matsubara (2008b) and Taruya et al. (2010), the approaches just introduced can describe the clustering of dark matter only, and it is non trivial to include into the models the effects of bias and redshift space distortions. Because of this, different phenomenological approaches based on some flavour of PT have been developed

in the past years with the goal of introducing in a relatively simple way these effects (e.g., McDonald, 2006; Crocce & Scoccimarro, 2008; Sánchez et al., 2008; Jeong & Komatsu, 2009).

Plan for the thesis

Following this approach, in Chapter 4, I will present a model of the large scale power spectrum inspired by RPT that, with the introduction of few parameters, can describe accurately the the full shape of the two-point statistics when both the bias and redshift space distortions are included. This model is then applied to the power spectrum that I measure from a LRG catalogue. Combining it with information from CMB, SNIa and an independent measurement of the local *Hubble parameter*, I extract tight cosmological constraints.

The basic cosmological concepts and quantities used throughout this work are presented in Section 2.1. Section 2.2 describes briefly the perturbation theory approach and how renormalized perturbation theory can improve it. In Chapter 3 I depict some of the observational evidences that suggested first and confirmed later that the Universe is geometrically close to flat and dominated by a dark energy component. In particular I illustrate the experiments that I use in Chapter 5 to extract cosmological constraints: the large scale structure of the Universe, cosmic microwave background, Type 1a supernovae and the measurement of the local Hubble parameter.

My model for the full shape of the large scale power spectrum is presented and tested in Chapter 4. In Section 4.1 I describe the set of simulations used to check the accuracy of the model and some technical details about the computation of the power spectrum from simulation boxes. The model, based on the approach used for the correlation function by Crocce & Scoccimarro (2008) and Sánchez et al. (2008, 2009), is explained in Section 4.2. Finally in Section 4.3 I describe the tests that I perform against the dark matter and halo power spectra, both in real and redshift space, and I show the range of scales in which the model is accurate and can recover unbiased constraints on the dark energy equation of state parameter.

In Chapter 5 I apply my model to the power spectrum measured from a LRG sample taken from the seventh data release of Sloan Digital Sky Survey (Sections 5.1.1 and 5.2.1). The mock catalogues used in order to estimate the errors and correlations are presented in Section 5.1.2 and their power spectrum and covariance are shown in Section 5.2.2. Sections 5.3.1 and 5.3.2 present the parameter spaces analysed and the procedure that I use to extract cosmological information. Similarly to what is done in Chapter 4, in Section 5.3.3 I test the model against the mock catalogues in order to access the validity of the model also in presence of a complex geometry. In Section 5.4 I combine the power spectrum with the cosmic microwave background, the type Ia supernovae and the measurement of the Hubble parameter and constrain cosmological parameters for the five parameter spaces.

In Chapter 6, I summarise the results of this work and draw my conclusions.

General relativity and cosmology

The theory of *general relativity* (GR, Einstein, 1915, 1916) allowed a new understanding of the nature of gravity and of the history and composition of our Universe (for early studies see e.g., Einstein, 1917; Friedmann, 1922, 1924; Lemaître, 1927). Few years later Hubble (1929) discovered that galaxies are receding from us at a velocity proportional to their distance, which gave observational support to the cosmological theories just developed, that predicted that the Universe was not stationary but expanding. In this chapter I introduce the basic quantities and equations to describe the evolution of a homogeneous and isotropic universe (Section 2.1) and the principal concepts of cosmological perturbation theory (Section 2.2).

2.1 Homogeneous and isotropic universe

The *Copernican principle* states that the Universe is *homogeneous*, i.e. there are no privileged positions, and *isotropic*, i.e. there are no privileged directions. This is clearly non valid at relatively small scales, where matter is distributed in clumps separated by large voids, but the principle holds at extremely large scales, as shown by galaxy number counts and observations of X-ray, γ -ray and the cosmic microwave background (CMB, the latter will be described in Section 3.2.3).

Under these assumptions, the *metric* $g_{\mu\nu}$ is described by the Friedmann-Lemaître-Robertson-Walker (FLRW) one:

$$ds^2 = g_{\mu\nu} dx^\mu dx^\nu = -dt^2 + a^2(t) \left[\frac{dr^2}{1 - kr^2} + r^2 (d\theta^2 + \sin^2 \theta d\phi^2) \right], \quad (2.1)$$

where $a(t)$ is the *scale factor*, t , r , θ and ϕ are the time and the three *comoving spatial* coordinates, i.e. stationary with respect to changes in $a(t)$, in spherical representation and k is the *curvature*. The physical coordinates, which evolve with time, are related to the comoving ones by the scale factor. In this work, the scale factor is normalised to $a = 1$ at present day. The value of k defines whether the geometry is flat ($k = 0$), open ($k = -1$)

or closed ($k = +1$). Through the whole thesis I use the following index conventions: greek indices run over the time (0) and space coordinates (1,2,3), latin indices indicate only space coordinates and repeated indices, one upper and one lower, are summed over. I also use a unit system in which $\hbar = c = k_B = 1$.

The evolution of the universe can be computed inserting the metric from equation (2.1) into the general relativity equation:

$$G_{\mu\nu} = R_{\mu\nu} - \frac{1}{2}g_{\mu\nu}R = 8\pi GT_{\mu\nu}. \quad (2.2)$$

$R_{\mu\nu}$ and $R = g^{\mu\nu}R_{\mu\nu}$ are the *Ricci tensor* and *scalar*, respectively, and are non-linear functions of the metric, G is Newton's constant and $T_{\mu\nu}$ is the *energy-momentum tensor*, that for perfect fluids with density ρ and pressure p has, in the rest frame, the form:

$$T_{\mu}{}^{\nu} = T_{\mu\alpha}g^{\alpha\nu} = \begin{pmatrix} -\rho & 0 & 0 & 0 \\ 0 & p & 0 & 0 \\ 0 & 0 & p & 0 \\ 0 & 0 & 0 & p \end{pmatrix}. \quad (2.3)$$

Solving equation (2.2) with the FLRW metric, it is possible to obtain two coupled differential equations, known as *Friedmann equations*:

$$\left(\frac{\dot{a}}{a}\right)^2 = \frac{8\pi G}{3}\rho - \frac{k}{a^2} \quad (2.4a)$$

and

$$\frac{\ddot{a}}{a} = -\frac{4\pi G}{3}(\rho + 3p). \quad (2.4b)$$

The two equations relate the rate of the expansion or contraction and the acceleration of the universe to the curvature and the densities and pressures of its constituents. The left hand sides of the equation (2.4) are usually parametrized through the *Hubble parameters* $H = \dot{a}/a$ and the *deceleration parameter* $q = -\ddot{a}a/\dot{a}^2$. Often the Hubble parameter is denoted by the dimensionless quantity $h = H/100 \text{ km s}^{-1} \text{ Mpc}^{-1}$.

Densities are commonly indicated by $\Omega_i = \rho_i/\rho_{\text{cr}}$, where the $\rho_{\text{cr}} = 3H_0^2/8\pi G$, dubbed *critical density*, is defined from equation (2.4a) assuming flatness, $k = 0$. With this definition it is easy to see the present day relation between the total density and the curvature:

$$\Omega - 1 = \frac{k}{H_0^2}. \quad (2.5)$$

$\Omega = 1$ if and only if the universe is geometrically flat. Higher and lower values of density requires the geometry to be, respectively, close or open, thus $k = +1$ or $k = -1$. It is also possible to define a density of curvature as $\Omega_k = -k/H_0^2$, with which $\Omega + \Omega_k = 1$ for $a = 1$.

From the time component of the conservation of $T^{\mu\nu}$, or equivalently from combining equations (2.4), it is possible to obtain an equation for the time evolution of the densities:

$$\frac{\dot{\rho}}{\rho} = -3\frac{\dot{a}}{a}\left(1 + \frac{p}{\rho}\right). \quad (2.6)$$

Assuming that pressure and density of each cosmic component are related by an *equation of state* parameter w :

$$p = w\rho, \quad (2.7)$$

equation (2.6) implies a simple evolution of the densities: $\rho_i \propto a^{-3(1+w_i)}$. Assuming the density of the components and the corresponding w_i , it is possible to calculate the curvature and the time evolution of the universe. In the same way from the cosmic history it is possible to infer, assuming the values of equation of state parameter, information regarding densities and curvature.

Observations, some of which are introduced in Chapter 3, show that the Universe is undergoing an accelerated expansion with $H_0 = H(a = 1) \approx 70 \text{ km s}^{-1} \text{ Mpc}^{-1}$ and $q_0 = q(a = 1) < 0$ (Gong & Wang, 2007), is close to geometrically flat ($k \approx 0$) and that the main components are: i) standard matter, referred to in the literature as *baryons*; ii) *dark matter*, that interacts only gravitationally; iii) *radiation*, photons and relativistic particles, and iv) *dark energy*, responsible for the acceleration of the expansion. Baryons and dark matter contribute to about 4% and 23% of the total energy density budget and are composed by non-relativistic particles with $w_b = w_{\text{DM}} = 0$. The sum of baryons and dark matter is usually referred to as *matter* and its density, as well as the one for the two components separately, evolves like $\rho_M \propto a^{-3}$, as expected by the matter conservation in an isolated system. Radiation, being relativistic, has $w = 1/3$ and its density evolves as $\rho_{\text{rad}} \propto a^{-4}$. The extra factor $1/a$ comes from the adiabatic change in the energy of radiation as the volume of the universe changes. This also means that radiation, although now negligible ($\Omega_{\text{rad}} \approx 10^{-4}$), was dominant at early times. The nature of dark energy is one of the most puzzling open problems in modern physics. The simplest model, which agrees with a large range of observations, is that dark energy is described by a *cosmological constant*, Λ , with $w_\Lambda = -1$. Because of this, its density $\rho_\Lambda = \Lambda/8\pi G \approx a^0$ is constant in time. The model just depicted is usually called ΛCDM .

The scale factor is often indicated by the *redshift* $z = \lambda_2/\lambda_1 - 1$, i.e. the change in wavelength of a photon between the emission at time t_1 and its observation at t_2 . Since the energy of a photon, assuming that the emitter and the observer are stationary with respect to their comoving coordinates, scales as the inverse of the scale factor, its wavelength is $\lambda(t) \propto a(t)$. Thus $z = a(t_2)/a(t_1) - 1$ or, if the photon is observed at present time, $z = a^{-1} - 1$, with a the scale factor at emission. Assuming the value of H_0 , the cosmological densities and a generic form of the dark energy equation of state parameter, it is possible to convert redshifts into comoving distances between the emitter and the observer:

$$D_C = \frac{1}{H_0} \int_0^z \frac{dz'}{E(z')} \quad (2.8)$$

with

$$E^2(z) = \Omega_M (1+z)^3 + \Omega_k (1+z)^2 + \Omega_r (1+z)^4 + \Omega_{\text{DE}} \exp \left\{ -3 \int_0^z \frac{dz'}{z'} [1 + w(z')] \right\}. \quad (2.9)$$

In the cosmological constant case, the argument of the exponent in equation (2.9) becomes 0. The time passed from the emission at redshift z , called *look back time*, can be

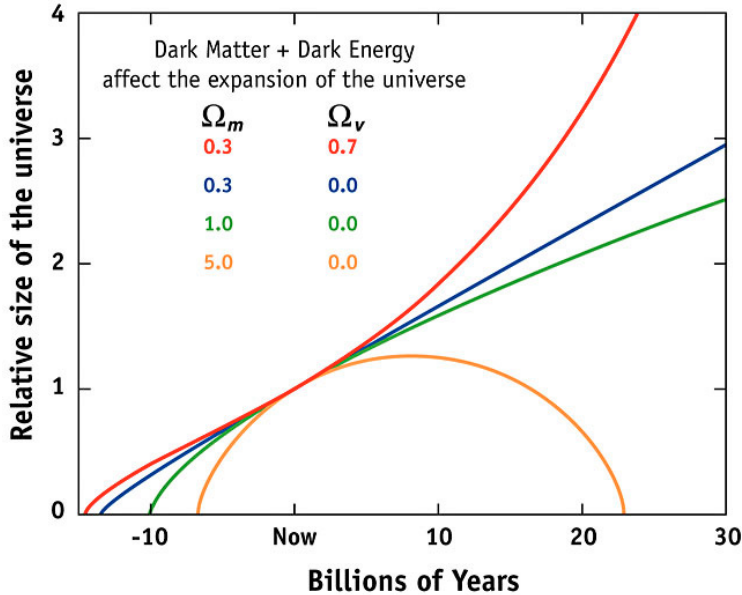


Figure 2.1: Time evolution of the Universe for different values of the density of matter (Ω_m) and cosmological constant (Ω_Λ). The upper line corresponds to a flat Λ CDM universe with 30% of matter and 70% of dark energy. The lower three show the scale factor evolution in open, flat and closed matter dominated scenarios. Figure from: http://map.gsfc.nasa.gov/universe/uni_fate.html

easily computed as $t_L = H_0^{-1} \int_0^z dz' [(1+z') E(z')]^{-1}$. The redshift, which can be in principle measured for each light source, makes it possible to analyse the three dimensional distribution of objects and to obtain the age of the Universe when their light was emitted.

Figure 2.1 shows the time evolution of the scale factor of the universe for four different combinations of matter and dark energy density with the same present day value of H . Given that $H_0 > 0$, all the cases shown began at $a = 0$ with a singularity, the *big bang*, characterised by infinite density and temperature and infinitesimal size. About 10^{-35} seconds after the big bang, it is believed that a short phase of exponential expansion, called *inflation*, occurred. By the time it finished, $\sim 10^{-32}$ seconds later, the universe had increased its size at least by a factor e^{60} . Inflation has been introduced in order to explain why our Universe is almost flat and very uniform, as well as the origin of density fluctuations (see, e.g., Liddle, 1999; Liddle & Lyth, 2000, for more details). Afterwards the expansion continues, while the temperature decreases adiabatically. Circa 3 minutes after the big bang, the temperature of the universe is around $T = 10^9 K$: at this stage protons and neutrons can combine and form deuterium, helium and very small quantities of lithium and beryllium. At about $z = 3000$, since the radiation density decreases much more rapidly than that of the matter, the former stops dominating the energy budget and the latter becomes the most important component. At $z = 1000$, i.e. about 300,000 years after the big bang, the thermal energy of the photons drops below 1 eV ($T \sim 10^4 K$) and the electrons can combine with the nuclei forming neutral atoms, mostly hydrogen. This epoch is dubbed *recombination*. The photons are then free to stream and we observe them now as the CMB (see Section 3.2.3). The processes just described occur for all the models depicted in Figure 2.1, although at times that depend on the exact values of the density and equation of state parameters. If there is no cosmological constant, i.e. $\Omega_\Lambda = 0$, matter will continue to be the dominant component and its gravitational pull will decelerate the

expansion of the universe. If the density is $\Omega > 1$, as represented by the orange in the figure, the pull will be enough to eventually stop the expansion and the scale factor will begin to decrease, reaching a new singularity: the *big crunch*. If $\Omega \leq 1$ the expansion will continue forever, but with two different asymptotes at infinite. In the case of the total density being less than one, shown by the blue line in Figure 2.1, the gravitational mass is not enough to stop the expansion and the rate of expansion will always remain strictly positive. $\Omega = 1$ divides the two cases just described: the Hubble parameter tends to zero at infinity and the expansion will stop asymptotically (green line). If the a cosmological constant is present and $\Omega \leq 1$ or $k/a^2 < 3\rho_\Lambda$, an accelerated expansion phase begins and dark energy becomes dominant. In the case shown in Figure 2.1 with a red line, the acceleration begins at $z_{\text{acc}} \approx 0.7$ and the universe undergoes a transition from matter to Λ dominated at $z \approx 0.3$. As the matter density becomes negligible the expansion becomes exponential, as in the inflationary epoch.

2.2 Cosmological perturbation theory

The Copernican principle allows for relatively simple solutions of equation (2.2). In reality the distribution of matter is not homogeneous and, given the non-linear nature of such equations, it is not possible to solve them exactly for realistic metrics. For sufficiently large scales, or high redshifts, the deviations from homogeneity and isotropy are “small” and it is possible to apply perturbation theory (PT; see, e.g., Bardeen, 1980; Kodama & Sasaki, 1984; Durrer, 1994; Bernardeau et al., 2002; Dodelson, 2003, for more detailed explanations). The full metric and energy-momentum, indicated with a tilde, can then be decomposed into a background part, described in Section 2.1 by the FLRW metric, and deviations $\delta g_{\mu\nu}$ and $\delta T_{\mu\nu}$:

$$\tilde{g}_{\mu\nu} = g_{\mu\nu} + \delta g_{\mu\nu} \quad \text{and} \quad \tilde{T}_{\mu\nu} = T_{\mu\nu} + \delta T_{\mu\nu}. \quad (2.10)$$

The fluctuations $\delta g_{\mu\nu}$ and $\delta T_{\mu\nu}$ are separated into three different modes: scalar-, vector- and tensor-like. It is possible to demonstrate (Kodama & Sasaki, 1984) that the three components are decoupled. In the rest of this work I will concentrate on scalar modes, since they connect the metric perturbations to density, pressure and velocity. Vector-like perturbations are damped by the cosmic expansion and tensor modes are related to the propagation of gravitational waves.

Scalar perturbations can be generally described by four functions for the metric (A , B , H_L and H_T) and four for the energy momentum tensor (δ , v , π_L and π_T , Kodama & Sasaki, 1984). The functional form of these variables depends on the choice of the coordinate system, commonly referred to as *gauge*. Gauge transformations are characterised by two degrees of freedom. It is therefore possible to chose a combination of the eight variables of above and obtain six gauge invariant quantities. Common examples of gauge invariant variables are the *Bardeen potentials* Φ and Ψ and the four generalisations of the energy-momentum perturbations Δ , V , Γ and Π (Bardeen, 1980). In the *conformal Newtonian* gauge the energy momentum perturbations can be identified with the following physical

quantities: i) $\delta(\mathbf{x}, t) = \rho(\mathbf{x}, t)/\bar{\rho}(t) - 1$, the density contrast in the point \mathbf{x} at time t with respect to the mean value $\bar{\rho}(t)$; ii) $v(\mathbf{x}, t)$ the peculiar velocity, i.e. the intrinsic velocity of objects with respect to the comoving coordinates; iii) the isotropic and iv) anisotropic pressure fluctuations.

Applying equation (2.2) to the scale invariant scalar modes of $\delta g_{\mu\nu}$ and $\delta T_{\mu\nu}$ it is possible to obtain two equations that connect the potentials Φ and Ψ to the density Δ (generalised Poisson equation) and to the anisotropic pressure Π . The conservation of the energy-momentum tensor produces the generalised version of the continuity and Euler equations. In order to break the degeneracies between the six variables two assumptions are usually made: i) isotropic pressure, i.e. $\Pi = 0$ or equivalently $\pi_T = 0$, which implies that $\Phi = -\Psi$ and ii) adiabaticity, i.e. $\Gamma = 0$ which corresponds to postulate that density and pressure perturbations are related by $\delta p = w\delta\rho$, the same equation of state as the corresponding mean values (equation 2.7).

The continuity and Euler equations, written for the conformal Newtonian gauge, read:

$$\frac{\partial\delta(\mathbf{x}, \tau)}{\partial\tau} + \nabla \cdot \{[1 + \delta(\mathbf{x}, \tau)] v(\mathbf{x}, \tau)\} = 0 \quad (2.11a)$$

and

$$\frac{\partial v(\mathbf{x}, \tau)}{\partial\tau} + \mathcal{H}(\tau)v(\mathbf{x}, \tau) + v(\mathbf{x}, \tau) \cdot \nabla v(\mathbf{x}, \tau) = -\nabla\phi(\mathbf{x}, \tau) + \frac{1}{\rho}\nabla \cdot [p(\pi_L + \pi_T)], \quad (2.11b)$$

where τ is the conformal time defined by $d\tau = dt/a$, $\mathcal{H} = H/a$ and ϕ is the gravitational potential sourced by density fluctuations. With the assumptions described above and the use of the Poisson equation to substitute ϕ with δ , equations (2.11) become, in Fourier space¹:

$$\frac{\partial\delta(\mathbf{k}, \tau)}{\partial\tau} + \theta(\mathbf{k}, \tau) = - \int \frac{d^3\mathbf{k}_1 d^3\mathbf{k}_2}{(2\pi)^3} \delta_D(\mathbf{k} - \mathbf{k}_1 - \mathbf{k}_2) \alpha(\mathbf{k}_1, \mathbf{k}_2) \delta(\mathbf{k}_1, \tau) \theta(\mathbf{k}_2, \tau) \quad (2.12a)$$

and

$$\begin{aligned} \frac{\partial\theta(\mathbf{k}, \tau)}{\partial\tau} + \mathcal{H}(\tau)\theta(\mathbf{k}, \tau) + \frac{2}{3}\Omega_m \mathcal{H}^2(\tau)\delta(\mathbf{k}, \tau) = \\ - \int \frac{d^3\mathbf{k}_1 d^3\mathbf{k}_2}{(2\pi)^3} \delta_D(\mathbf{k} - \mathbf{k}_1 - \mathbf{k}_2) \beta(\mathbf{k}_1, \mathbf{k}_2) \theta(\mathbf{k}_1, \tau) \theta(\mathbf{k}_2, \tau), \end{aligned} \quad (2.12b)$$

where $\theta(\mathbf{x}, \tau) = \nabla \cdot v(\mathbf{x}, \tau)$ and

$$\alpha(\mathbf{k}_1, \mathbf{k}_2) = \frac{(\mathbf{k}_1 + \mathbf{k}_2) \cdot \mathbf{k}_1}{k_1^2}, \quad \beta(\mathbf{k}_1, \mathbf{k}_2) = \frac{|\mathbf{k}_1 + \mathbf{k}_2|^2 \mathbf{k}_1 \cdot \mathbf{k}_2}{2k_1^2 k_2^2}. \quad (2.13)$$

The last two equations describe the non-linear coupling between different modes \mathbf{k} .

¹Through all this thesis we use the Fourier transform convention: $a(x) = (2\pi)^{-3} \int d^3\mathbf{k} a(k) e^{ikx}$ and $a(k) = \int d^3\mathbf{x} a(x) e^{-ikx}$

At linear order, the right hand sides of equations (2.12), that are of second order in the perturbations, can be neglected. Differentiating equation (2.12a) with respect to τ and substituting $\partial\theta(\mathbf{k}, \tau)/\partial\tau$ with equation (2.12b), it is possible to obtain a second order differential equation for the density perturbation, that has a generic solution of the kind $\delta_1(\mathbf{k}, \tau) = D_1^+(\tau)A(\mathbf{k}) + D_1^-(\tau)B(\mathbf{k})$. D_1^+ and D_1^- are an increasing and a decreasing function of time only, which contain information about the cosmological parameters, and A and B are functions of the wave number only. Considering only the growing mode, called *linear growth factor*, the linear solutions of equations (2.12) are:

$$\delta_1(\mathbf{k}, \tau) = D_1(\tau)\delta(\mathbf{k}, 0), \quad \theta_1(\mathbf{k}, \tau) = -\mathcal{H}(\tau)f(\tau)D_1(\tau)\delta(\mathbf{k}, 0), \quad (2.14)$$

where $f(\tau) = d \ln D_1(\tau)/d \ln a$ and $\delta(\mathbf{k}, 0)$ is the initial density contrast. For simplicity I have dropped the superscript “+” of D_1 . The linear growth factor as function of scale factor a is

$$D_1(a) = \frac{5\Omega_M}{2}E(a) \int_0^a \frac{da'}{a'E(a')} \quad (2.15)$$

Beyond the linear regime, equations (2.12) can be solved perturbatively through recursive substitutions and assuming that at order n all the factors δ and θ on the right hand sides are set to their linear theory values. For an *Einstein-de Sitter cosmology* ($\Omega_m = 1$ and $\Omega_\Lambda = 0$), it is possible at each order to factorize the time and k dependence into two separate functions. Noting that in this case $D_1 = a$ and $f = 1$, the full solutions can then be written as

$$\delta(\mathbf{k}, \tau) = \sum_{n=1}^{\infty} a^n(\tau)\delta_n(\mathbf{k}), \quad (2.16a)$$

$$\theta(\mathbf{k}, \tau) = -\mathcal{H}(\tau) \sum_{n=1}^{\infty} a^n(\tau)\theta_n(\mathbf{k}) \quad (2.16b)$$

with

$$\delta_n(\mathbf{k}) = \int \frac{d^3\mathbf{q}_1 \dots d^3\mathbf{q}_n}{(2\pi)^{3n-3}} \delta_D(\mathbf{k} - \sum_{i=1}^n \mathbf{q}_i) F_n(\mathbf{q}_1, \dots, \mathbf{q}_n) \delta(\mathbf{q}_1, 0) \dots \delta(\mathbf{q}_n, 0) \quad (2.17a)$$

and

$$\theta_n(\mathbf{k}) = \int \frac{d^3\mathbf{q}_1 \dots d^3\mathbf{q}_n}{(2\pi)^{3n-3}} \delta_D(\mathbf{k} - \sum_{i=1}^n \mathbf{q}_i) G_n(\mathbf{q}_1, \dots, \mathbf{q}_n) \delta_1(\mathbf{q}_1, 0) \dots \delta_1(\mathbf{q}_n, 0). \quad (2.17b)$$

The PT *kernels* F and G couple modes with different wave-numbers. Comparing equations (2.17) and (2.14), it is clear that at linear order (i.e. $n = 1$), the kernels are $F_1 = G_1 = 1$. At any higher order they can be computed recursively from:

$$F_n(\mathbf{q}_1, \dots, \mathbf{q}_n) = \sum_{m=1}^{n-1} \frac{G_m(\mathbf{q}_1, \dots, \mathbf{q}_m)}{(2n+3)(n-1)} [(2n+1)\alpha(\mathbf{k}_1, \mathbf{k}_2)F_{n-m}(\mathbf{q}_{m+1}, \dots, \mathbf{q}_n) + 2\beta(\mathbf{k}_1, \mathbf{k}_2)G_{n-m}(\mathbf{q}_{m+1}, \dots, \mathbf{q}_n)], \quad (2.18a)$$

$$G_n(\mathbf{q}_1, \dots, \mathbf{q}_n) = \sum_{m=1}^{n-1} \frac{G_m(\mathbf{q}_1, \dots, \mathbf{q}_m)}{(2n+3)(n-1)} [3\alpha(\mathbf{k}_1, \mathbf{k}_2) F_{n-m}(\mathbf{q}_{m+1}, \dots, \mathbf{q}_n) + 2n\beta(\mathbf{k}_1, \mathbf{k}_2) G_{n-m}(\mathbf{q}_{m+1}, \dots, \mathbf{q}_n)], \quad (2.18b)$$

where $\mathbf{k}_1 = \mathbf{q}_1 + \dots + \mathbf{q}_m$, $\mathbf{k}_2 = \mathbf{q}_{m+1} + \dots + \mathbf{q}_n$. For $n = 2$, the kernels are:

$$F_2(\mathbf{q}_1, \mathbf{q}_2) = \frac{5}{7} + \frac{1}{2} \frac{\mathbf{q}_1 \cdot \mathbf{q}_2}{q_1 q_2} \left(\frac{q_1}{q_2} + \frac{q_2}{q_1} \right) + \frac{2}{7} \frac{(\mathbf{q}_1 \cdot \mathbf{q}_2)^2}{q_1^2 q_2^2} \quad (2.19a)$$

$$G_2(\mathbf{q}_1, \mathbf{q}_2) = \frac{3}{7} + \frac{1}{2} \frac{\mathbf{q}_1 \cdot \mathbf{q}_2}{q_1 q_2} \left(\frac{q_1}{q_2} + \frac{q_2}{q_1} \right) + \frac{4}{7} \frac{(\mathbf{q}_1 \cdot \mathbf{q}_2)^2}{q_1^2 q_2^2}. \quad (2.19b)$$

Available data do not agree with the Einstein-de Sitter model, and therefore the perturbative approach just shown becomes in principle not valid. However for Λ CDM-like cosmologies the separability of time and wave-number can be approximatively maintained when the proper growth factor D and its logarithmic derivative f are used. Equations (2.16) can therefore be written as

$$\delta(\mathbf{k}, \tau) = \sum_{n=1}^{\infty} D_1^n(\tau) \delta_n(\mathbf{k}, \tau), \quad (2.20a)$$

$$\theta(\mathbf{k}, \tau) = -\mathcal{H}(\tau) f(\tau) \sum_{n=1}^{\infty} D_1^n(\tau) \theta_n(\mathbf{k}, \tau). \quad (2.20b)$$

In principle with the few ingredients listed above, it would be possible to describe the full density and velocity field at cosmological scales. Unfortunately, we do not have access to the exact initial conditions, set by the inflation, and we cannot observe the dynamical evolution of the Universe, since its timescales are much longer than human ones. Without this information, it is only possible to treat the perturbations statistically, assuming that they are a stochastic realisation of a given process. In the rest of this dissertation I concentrate on the density fluctuations. A stochastic process can be described as a collection of n -point ensemble averages, denoted by $\langle \delta_1 \dots \delta_n \rangle$. Without loss of generality, the mean of the fluctuations can be set to zero by definition, i.e. $\langle \delta(\mathbf{k}, \tau) \rangle = 0$. From the two-point ensemble average, i.e. the variance, the *power spectrum* or its Fourier transform the *correlation function* can be defined as

$$\langle \delta(\mathbf{k}_1, \tau) \delta^*(\mathbf{k}_2, \tau) \rangle = (2\pi)^3 P(\mathbf{k}, \tau) \delta_D^3(\mathbf{k}_1 - \mathbf{k}_2) \quad (2.21a)$$

and

$$\langle \delta(\mathbf{x}) \delta^*(\mathbf{x} + \mathbf{r}) \rangle = \xi(\mathbf{r}), \quad (2.21b)$$

respectively, where $\delta_D^3(\mathbf{k})$ is the three dimensional Dirac delta function. If the process is Gaussian, the mean and variance are sufficient to describe the full system, and the

higher order statistics can be decomposed as products and sums of the one- and two-point averages. Observational constraints (e.g., Komatsu et al., 2011) show that deviations from this primordial Gaussianity, if present, are very small; therefore I assume these deviations to be null.

Because of the assumption that the Universe is isotropic, the power spectrum and the correlation function are independent of the direction of the wave number \mathbf{k} or the separation \mathbf{r} and it is possible therefore to substitute the vectors with their moduli. Given the definition of equation (2.21a) and the perturbative expansion of equation (2.16a), the power spectrum itself can be expanded in series as $P(k, \tau) = \sum_n P_n(k, \tau)$, where $P_n(k, \tau) = D_1^{2n}(\tau)P_n(k)$. At linear order the power spectrum is simply

$$P_1(k, \tau) = D_1^2(\tau)P(k, 0), \quad (2.22)$$

with $P(k, 0)$ the initial power spectrum, while the next order contribution is the sum of two terms, each combining two linear power spectra: $P_2(k, \tau) = P_{22}(k, \tau) + P_{13}(k, \tau)$, where

$$P_{22}(k, \tau) = \frac{1}{4\pi^3} \int d^3\mathbf{q} |F_2(\mathbf{k} - \mathbf{q}, \mathbf{q})|^2 P_1(|\mathbf{k} - \mathbf{q}|, \tau) P_1(q, \tau) \quad (2.23a)$$

and

$$P_{13}(k, \tau) = \frac{3}{4\pi^3} P_1(k, \tau) \int d^3\mathbf{q} F_3(\mathbf{k}, \mathbf{q}, -\mathbf{q}) P_1(q, \tau). \quad (2.23b)$$

As all the averages of an odd number of $\delta(\mathbf{k}, 0)$ are zero, these are the only two contributions at second order. The third order is given by $P_3(k, \tau) = P_{15}(k, \tau) + P_{24}(k, \tau) + P_{33}(k, \tau)$, where each term is a complex double integral and combines three linear power spectra at different wave-numbers (for the explicit expression of these three terms see, e.g., appendix A in Carlson et al., 2009).

The shape of the initial power spectrum, $P(k, 0) = P_{\text{prim}}(k)T^2(k)$, depends on how inflation converted quantum fluctuations into cosmological ones ($P_{\text{prim}}(k)$) and on how the fluctuations at a given scale behave when they enter in the causal horizon as the universe expands, which is encoded in the *transfer function*, $T(k)$. Standard inflationary models predict that primordial cosmological perturbations are created as a nearly scale invariant power law, i.e. $P_{\text{prim}}(k) \propto k^{n_s}$, with the *spectral index* $n_s \approx 1$. Perfect scale invariance is equivalent to the condition that the power spectrum is Harrison-Zel'dovich-Peebles: $\bar{k}^3 P(\bar{k}, \tau_{\text{cros}}) = \text{const}$ when $\bar{k} = \mathcal{H}(\tau_{\text{cros}})$, i.e. when it crosses the horizon at τ_{cros} . The form of $T(k)$ depends on when a given mode k enters the horizon. Very small scales, i.e. large values of k , cross it in the radiation dominated era, where the photon pressure and the expansion create a damped oscillator that suppresses the amplitude of the perturbation. Well within the matter dominated era, instead, all the density perturbations grow as $D_1^+(\tau)$. This means that $T(k \rightarrow \infty) \rightarrow 0$ and $T(k \rightarrow 0) \rightarrow 1$. The initial power spectrum $P(k, 0)$ is therefore approximately described by a double power law (k^{n_s} at very large scales and k^{-i} , with $i > 0$ at very small scales) connected smoothly and with a peak, also called *turnover*, at the scale corresponding to the horizon scale at the matter-radiation equality.

The linear power spectrum $P_1(k, \tau)$ and the first three perturbation terms $P_2(k, \tau)$, $P_3(k, \tau)$ and $P_4(k, \tau)$ as computed from standard perturbation theory are shown in the

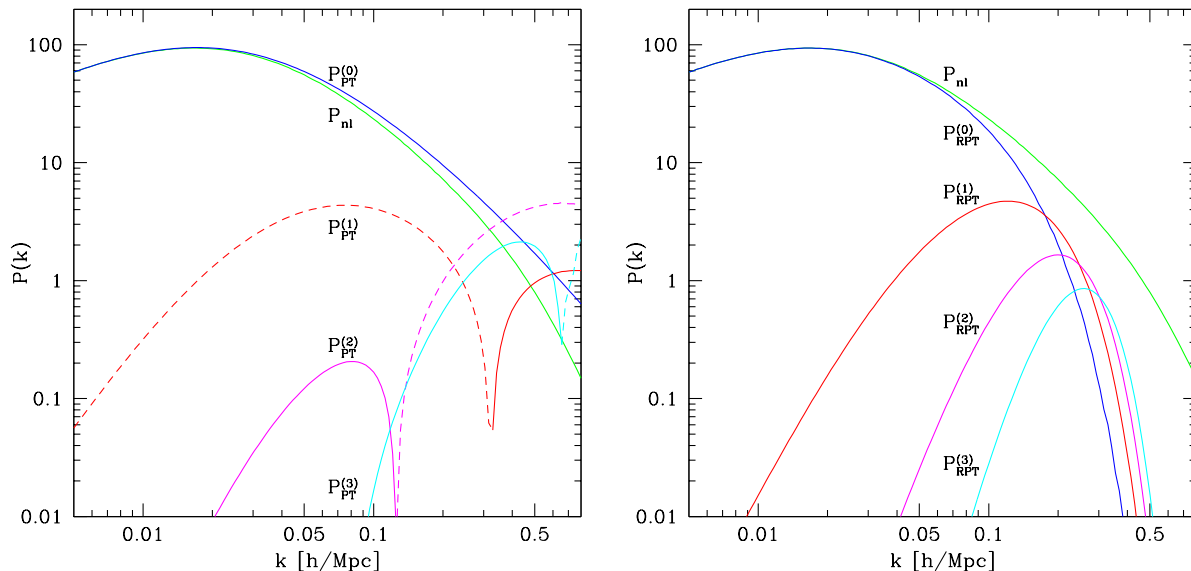


Figure 2.2: *Left* panel: non-linear power spectrum, green line, decomposed according to perturbation theory as the sum of the linear term, blue line, and the first three perturbation terms, red, violet and cyan lines. Solid and dashed lines indicates positive and negative contributions, respectively. Note the different convention in the figure: the index of the series starts from 0 instead then from 1. *Right* panel: same non-linear power spectrum decomposed according to renormalised perturbation theory. The terms $P_{\text{RPT}}^{(0)}$ and $P_{\text{RPT}}^{(n)}$, for $n > 0$ in the figure are equivalent to $G^2(k, \tau)P(k, 0)$ and $P_{n+1\text{MC}}(k, \tau)$ from equation (2.25). Figures from Crocce & Scoccimarro (2006a).

left panel of Figure 2.2 with blue, red, violet and cyan lines, respectively, as a function of the wave number rescaled by the dimensionless Hubble parameter. Solid and dashed lines denote positive and negative contributions. Note that in the figure a convention is used, according to which the starting index of the series expansion is “0” and not “1”, as done here. This figure shows clearly the main problem of standard perturbation theory: with the exception of the linear power spectrum, each term has both positive and negative contributions and their absolute amplitudes do not decrease substantially with increasing order nor do their maxima or minima shift significantly to smaller scales. Because of this it is not possible to predict the sign and amplitude of any term before computing it explicitly, which makes the choice of where to truncate the PT expansion problematic. Therefore PT can be used to describe only the mildly non-linear regime. At low redshift, this translates into the fact that this theory holds only for scales $k \lesssim 0.1 h \text{ Mpc}^{-1}$, if the first two perturbative contributions are used. It has been shown (e.g., Jeong & Komatsu, 2006, 2009) that at higher redshift, e.g. $z = 4 - 5$, the same terms can describe the power spectrum up to $k \approx 0.4 h \text{ Mpc}^{-1}$.

In the last few years, however, many different approaches to improve PT have been studied. In this work I concentrate on *renormalised perturbation theory* (RPT, Crocce &

Scoccimarro, 2006a,b), as it is the base of the phenomenological model that is described in Section 4.2. Approaches based on renormalisation group equations, inspired by quantum field theory, are complementary to RPT (e.g., Matarrese & Pietroni, 2007, 2008). It is possible also to use equation (2.20a) to construct a sequence of n-point ensemble average and introduce a closure equation in order to truncate the series (e.g., Pietroni, 2008; Taruya & Hiramatsu, 2008; Taruya et al., 2009). This is similar to what is done in fluid dynamics when introducing an equation of state. PT can also be improved renormalising the parameters of the model in order to obtain observational quantities (e.g., McDonald, 2006, 2007; Smith et al., 2009).

In few words, RPT consists of a reorganisation of the terms in the PT expansion shown above. At first all the terms in the standard perturbative expansion that are proportional to the primordial power spectrum, like P_{13} and P_{15} , are grouped together into a common factor $G(k, \tau)$, called *renormalized propagator*, that encodes the loss of information of the initial conditions due to non-linear evolution. $G(k, \tau) \approx D_1(\tau)$ at very large scales and decreases at increasing k approximatively as a gaussian with zero mean and characteristic width

$$k_*(\tau) = \left[\frac{1}{6\pi^2} \int dk P_1(k, \tau) \right]^{-1/2}. \quad (2.24)$$

It is interesting to note that, by definition, k_* increases with the inverse of $D_1(z)$ (Crocce et al., 2011). The remaining terms are organised according to the number n of initial modes coupled and enclosed into the *mode coupling power spectrum* $P_{n\text{MC}}(k, \tau)$. As example the lower order, and prototype, of $P_{2\text{MC}}(k, \tau)$ is P_{22} of equation (2.23a). The full non-linear power spectrum is described by RPT as

$$P(k, \tau) = G^2(k, \tau)P(k, 0) + \sum_{n=2}^{\infty} P_{n\text{MC}}(k, \tau). \quad (2.25)$$

The right panel of Figure 2.2 shows the linear power spectrum multiplied by the renormalized propagator as $P_{\text{RPT}}^{(0)}$ (blue line) and the first three mode coupling terms, in red, violet and cyan. Note that $P_{\text{RPT}}^{(n)}$, for $n > 0$ in the figure are the same as $P_{(n+1)\text{MC}}(k, \tau)$ in equation (2.25). The advantage of RPT over standard PT is clear: in the former case each term is positive and is dominant over a restricted range of wave-numbers, which increases with the number of initial modes coupled. This makes, in principle, simple to decide where to truncate the series of equation (2.25) if a given precision at wave number k is required. Recently a multi-fluid approach based on RPT and designed to describe the dark matter and baryon power spectra has been proposed by Somogyi & Smith (2010).

A complementary approach to the one just described, called *Eulerian*, is *Lagrangian perturbation theory* (LPT), in which the particle trajectories, instead of the density and velocity fields, are followed. This is done through a map $\Psi(\mathbf{q}, \tau)$, the *displacement field*, which connects the initial Lagrangian position \mathbf{q} to the Eulerian position \mathbf{x} at any time τ :

$$\mathbf{x}(\mathbf{q}, \tau) = \mathbf{q} + \Psi(\mathbf{q}, \tau). \quad (2.26)$$

It has been shown (Matsubara, 2008a,b) that LPT leads naturally to a partial resummation of an infinite number of Eulerian PT terms and has some analogy with RPT. In the mildly non-linear regime, LPT and RPT are very similar: they both describe the power spectrum as a damped linear component plus a small contribution due to mode coupling and they have the same damping scale given by equation (2.24). However in LPT all the perturbative terms are suppressed in the same way, which makes impossible to use it at non-linear scales.

In this chapter I have introduced the basic equations and quantities that characterise the composition and history of a homogeneous and isotropic universe and I have presented the main concepts of perturbation theory. These notions are the basis of the work exposed in the rest of this thesis.

Observational evidence

Observations, analysed within the framework described in Chapter 2, show that the Universe is close to geometrically flat (i.e. $\Omega_k \approx 0$), composed of dark energy, which behave similarly to a cosmological constant with $w_{\text{DE}} = -1$ and $\Omega_\Lambda \approx 0.73$, cold dark matter, for which $\Omega_{\text{DM}} \approx 0.23$ and baryons with $\Omega_b \approx 0.04$ and that primordial density fluctuations are adiabatic, nearly Gaussian and almost scale invariant (see e.g. Komatsu et al., 2011)

In this chapter I describe some of the observations that I use to constrain cosmological parameters in Chapter 5. Since it is the main topic of my doctoral work, in Section 3.1 I introduce the most important concepts related to the large scale structure of the Universe (LSS). Then in Section 3.2 I describe briefly type Ia supernovae (Section 3.2.1), the direct measurement of the local Hubble parameter (Section 3.2.2) and the cosmic microwave background (Section 3.2.3).

In Section 3.3 I show that the use of different independent observations is important in cosmology. In fact, each of the tests described in this chapter is more or less sensitive to certain parameters or combinations of parameters and presents strong degeneracies among some of them. The use of the combined information from different sources can break some of the degeneracies and allow to obtain more accurate cosmological parameters.

3.1 Large Scale Structure

Dark matter composes about the 85% of the total gravitational mass in the Universe, influencing its evolution, both in terms of background and perturbations, much more than baryons. Despite this fact, dark matter interacts only gravitationally and we cannot directly measure its distribution. We can observe mostly photons emitted by stars, gas or dust and we can trace dark matter through the distribution of these sources or through its effects on the path of the light. The latter is called *gravitational lensing* and is not discussed in this thesis. I will concentrate on the distribution of light sources, in particular galaxies.

Galaxies are biased tracers of the underlying matter distribution, i.e. they do not trace

it exactly. The relation between galaxies and the dark matter distribution changes with redshift and depends upon the mass m , the luminosity L and the assembly history of the galaxies, as it has been measured both observationally and with numerical simulations (e.g., Davis & Geller, 1976; Norberg et al., 2001, 2002; Zehavi et al., 2002; Phleps et al., 2006; Croton et al., 2007; Dalal et al., 2008; Reid et al., 2010b). Assuming that the connection between galaxy and dark matter densities is local, i.e. that it can be described as function of the local coordinates only, and that $\delta_{\text{DM}}(\mathbf{k}) \ll 1$, the galaxy density contrast can be written as (Fry & Gaztanaga, 1993):

$$\delta_{\text{g}}(\mathbf{k}, z, m, L) = f(\delta_{\text{DM}}(\mathbf{k}, z)) = \sum_{n=0}^{\infty} \frac{b_n(z, m, L)}{n!} \delta_{\text{DM}}^n(\mathbf{k}, z). \quad (3.1)$$

At lowest order all the terms $n > 1$ can be discarded and $P_{\text{g}}(k, z, m, L) = b_1^2(z, m, L)P_{\text{DM}}(k, z)$, with b_1 the linear bias. I assume that the term b_0 , which is related with the stochasticity of the galaxy bias, is uncorrelated with $\delta_{\text{DM}}(\mathbf{k}, z)$ (e.g. Yoshikawa et al., 2001; Jeong & Komatsu, 2009). High mass objects tend to grow and cluster in over-dense regions and to be almost absent where the density is low: this enhances the density fluctuations, causing an increase of the power spectrum amplitude and thus $b_1 > 1$. Low mass and luminosity galaxies are instead more homogeneously distributed, which results in a decrease of the power spectrum and in a bias less than unity. The coefficients in equation (3.1) cannot be determined within the perturbation theory approach, thus either they are considered as free parameters or a different theoretical framework must be used. The halo model (HM, see Cooray & Sheth, 2002, for a review) provides a way to compute, although only approximate, the values of the bias parameters both for *haloes*, i.e. bound structures that form due to gravitational collapse of dark matter in over-dense regions, and galaxies, that form in these haloes. One of the basic ingredients of the HM is the *mass function* $n(z, M)$, which represents the comoving number density of haloes of mass M at redshift z . The functional form of $n(z, M)$ depends upon the cosmology and the dynamics of the formation of haloes. It has been first determined analytically assuming that the collapse is spherical (Press & Schechter, 1974) and later improved by allowing for the formation of ellipsoidal structures (Sheth & Tormen, 1999; Sheth et al., 2001). The mass function has also been measured from N-body numerical simulations, providing a higher accuracy (see, e.g., Jenkins et al., 2001; Warren et al., 2006; Tinker, 2007; Pillepich et al., 2010). The latter approach is limited by the resolution and the volume of the simulation, which regulate the smaller and larger halo masses achievable and therefore the mass range over which the measurement is precise. From the density contrast of haloes with mass M that collapsed at redshift z_1 and that are at z in a volume V containing mass M_V and using the expansion of equation (3.1), it is in principle possible to estimate the bias parameters as complex functions of the $n(z, M)$ and its derivatives. Assuming the mass function from Sheth & Tormen (1999) the linear bias is

$$b_1(z, m) = 1 + \frac{q\nu - 1}{\delta_{\text{sc}}(z)} + \frac{2p}{\delta_{\text{sc}}(z)(1 + (q\nu)^p)}, \quad (3.2)$$

where $p \approx 0.3$, $q \approx 0.75$, $\delta_{\text{sc}}(z)$ is the critical density which causes the spherical collapse at z and $\nu = \delta_{\text{sc}}^2(z)/\sigma^2(m)$, where the denominator is the variance of the initial density

contrast, extrapolated linearly to present epoch, in a sphere of radius determined by the mass and the mean density of the halo as $R = (3m/4\pi\bar{\rho})^{1/3}$. Equation (3.2) shows that the bias grows with mass, according to the idea that higher dark matter over-densities collapsed earlier. The bias of a halo sample with masses within the limits M_1 and M_2 can be measured with a weighted average:

$$b_{1\text{ eff}}(z, [M_1, M_2]) = \frac{\int_{M_1}^{M_2} dM' b_1(z, M') n(z, M')}{\int_{M_1}^{M_2} dM' n(z, M')}. \quad (3.3)$$

Haloes provide the potential well in which gas can fall, cool and form stars and galaxies. Although the physics of this process is very complicated, haloes can be populated with galaxies statistically according to the conditional probability of finding N_{gal} in a halo of mass M , whose mean, or first moment, is $\langle N_{\text{gal}} | M \rangle$. This relation depends on the type, luminosity and mass of the galaxies considered. The linear bias of a class of galaxies can be easily computed as:

$$b_{1\text{ gal}}(z, m, L) = \frac{\int_0^\infty dM \langle N_{\text{gal}} | M \rangle b_1(z, M) n(z, M)}{\int_0^\infty dM \langle N_{\text{gal}} | M \rangle n(z, M)}. \quad (3.4)$$

The analysis of the matter distribution, and the computation of the power spectrum and correlation function, is further complicated by the fact that the physical or comoving coordinates of the galaxies cannot in general be measured directly but are inferred, assuming a set of cosmological parameters, from the observed angular positions and redshifts of the objects. The latter is given by the sum of the contributions from the cosmological expansion and the *Doppler shift* due to its peculiar motion along the line of sight. Therefore, when obtaining the distance assuming that the redshift is only cosmological, the resulting map of the galaxy distribution is distorted and appears to be anisotropic. On large scales the motion of objects is dominated by a coherent inflow towards the dense regions, which therefore appear denser than they are and squeezed in the direction parallel to the line of sight. This is usually called *Kaiser effect* (Kaiser, 1987). At these scales, the three dimensional redshift space power spectrum can be linked to the real space isotropic one by $P_s(k, \mu) = (1 + \beta\mu^2)^2 P_r(k)$, where $\beta = f/b_1$ and μ is the cosine of the angle between the vector \mathbf{k} and the line of sight. The spherically averaged power spectrum becomes $P_s(k) = \int d\mu P_s(k, \mu) = S_{\text{lin}} P_r(k)$, with the *Kaiser factor*

$$S_{\text{lin}} = \frac{P_s(k)}{P_r(k)} = 1 + \frac{2}{3}\beta + \frac{1}{5}\beta^2. \quad (3.5)$$

On small scales the random motions within virialized structures dominate, making them appear elongated along the line of sight, an effect called *fingers-of-god* (Jackson, 1972), and decreasing the amplitude of the spherically averaged power spectrum. The linear theory description of equation (3.5) is only valid asymptotically on extremely large scales and deviations induced by fingers-of-god are measurable even at scales $k > 0.03 h \text{ Mpc}^{-1}$ (Scoccimarro, 2004; Angulo et al., 2008; Jennings et al., 2011). In the halo model approach

described above a generic galaxy sample is decomposed into central and satellite galaxies. The former are assumed to lie at or near the centre of the dark matter haloes while the later are objects gravitationally bound to the potential of massive haloes that already contain a central galaxy. In this way, the signature of the fingers-of-god effect can be associated with the contribution of the satellite galaxies, which then are responsible for the most important non-linear redshift space distortions. In order to minimise their impact on the power spectrum shape, different approaches have been proposed. For example, Tegmark et al. (2004) analysed the second data release of SDSS compressing the fingers-of-god into isotropic structures and, more recently, Reid & Spergel (2009) and Reid et al. (2009) proposed a method to reconstruct the underlying halo density field from a galaxy sample by identifying fingers-of-god like structures and replacing them by one single halo, minimising de facto the impact of satellites.

At very large scales, both the bias and the Kaiser effect are scale independent and their only effect is to change the amplitude of the power spectrum or the correlation function. At smaller scales the two effects are functions of the wave-number or distance and distort the shape of the two-point statistics by damping their amplitudes. These effects add to the distortions introduced by non-linear evolution. In Section 4.3 I will discuss further these effects using results from numerical simulations.

Besides the full shape, the power spectrum and correlation contain a feature called baryonic acoustic oscillation (BAO), which is related to the physics of the primordial baryon-photon plasma. Before recombination, photons, electrons and nuclei were locked into a plasma traversed by sound waves generated by inflation. Short after recombination, at the drag epoch, the baryons were released from the photon pull and those waves froze after having travelled a comoving distance of about $110 h^{-1}$ Mpc. This left a signal in the galaxy distribution, where a small statistical excess of objects separated by this distance can be observed. In the correlation function it corresponds to a quasi gaussian peak (Matsubara, 2004), while in the power spectrum it shows up as damped quasi-harmonic oscillations (Sugiyama, 1995; Eisenstein & Hu, 1998, 1999). The physical scale of the BAOs can be computed very accurately in linear theory, suggesting that they can be used as a standard ruler. In reality, although they are at very large scales, BAOs are modified by non-linear evolution in two ways: i) their amplitude is decreased with respect to linear theory and ii) their position is shifted towards smaller scales by a few percent (Crocco & Scoccimarro, 2008; Sánchez et al., 2008; Smith et al., 2008). Besides this, bias and redshift space distortions modify additionally the BAO signal.

In addition to the signature of the initial conditions, namely the spectral index and the primordial amplitude, the shape of the power spectrum is characterised by three scales (Silk, 1968; Dodelson, 2003; Shoji et al., 2009): i) the Hubble horizon at matter-radiation equality $r_{\mathbf{H}}(z_{\text{eq}}) = 1/[a_{\text{eq}}H(z_{\text{eq}})]$, ii) the sound horizon at the drag epoch $r_{\mathbf{s}}(z_{\mathbf{d}}) = \int_0^{t(z_{\mathbf{d}})} dt c_{\mathbf{s}}(t)/a(t)$, with the *sound speed* of the baryon-photon plasma $c_{\mathbf{s}}(t) = 4\Omega_{\mathbf{r}}/\{\sqrt{3}[1+a(t)]3\Omega_{\mathbf{b}}\}$ and iii) the *Silk damping* scale $k_{\mathbf{d}} \propto (\Omega_{\mathbf{b}}h^2)^{1/2}(\Omega_{\mathbf{M}}h^2)^{1/4}$. In the power spectrum they can be identified, respectively, with the turnover, the BAO and the large k damping scales and depend mainly on matter, baryon and photon densities. At

redshift z , their apparent sizes in direction perpendicular and parallel to the line of sight, respectively $\delta\theta(z)$ and $\delta z(z)$, are related to the physical ones by the inverse of the *angular diameter distance* $D_A(z)$ and the Hubble parameter $H(z)$ (e.g., Shoji et al., 2009). D_A is defined, in terms of D_C (equation 2.8), as

$$D_A(z) = \frac{1}{1+z} \begin{cases} \frac{1}{H_0\sqrt{\Omega_k}} \sinh [\sqrt{\Omega_k}H_0D_C(z)] & \Omega_k > 0 \\ D_C(z) & \Omega_k = 0 \\ \frac{1}{H_0\sqrt{|\Omega_k|}} \sin [\sqrt{|\Omega_k|}H_0D_C(z)] & \Omega_k < 0 \end{cases}. \quad (3.6)$$

$D_A(z)$ and $H(z)$ are functions of all the density and equation of state parameters and are sensitive in particular to dark energy and curvature. When the radial and angular information is combined, for instance when considering the spherical averaged power spectrum, the apparent size of the scales described above is proportional to $[H(z)/D_A^2(z)]^{1/3}$.

The left panel of Figure 3.1 shows, with circles, the power spectrum measured from the two-degree Field Galaxy Redshift Survey (2dFGRS, Colless et al., 2003; Cole et al., 2005). The errors indicated by bars are computed using lognormal mock catalogues (LN, Coles & Jones, 1991), while the ones indicated with the shaded area in the lower panel are derived from a jack-knife resampling of the data. The dashed and solid lines show a model power spectrum, defined by the parameters listed in the upper panel, before and after the convolution with the window function of the survey (see Section 5.2.1 for more details). The lower panel shows the same information of the upper one, but divided by a reference power spectrum without BAOs computed with the formulae of Eisenstein & Hu (1998, 1999). The right panel of Figure 3.1 shows, with filled circles, the large scale correlation function computed from the *luminous red galaxy* sample (LRGs, Eisenstein et al., 2005) in the third data release of the Sloan Digital Sky Survey (SDSS, York et al., 2000). The error-bars are computed from a set of mock catalogues. The three upper solid lines show models with different values of $\Omega_M h^2$, while the lower one shows the correlation function without the BAO feature. Note that the vertical axis of the outer plot mixes logarithmic and linear scaling. The inner plot is a zoom around the BAO peak. These two figures, besides showing an example of the measured power spectrum and correlation function, are historically very important, since they represent the first detection of the BAO signature in the galaxy distribution.

The large scale galaxy distribution has been used intensively in the past years to extract cosmological information, alone or in combination with other independent datasets (e.g., Efstathiou et al., 1990; Baumgart & Fry, 1991; Feldman et al., 1994; Efstathiou et al., 2002; Percival et al., 2002; Tegmark et al., 2004; Cole et al., 2005; Eisenstein et al., 2005; Sánchez et al., 2006; Percival et al., 2007; Cabré & Gaztañaga, 2009a; Gaztañaga et al., 2009; Sánchez et al., 2009; Kazin et al., 2010; Percival et al., 2010; Reid et al., 2010a; Blake et al., 2011; Tinker et al., 2011). Some authors (e.g., Percival et al., 2010) extracted the BAO signal from the power spectrum and based their cosmological analysis on this feature alone. This approach has the advantage that BAOs are easier to model than the full shape of the power spectrum or the correlation function, but on the other hand the information

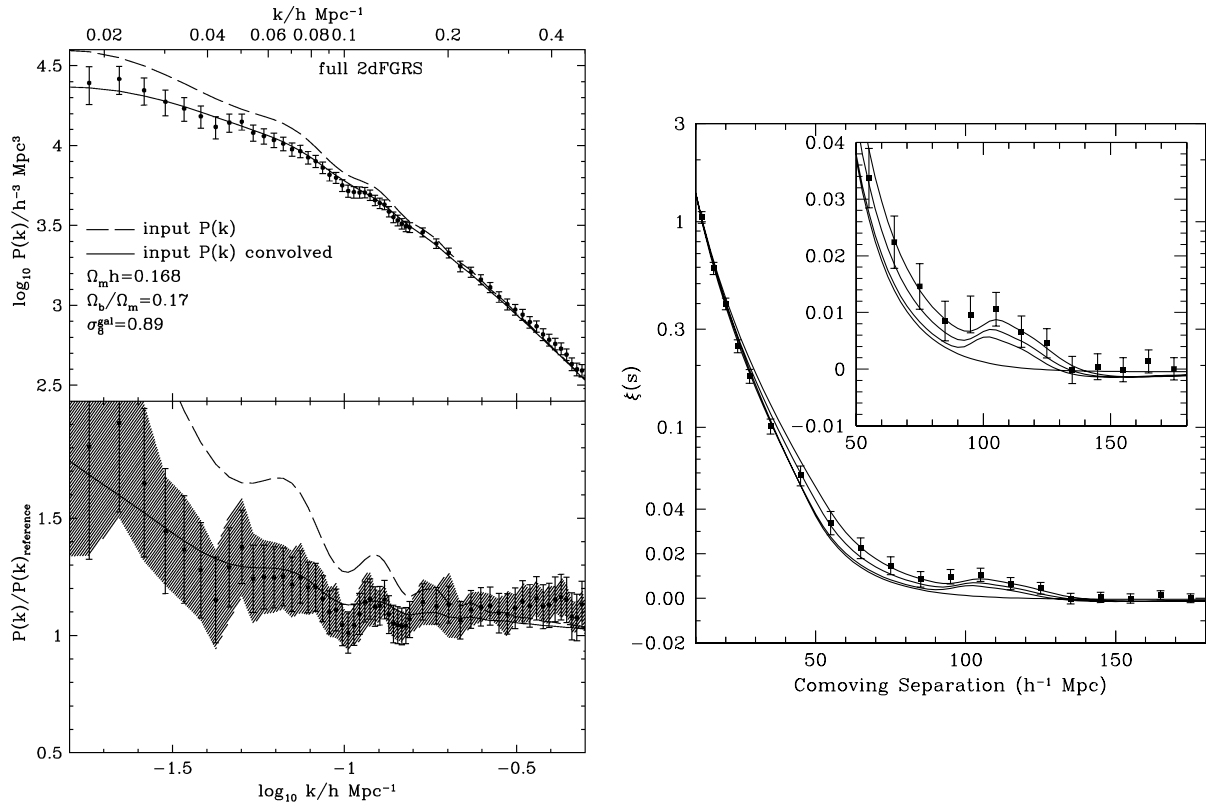


Figure 3.1: *Left* panel: power spectrum from the two-degree Field Galaxy Redshift Survey, circles, with errors determined from lognormal mocks, bars, and jack-knife resampling of the data, shaded areas. The dashed and solid lines show a model power spectrum with the parameters listed in the upper panel, before and after convolving it with the survey window function. The lower panel shows the same power spectra of the upper one divided by one without BAO oscillations. Figure from Cole et al. (2005). *Right* panel: large scale correlation function of the luminous red galaxy sample from Sloan Digital Sky Survey. The errors are computed from a set of mock catalogues. The three upper lines are for models with different values of $\Omega_m h^2$, the lower line represents a model without BAO. The vertical axis of the outer panel mixes linear and logarithmic scaling. The inner panel shows a zoom around 100 $h^{-1} \text{ Mpc}$. Figure from Eisenstein et al. (2005).

encoded in the broad band shape of the galaxy two-point statistics is discarded, which causes a degradation of the accuracy at which cosmological parameters can be constrained (Sánchez et al., 2008; Shoji et al., 2009; Blake et al., 2011).

In the next years several new galaxy redshift surveys will allow to measure the large scale clustering pattern of the Universe and the BAO feature with a precision much higher than what is possible with present-day datasets. Thanks to this, it will be possible to constrain the cosmological parameters with a higher accuracy, in particular the ones related to dark energy. In order to obtain unbiased constraints it is necessary to use models that can account accurately for the effects of non-linear evolution, bias and redshift space distortions

in the full shape of the two-point and higher order statistics. Motivated by this, I propose a new model of the full shape of the power spectrum, presented in Section 4.2, which thanks to a few parameters describes accurately the clustering of biased objects in redshift space and can be successfully applied to a galaxy catalogue (see Chapter 5).

3.2 Additional observations

This section introduces the basic concepts of type Ia supernovae and cosmic microwave background and describes a precise measurement of the local Hubble parameter.

3.2.1 Type Ia supernovae

Type Ia supernovae (SNIa) provided the first observational evidence that the expansion of the Universe is accelerating and that dark energy constitutes about the 73% of the total energy density. They are among the brightest object in the Universe, visible also at $z > 1$, and are caused by the thermonuclear runaway of white dwarf stars. The signature of SNIa does not vary much from object to object and from the time evolution of the observed luminosity, the *light curve*, it is possible to infer the absolute luminosity L : correcting for these differences makes them standard candles. From L and the measured flux F it is possible to infer the *luminosity distance* of the object at redshift z , which is defined as:

$$D_L(z) \equiv \sqrt{\frac{L}{4\pi F}} = (1+z)^2 D_A(z). \quad (3.7)$$

Equation (3.7) can also be rewritten as $\mu = 5 \log(D_L/10\text{pc})$, where $\mu = m - M - K$ is called *distance modulus*. The *apparent* and *absolute magnitudes* are defined as $m = -2.5 \log(F/F_0)$ and $M = -2.5 \log(L/L_0)$, where F_0 and L_0 are a reference flux and luminosity, which cancel out in the definition of μ . The last term in the distance modulus is the *K-correction*, that accounts for the fact that the light observed at a given wavelength was emitted at a shorter one. Therefore knowing the luminosities and fluxes, or the absolute and apparent magnitudes, and the redshifts of a set of SNIa it is possible to infer the density parameters Ω_i and w_{DE} . However, a general consensus about the physics of SNIa and the impact of selection effects, intrinsic differences between the objects and of the effects of galactic and intergalactic medium has not yet been reached. This produces tensions between different models of light curves, which result in different estimations of the luminosities of objects, making the analysis of systematic effects very complicated.

Evidences of the existence of dark energy were found independently by two groups (Riess et al., 1998; Perlmutter et al., 1999) analysing the luminosity-distance relation, or Hubble diagram, measured from two relatively small samples of SNIa. Figure 3.2 shows the luminosity-distance relation from Perlmutter et al. (1999) (coloured circles with error bars) and seven models specified by the parameters annotated on the upper right corner. The vertical axis shows the effective rest-frame B magnitude, which is analogous of the distance modulus. It rescales the measured peak magnitude according to the width of the

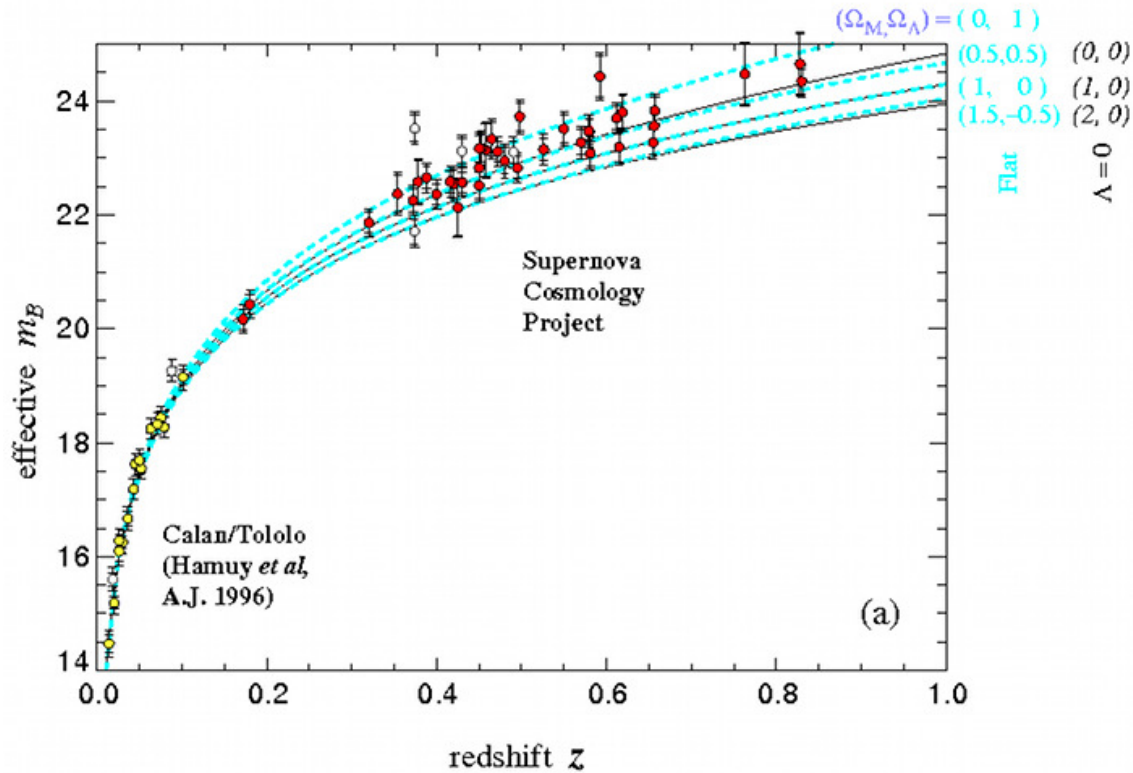


Figure 3.2: Luminosity-distance relation from SNIa observations, dots with error bars, compared with seven models, with parameters listed in the upper right corner. The vertical axis shows the effective rest-frame B magnitude, corrected for the width of the light curve, the extinction and the K-correction. Figure from Perlmutter et al. (1999)

light curve, to the extinction due to the medium between the SNIa and the observer and to the K-correction.

Over the past decade SNIa observations were carried out with a large number of telescopes, subjected to different systematics and with a statistically small number of objects, ranging between few and few hundreds. In order to increase the number of objects, many samples have been built combining different observations in a uniform way: e.g. the Union compilation (Kowalski et al., 2008), the Sloan Digital Sky Survey-II Supernova Survey set (SDSS SN, Kessler et al., 2009), the Constitution set (Hicken et al., 2009), the Union2 compilation (Amanullah et al., 2010) and the Supernova Legacy Survey Three Year Data (SMLS3, Sullivan et al., 2011). In Chapter 5 I use two of these datasets: the Union2 and the SDSS SN.

The Union2 sample consists of 557 SN drawn from 17 datasets in the redshift range $0.015 \leq z \leq 1.4$. It is the largest available supernovae sample to date and is used in the main analysis of this thesis. All the objects have been selected according to common criteria and the distance information has been extracted using the light-curve fitter SALT2

(Guy et al., 2007). Furthermore, the analysis of systematic effects is improved with respect to previous similar works, in particular the Union and Constitution sets. Amanullah et al. (2010) showed that the cosmological constraints obtained with or without the inclusion of systematic errors do not change substantially, a part from a decrease in the uncertainties at which they are determined. In Section 5.4 I make use of the luminosity-distance relation from the Union2 with both statistic and systematic errors. In Sections 5.4.1 and 5.4.3, I also test the impact of neglecting the systematic uncertainties in my analysis.

The SDSS SN sample consists of 288 SNIa from 5 different experiments. The objects have been chosen according to the same criteria and all light curves measured have been fitted with MLCS2K2 (Jha et al., 2007) and SALT2 in order to measure the distance modulus. Since most of the objects contained in this sample are also part of the Union2, the results obtained with these samples, when the SALT2 is used, are only slightly different, mostly because of the lower number of SNIa in SDSS SN. Therefore I use only the luminosity-distance relation obtained with MLCS2K2. In Sections 5.4.1 and 5.4.3 I discuss the results obtained when these data are used. Hicken et al. (2009) and Kessler et al. (2009) have shown that the use of different models of light curves can have important effects on the inferred distance modulus. They found that the differences between the luminosity-distance relation obtained from MLCS2K2 and SALT2 can give rise to tensions in the cosmological constraints up to the $1-2\sigma$ level. These offsets can be diminished with a careful selection of SNIa and using larger samples, but a better understanding of their origin is important in order to obtain reliable cosmological information.

3.2.2 Hubble parameter

Nearby SNIa and other standard candles can be used in order to measure directly the local Hubble parameter. In fact, for small redshifts, assuming that peculiar motions are negligible, the recession velocity of a galaxy v and its physical distance d are relate linearly by $v = cz = H_0 d$. With an accurate measurement of the distance, obtained from Cepheids and SNIa, and of the redshift of nearby galaxies it is possible to measure directly H_0 . Cepheids are variable stars which show a tight correlation between period and luminosity and that can be therefore used as standard candels. In Chapter 5 I use a measurement of the Hubble parameter as a prior knowledge when constraining cosmological parameters.

The Supernovae and H_0 for the Equation of State Program (SHOES, Riess et al., 2009) aims at the direct measurement of the Hubble parameter at present epoch, H_0 , to better than 5% accuracy. The SHOES team identified 6 nearby spectroscopically typical SNIa, that have been observed before maximum luminosity, that are subject to low reddening and that reside in galaxies containing Cepheids. Thanks to 260 Cepheids observed with the Near-Infrared Camera and Multi-Object Spectrometer (NICMOS) on the Hubble Space Telescope (HST) in the 6 host galaxies and in the galaxy NGC 4258, which hosts a water maser that allows a precise determination of the distance, the authors could calibrate directly the peak luminosity of the SNIa. Combining this 6 objects with 240 SNIa at redshift $z < 0.1$, they measured the Hubble parameter $H_0 = 74.2 \pm 3.6 \text{ km s}^{-1} \text{ Mpc}^{-1}$. The error includes both statistical and systematic uncertainties.

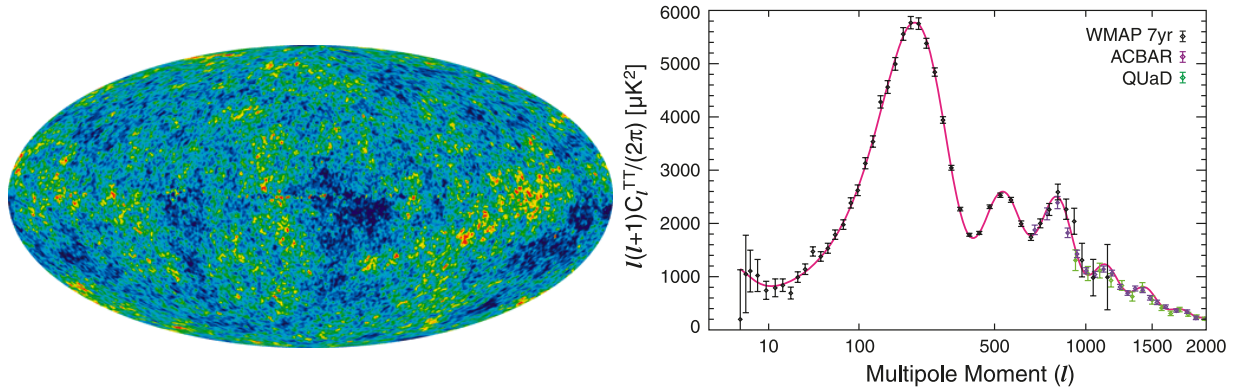


Figure 3.3: *Left* panel: WMAP 7 years full sky map of the CMB fluctuations. The anisotropies are shown in a linear scale between -200 and $200 \mu\text{K}$. Figure from <http://lambda.gsfc.nasa.gov>. *Right* panel: CMB angular power spectrum from the WMAP7, black circles, ACBAR, red circles, and QUaD, green circles. The solid line shows the the best fit ΛCDM model as obtained from WMAP data alone. Figure from Komatsu et al. (2011).

Using spectral properties of early-type galaxies, Moresco et al. (2011) recently constrained the Hubble parameter to $H_0 = 72.6 \pm 2.9 \text{ km s}^{-1} \text{ Mpc}^{-1}$ at 68% confidence level. While finishing the work presented in Chapter 5, Riess et al. (2011) refined the analysis of the SHOES program and obtained $H_0 = 73.8 \pm 2.4 \text{ km s}^{-1} \text{ Mpc}^{-1}$.

3.2.3 Cosmic microwave background

The observations of the temperature fluctuations in the CMB provide one of the most striking evidences that the Universe is homogeneous and isotropic to a very high degree. Its spectrum, i.e. the intensity as function of the frequency, is the most perfect black body known and has a temperature of $2.728 \pm 0.004 \text{ K}$ (Fixsen et al., 1996). If this is subtracted from the CMB signal and foreground emissions, mostly due to the diffuse signal from the Milky Way and point-like sources, are accounted for, fluctuations of the order of 10^{-5} K become visible.

The left panel in Figure 3.3 shows a full sky map of the temperature fluctuations in the CMB as measured by the *Wilkinson microwave anisotropy probe* (WMAP) satellite after 7 years of observations (WMAP7, Jarosik et al., 2011; Komatsu et al., 2011; Larson et al., 2011). The fluctuations are shown in a linear scale between -200 and $200 \mu\text{K}$. The temperature angular power spectrum, computed from the coefficients of the expansion in spherical harmonics of the CMB anisotropies, is shown in the right panel of Figure 3.3 (Komatsu et al., 2011). The black circles with error bars are computed from the WMAP7 data, the red and green circles from the two ground based experiments Arcminute Cosmology Bolometer Array (ACBAR, Kuo et al., 2007; Reichardt et al., 2009) and QUEST at DASI (QUaD, Brown et al., 2009). The red solid line shows the best fit ΛCDM model, when WMAP data alone are used ($\Omega_\Lambda = 0.73$, $\Omega_M = 0.27$). Cosmological information is

encoded in the CMB power spectrum through its shape and the position and amplitude of the peaks. The low multipole amplitude is directly related to the initial conditions. The apparent position of the peaks is proportional, similarly to the BAO scale in the galaxy power spectrum, to the ratio of the angular diameter distance to the recombination $D_A(z_{\text{rec}})$, and the sound horizon scale at the same epoch $r_s(z_{\text{rec}})$. The relative amplitudes of the second and third peaks with respect to the first one are proportional to the baryon density and to the matter to radiation densities ratios, respectively (e.g., Hu et al., 2001). Finally the Silk damping decreases the amplitude of the small scale CMB power spectrum as well as the galaxy one.

In Chapter 5 I use CMB measurements from five different experiments. WMAP7 make available measurements of the temperature angular power spectrum in the multipole range $2 \leq l \leq 1000$ and of the temperature-E polarisation cross power spectrum in the range $2 \leq l \leq 450$. Measurements of higher multipoles can be obtained from other four experiments which observe the CMB temperature anisotropies on smaller areas of the sky with a much higher resolution. I use the measurements of the temperature angular power spectrum in i) 14 bandpowers in the range $910 \leq l \leq 1850$ from ACBAR, ii) 6 bandpowers in the range $855 \leq l \leq 1700$ from the Cosmic Background Imager (CBI, for latest results see Sievers et al., 2009), iii) 7 bandpowers in the range $925 \leq l \leq 1400$ from the 2003 flight of the Balloon Observations Of Millimetric Extragalactic Radiation and Geophysics (BOOMERanG Jones et al., 2006; MacTavish et al., 2006; Montroy et al., 2006; Piacentini et al., 2006) and iv) 11 bandpowers in the range $974 < l < 1864$ from the final release of QUaD. I also use E and B polarisation (EE and BB) and the cross temperature-E polarisation (TE) angular power spectra measurements from the latter three experiment. i) CBI: EE in 7 bandpowers in the range $860 \leq l \leq 1800$, BB in 5 bandpowers in the range $0 \leq l \leq 5000$ and TE in 8 bandpowers in the range $860 \leq l \leq 1800$; ii) BOOMERanG: EE and BB in 3 bandpowers in the range $600 < l < 1000$ and TE in 6 bandpowers in the range $450 \leq l \leq 950$; iii) QUaD: EE, BB and TE in 17 bandpowers in the range $488 < l < 1864$. In order to avoid complex correlations, I discard, for these four experiments, values of l that overlap with the multipoles measured from WMAP.

In the next years the Planck satellite (Ade et al., 2011) will measure the signal from temperature and polarisation CMB anisotropies with unprecedented precision, improving substantially the accuracy at which we can constrain cosmological parameters.

3.3 Combining experiments

In the previous sections I have introduced some of the most used probes in cosmological analyses and I have briefly described how the observed quantities depend upon the expansion rate, curvature, density and equations of state parameters. Each experiment can be more sensitive to a subset of parameters than to another and is subject to degeneracies among some of them. Because of it, not all cosmological parameters can be constrained with high accuracy. Figure 3.4 (Reid et al., 2010a) shows the two-dimensional constraints from CMB, SNIa and LLS data, with blue and green shaded areas and solid lines, respec-

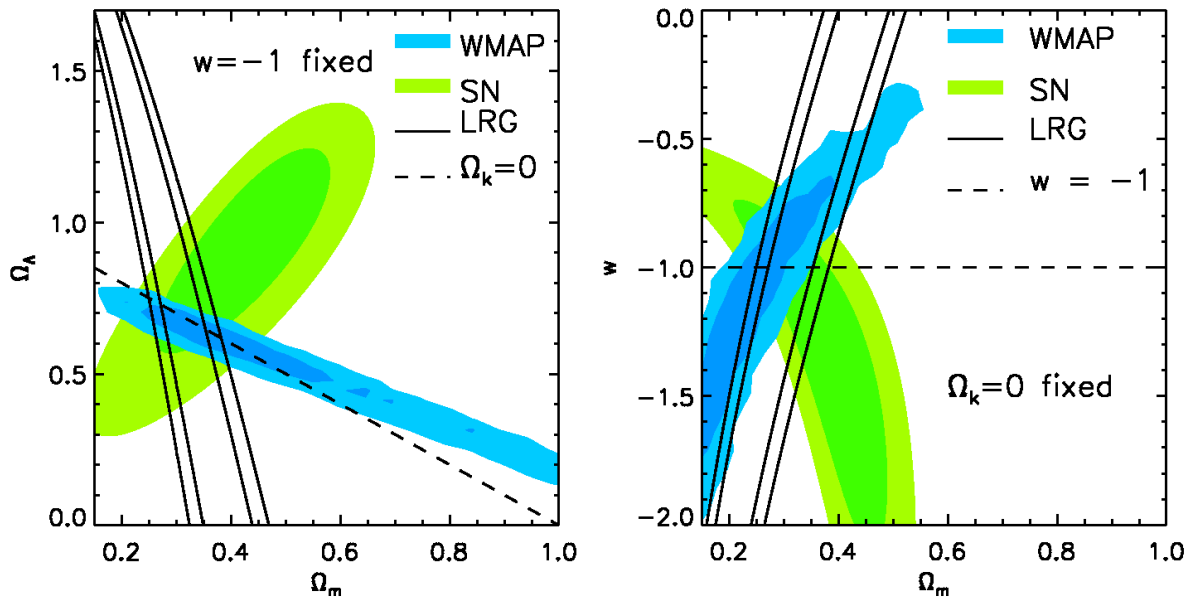


Figure 3.4: Two-dimensional marginalised constraints from CMB (blue shaded areas), SNIa (green shaded areas) and LSS (solid lines); the inner and outer contours show the 68 and 95% confidence levels. *Left panel:* $\Omega_M - \Omega_\Lambda$ plane for a Λ CDM model with free curvature. *Right panel:* $\Omega_M - w_{DE}$ for a flat cosmology. Figure from Reid et al. (2010a)

tively; the inner and outer contours show the 68 and 95 % confidence limits. The left panel shows the results in the $\Omega_M - \Omega_\Lambda$ plane for a model in which dark energy is given by a cosmological constant and curvature is allowed to vary. The right Panel depicts the constraints in the $\Omega_M - w_{DE}$ plane for a flat model. This example shows clearly that it is not possible to extract accurate information about densities, curvature and dark energy equation of state parameter from each experiment individually because of the strong degeneracies. Thanks to the fact that the latter are different in the three cases shown, when their information is combined it is possible to obtain very accurate constraints on cosmological parameters. Besides this, the fact that all three intersect in the same region of the parameter space, highlights the consistency between them.

The results shown in Figure 3.4 and from other works (e.g. Sánchez et al., 2009; Amanullah et al., 2010; Komatsu et al., 2011; Percival et al., 2010), concur to describe a Universe where dark energy dominates the energy budget with about 73% of the total, geometry is to very high degree Euclidean and w_{DE} does not exhibit any time evolution and is consistent with -1 with a 5-10% accuracy.

A new model for the full shape of the matter power spectrum

In this chapter a new phenomenological model for the large scale power spectrum, able to account for non-linear bias and redshift space distortions, is presented and tested against numerical simulations. In section 4.1 I describe the simulations used in this analysis and the power spectra measured from them. Section 4.2 presents the model and Section 4.3 explains the tests performed in order to probe its accuracy. The content of this chapter is based on the work published in Montesano et al. (2010).

4.1 N-body simulations and the computation of the power spectrum

In this section I briefly describe the L-BASICC II ensemble of N-Body simulations used in my analysis and give some technical details about the methodology to compute the power spectra from these simulations. The basic equations used to compute the power spectrum can be found in Appendix A.1.

4.1.1 The L-BASICC II N-Body simulations

I use an ensemble of 50 moderate resolution, very large volume dark matter N-Body simulations called L-BASICC II (Angulo et al., 2008; Sánchez et al., 2008). These are analogues to the L-BASICC simulations used in Angulo et al. (2008) and represent the evolution of the dark matter density field in a universe characterised by a flat Λ CDM cosmology consistent with the constraints on cosmological parameters obtained from the combination of CMB and LSS information of Sánchez et al. (2006) and Spergel et al. (2007). The values of the cosmological parameters and other specifications of the simulations are listed in Table 4.1.

matter density	Ω_m	0.237	Table 4.1: Cosmological parameters and specifications of the L-BASICC II simulations.
baryonic density	Ω_b	0.041	
scalar spectral index	n_s	0.954	
Amplitude of density fluctuations	σ_8	0.77	
Hubble constant	H_0	$73.5 \text{ km s}^{-1} \text{ Mpc}^{-1}$	
Number of particles	N_p	448^3	
Particle mass	M_p	$1.75 \times 10^{12} h^{-1} M_\odot$	
Softening length	ϵ	$200 h^{-1} \text{ kpc}$	
Comoving box side		$1340 h^{-1} \text{ Mpc}$	
Comoving volume		$2.41 h^{-3} \text{ Gpc}^3$	
Total volume of the ensemble		$120 h^{-3} \text{ Gpc}^3$	

	$z = 0$	$z = 0.5$	$z = 1$	Table 4.2: Mass limits in units of $10^{13} h^{-1} M_\odot$ for the three halo sub catalogues at the three redshift outputs of the simulations. The limits at $z=0$ are the same as in Sánchez et al. (2008)
1	$M < 3.5$	$M < 2.9$	$M < 2.6$	
2	$3.5 \leq M < 5.95$	$2.9 \leq M < 4.65$	$2.6 \leq M < 3.8$	
3	$M \geq 5.95$	$M \geq 4.65$	$M \geq 3.8$	

The position and the velocity of all the particles in the simulations are stored in three snapshots at redshifts $z = 0, 0.5$ and 1 . Halo catalogues are constructed from the dark matter distribution at each redshift using a *Friend-of-Friends* algorithm (FoF, Davis et al., 1985), with a linking length parameter $b = 0.2$ and selecting all the haloes with more than 10 particles, which corresponds to a minimum halo mass of $1.75 \times 10^{13} h^{-1} M_\odot$.

From each halo catalogue I extract three sub-samples selected according to the mass limits shown in Table 4.2 (all the value are in units of $10^{13} h^{-1} M_\odot$). I choose these limits in order to include about half of the total number of haloes in mass range 1 and the remaining equally divided between samples 2 and 3. The number of haloes (N_h) and the corresponding *shot noise* terms ($1/\bar{n}$), a scale independent poisson term arising from the discretization of the density field (see also Appendix A.1), for each mass bin at each redshift are given in Table 4.3.

4.1.2 Power spectrum computation and shot noise

In order to compute the power spectra, the dark matter particles or haloes are assigned to a grid of 1008^3 cells using the *triangular shaped cloud* (TSC) as *mass assignment scheme* (MAS). I then compute the Fourier transform of the obtained density field using a fast Fourier transform (FFT) algorithm as implemented by the free software FFTW¹ (Fastest Fourier Transform in the West, Frigo & Johnson, 2005). I correct the amplitude of the Fourier modes for the effects of the MAS as in the first line of equation (A.4b), spheri-

¹<http://www.fftw.org/>

bin	$z = 0$		$z = 0.5$		$z = 1$	
	N_h	$1/\bar{n}$	N_h	$1/\bar{n}$	N_h	$1/\bar{n}$
tot	465903	5164	294204	8178	143531	16764
1	262232	9175	151976	15832	69457	34642
2	101825	23630	71551	33628	36852	65291
3	101846	23625	70678	34043	37221	64644

Table 4.3: Number of haloes (N_h) and shot noise term ($1/\bar{n}$, in units of $h^{-3} \text{Mpc}^3$) for the total halo sample and the three mass bins defined in Table 4.2 for redshift 0, 0.5 and 1.

cally average them in shells of thickness $\Delta k = 2\pi/L = 0.0047 h \text{Mpc}^{-1}$ and subtract the shot noise contribution $1/\bar{n}$. For this configuration the *Nyquist wave number* is $k_N = 2.36 h \text{Mpc}^{-1}$ and the computed power spectrum is exact for $k < 67\%k_N = 1.58 h \text{Mpc}^{-1}$ (see Appendix A.1 for more details). To obtain the redshift space power spectrum, I shift the position of the dark matter particles or haloes along one axis, converting their peculiar velocity into a displacement in comoving coordinates.

I compute the real and redshift-space power spectra of the dark matter distribution (P_{DM}) at redshift 0, 0.5 and 1, and the corresponding power spectra of the total halo catalogues and the three mass sub-samples, which I label as P_{tot}^h , P_{11}^h , P_{22}^h and P_{33}^h respectively. I also compute the cross power spectra for the three possible combinations of the mass bins at each redshift (P_{12}^h , P_{13}^h and P_{23}^h).

The FoF algorithm, used to create the halo catalogues, is intrinsically exclusive: two haloes must be separated by a distance larger than the sum of their radii or they would be identified as a single more massive halo. This introduces an exclusion effect in the halo catalogues which is visible in both the correlation functions and the power spectra of these samples. In the correlation function the exclusion effect is clearly visible at small scales, where it becomes negative. As an example, the left panel of Figure 4.1 shows the mean correlation function obtained from the total halo catalogue at $z = 0$ in our ensemble of simulations: after reaching its maximum value at $r \approx 2 h^{-1} \text{Mpc}$, it decreases converging to $\xi = -1$ as $r \rightarrow 0$. The right panel of Figure 4.1 shows the mean power spectrum with and without the shot noise subtracted (solid and long-dashed lines, respectively) for the same sample and redshift. The dot-dashed lines show their corresponding $1 - \sigma$ variance. The shot noise amplitude is indicated by the horizontal dashed line. It is important to notice that when the shot noise is subtracted, the power spectrum becomes negative for $k \gtrsim 1 h \text{Mpc}^{-1}$. Tests show that this feature is independent of the shot noise amplitude or the dimension of the grid used for the FFT. This clearly points to the fact that in the presence of the exclusion effect the noise is not Poisson anymore and is possibly scale-dependent.

The problem of the existence and impact of the exclusion effect in the power spectrum has been already addressed in previous analyses. Smith et al. (2007) point out that the exclusion effect may give rise to a scale dependent noise term which may lead to a misinterpretation of the shape of the power spectrum; Casas-Miranda et al. (2002) and Manera & Gaztanaga (2009) found that biased objects present non Poisson noise. Since the understanding and modelling of the influence of the exclusion effect on the power spectrum is beyond the scope of this thesis, I do not address specifically this problem here. Nonethe-

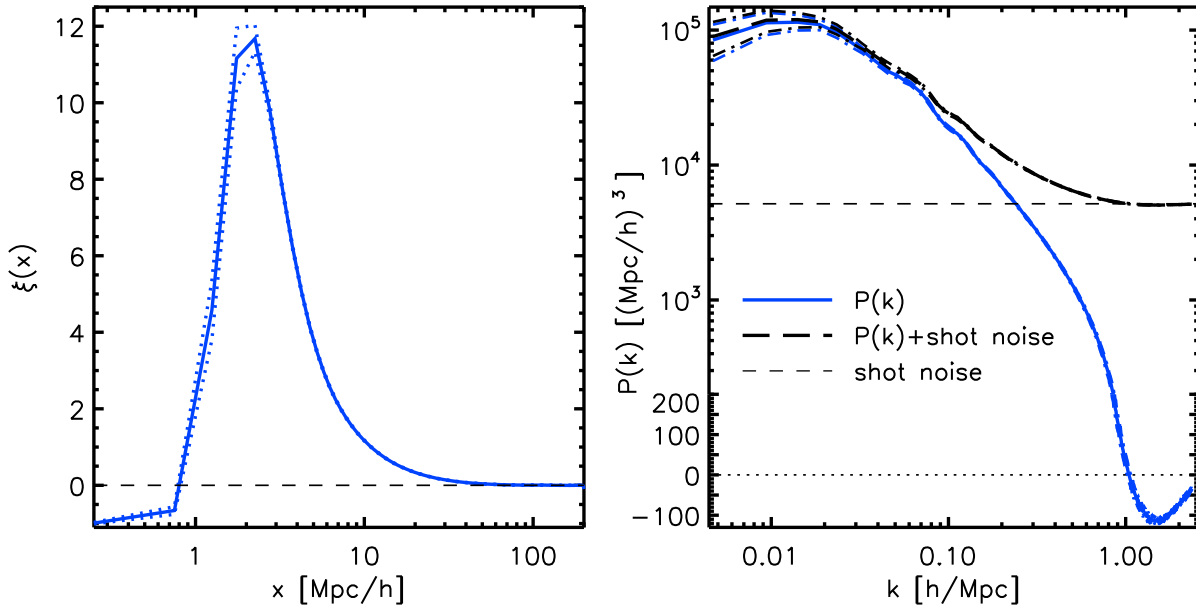


Figure 4.1: *Left* panel: log-linear scaling of the mean real-space correlation function $\xi(x)$ (solid line) of the total halo sample from the ensemble of simulations. The dotted lines indicate the variance from the different realisations. The signature of the exclusion effect in the halo sample can be clearly seen at $r < 2 h^{-1} \text{Mpc}$. *Right* panel: mean power spectrum with and without the shot noise subtracted (solid and long-dashed lines, respectively) from the ensemble of simulations and their corresponding $1\text{-}\sigma$ variance (dot-dashed lines) for the total halo sample. The amplitude of the shot noise is indicated by the horizontal dashed line. To enhance the negative part of the power spectrum at small scales, I use linear vertical axis for $P(k) < 200 h \text{Mpc}^{-1}$ instead of logarithmic.

less, as is explained Section 4.2, the model of the shape of the power spectrum contains few free parameters that can partially absorb possible deviations from white noise. This issue is addressed again in Section 4.3.4.

4.2 Modelling the full shape of the power spectrum

The increasing volume of the new large galaxy redshift surveys requires accurate models of the LSS observations in order to extract the maximum amount of information from the data without introducing systematic effects. In Section 2.2, I introduced the basic concepts of renormalised perturbation theory and how it can improve over standard PT in describing the dark matter power spectrum at non-linear scales. However, in order to describe the galaxy clustering, it is necessary to include into the modelling the distortions due to bias and redshift space effects.

As a first step towards a phenomenological model of the power spectrum, I introduce two approximations in the two terms in the right hand side of equation (2.25). First I

assume that the propagator is described by the growth factor times a Gaussian damping

$$G(k, z) = D_1(z) \exp \left[- \left(\frac{k}{\sqrt{2}k_\star} \right)^2 \right], \quad (4.1)$$

where the scale k_\star is given by equation (2.24). Secondly I reduce the full mode coupling $\sum_{n=2}^{\infty} P_{n\text{MC}}(k, \tau)$ to its lowest order contribution: P_{22} from equation (2.23a). Equation (4.1) is almost exact in the large- k limit and is a good approximation for the propagator for small values of k .

Crocce & Scoccimarro (2008) proposed a model for the large scale correlation function motivated by the RPT formalism. In this ansatz the correlation function is given by

$$\xi_{\text{NL}}(r) = b^2 \left[\xi_{\text{L}}(r) \otimes e^{-(k_\star r)^2} + A_{\text{MC}} \xi_{\text{L}}'(r) \xi_{\text{L}}^{(1)}(r) \right], \quad (4.2)$$

where b , k_\star and A_{MC} are treated as free parameters, and the symbol \otimes denotes a convolution. The factor b encodes the change in the large scale amplitude caused by the linear bias b_1 and the Kaiser factor S_{lin} ; A_{MC} quantifies the relative amplitude of the mode coupling term with respect to the linear one. ξ_{L}' is the derivative of the linear correlation function and $\xi_{\text{L}}^{(1)}(r)$ is defined by

$$\xi_{\text{L}}^{(1)}(r) \equiv \hat{r} \cdot \nabla^{-1} \xi_{\text{L}}(r) = \frac{1}{2\pi^2} \int dk k P_{\text{L}}(k) j_1(kr), \quad (4.3)$$

with $j_1(y)$ denoting the spherical Bessel function of order one. The two terms in equation (4.2) are, respectively, the linear correlation function convolved with the Fourier transform of the approximated propagator of equation (4.1) and the leading order contribution to ξ_{MC} from the lowest order approximation of the mode coupling power spectrum of equation (2.23a). Sánchez et al. (2008) compared this model with the results of N-body simulations and found that it is able to give an accurate description of the full shape of the correlation function, including the effects of bias and redshift space distortions, for volumes up to two orders of magnitude larger than present day datasets. Sánchez et al. (2009) successfully used this model to obtain constraints on cosmological parameters from the correlation function of a sample of luminous red galaxies drawn from the data release 6 of the SDSS as measured by Cabré & Gaztañaga (2009a).

In this analysis, I follow the same approach and model the non-linear power spectrum as

$$P(k, z) = b^2 \left[e^{-(k/k_\star)^2} P_{\text{lin}}(k, z) + A_{\text{MC}} P_{22}(k, z) \right], \quad (4.4)$$

and treat b , k_\star and A_{MC} as free parameters. In the next section I show that this model allows to obtain unbiased constraints on the dark energy equation of state parameter by accurately describing the full shape of the power spectrum measured in real and redshift space.

Panel *a* of Figure 4.2 shows the linear theory power spectrum (solid line) and $P_{22}(k)$ (dashed line) computed assuming the cosmological parameters of the L-BASICC II simulations. Panel *b* shows $P_{\text{L}}(k)$ divided by a reference power spectrum without BAO (Eisenstein & Hu, 1998) and $P_{22}(k)$ divided by the corresponding term derived applying equation

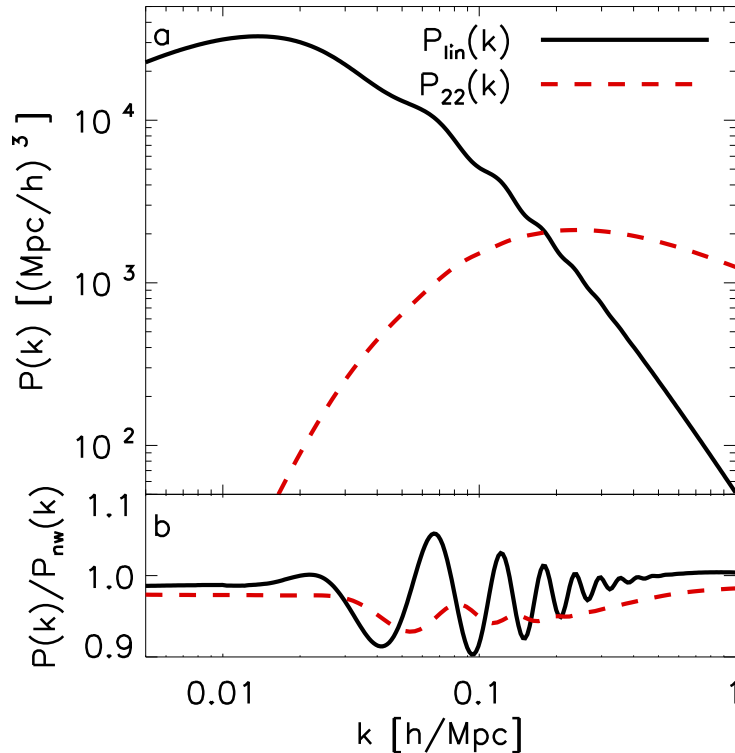


Figure 4.2: Panel *a*: Linear theory (solid line) and lowest order non-linear (dashed line) power spectra. Panel *b*: ratio between the power spectra of panel *a* and reference ones without oscillations. $P_{22}(k)$ shows small oscillations out of phase with respect to $P_{\text{lin}}(k)$, generating a net shift of the BAO peaks when summed.

(2.23a) to the smooth power spectrum. Both power spectra show oscillations, although in $P_{22}(k)$ they have a smaller amplitudes and are out of phase with respect to the ones in $P_L(k)$. When these two terms are summed as in equation (4.4), the BAOs are shifted towards smaller scales with respect to the ones in the linear power spectrum, in agreement with the findings of Crocce & Scoccimarro (2008), Sánchez et al. (2008) and Smith et al. (2008).

$P_{22}(k)$ does not have the same shape as $P_{2\text{MC}}(k)$: the latter in fact decreases faster than the former and at $k \sim 0.15 - 0.2 h \text{ Mpc}^{-1}$ it is roughly 1.5 – 2 times smaller. But at those scales the amplitude of the three mode coupling, $P_{3\text{MC}}(k)$, is already around $1/4 - 1/2$ of $P_{2\text{MC}}(k)$ and should be included in the model, as can be seen comparing Figures 4.2 and 2.2. $P_{22}(k)$ is thus somewhat larger than $P_{2\text{MC}}(k) + P_{3\text{MC}}(k)$ and the difference becomes more and more important with increasing wave number. I will come back to this again in section 4.3, where I discuss the range of scales in which the model of equation (4.4) can be applied to a measurement of the power spectrum.

It can be expected that this model is less efficient at describing the shape of the power spectrum in redshift-space than in real-space. In fact, in equation (4.4) I do not include redshift space distortions explicitly and I let the free parameters compensate some of their effects. The lack of a model for the redshift space distortions will be particularly visible for the dark matter, since the associated scale dependence is stronger than for the haloes (Scoccimarro, 2004; Angulo et al., 2008).

4.3 Model in practice and discussion

In this section I test whether or not the model described in section 4.2 can give an accurate description of the power spectrum including the effects of non-linear evolution, redshift space distortions and bias. In section 4.3.1 I describe the test that I implement to determine if the model returns unbiased constraints on the dark energy equation of state parameter w_{DE} . Sections 4.3.2-4.3.4 describe the results obtained when each of these scale dependent effects is included in the measurement of the power spectrum.

4.3.1 Testing the model

When measuring the power spectrum from an observational dataset, it is necessary to assume a fiducial cosmology in order to map the observed galaxy redshifts and angular positions into comoving distances. Under the assumption that a wide solid angle is covered, different choices of the parameters change the distances between objects, which modify the shape of the power spectrum. However, it is possible to take into account these distortions by rescaling the power spectrum from the fiducial cosmology to the true one multiplying the wave number by the factor (Eisenstein et al., 2005):

$$\alpha = \frac{D_{\text{V}}^{\text{fid}}(z)}{D_{\text{V}}^{\text{model}}(z)} \quad (4.5)$$

and the amplitude of the power spectrum by $1/\alpha^3$. The *effective distance* $D_{\text{V}}(z)$ to the redshift z is

$$D_{\text{V}}(z) = \left[D_{\text{A}}^2(z) \frac{z}{H(z)} \right]^{1/3}, \quad (4.6)$$

with $D_{\text{A}}(z)$ the comoving angular diameter distance of equation 3.6.

Following Angulo et al. (2008) and Sánchez et al. (2008), I consider here the simple case in which all cosmological parameters, except w_{DE} , are fixed to the values in Table 4.1. In this case equation (4.5) allows to relate univocally the dark energy equation of state with the wave number stretch parameter α (Huff et al., 2007). Therefore, from the constraints on α , as obtained from the mean power spectra of the L-BASICC II simulations, and using equation (4.5), it is possible to relate the value of α with constraints on the dark energy equation of state parameter. This relation is shown in figure 12 from Angulo et al. (2008).

I consider α free and, using a *Markov chain Monte Carlo* technique (MCMC, Gilks et al., 1996; Christensen & Meyer, 2000), I explore the parameter space defined by $\theta = (k_{\star}, b, A_{\text{MC}}, \alpha)$. I assume that the likelihood function follows a Gaussian form

$$\mathcal{L} \propto \exp \left[-\frac{1}{2} \chi^2(\theta) \right], \quad (4.7)$$

where

$$\chi^2(\theta) = [\mathbf{d} - \mathbf{t}(\theta)]^T \mathbf{C}^{-1} [\mathbf{d} - \mathbf{t}(\theta)] \quad (4.8)$$

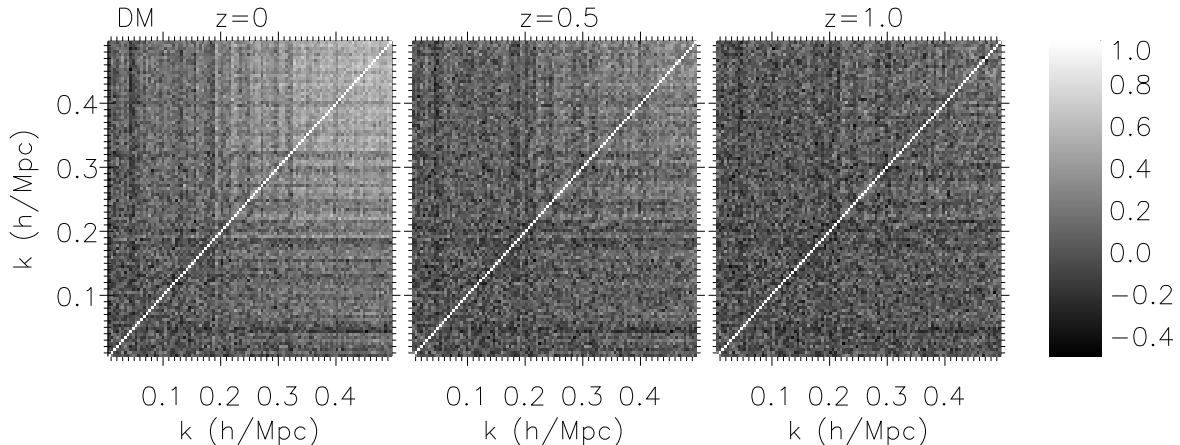


Figure 4.3: Correlation matrix $C_{ij}/\sqrt{C_{ii}C_{jj}}$, where C_{ij} are the elements of the covariance matrix \mathbf{C} , for the real-space dark matter power spectra at $z = 0$ (left), $z = 0.5$ (center) and $z = 1$ (right). At $z = 1$ the correlation matrix is close to diagonal, but at lower redshifts, when non-linearities become increasingly important, a significant correlation between different modes appears and becomes more important for larger scales, i.e. smaller k , as the redshift decreases. A similar result is obtained for the redshift-space power spectrum.

is the standard χ^2 , in which \mathbf{d} is an array containing the fitted data, in this case the computed power spectrum, $\mathbf{t}(\theta)$ contains the model computed for a given set of parameters θ and \mathbf{C} is the covariance matrix of the measurement.

I compute the covariance matrix \mathbf{C} for the dark matter and the halo power spectra as

$$C_{ij} = \frac{1}{N_{\text{real}} - 1} \sum_{l=1}^{N_{\text{real}}} [P_l(k_i) - \bar{P}(k_i)] [P_l(k_j) - \bar{P}(k_j)], \quad (4.9)$$

where $P_l(k_i)$ corresponds to the measurement of the power spectrum at the i -th k -bin in the l -th realisation and $\bar{P}(k_i)$ corresponds to the mean power spectrum from the ensemble at the same wavenumber.

Figures 4.3 and 4.4 show the correlation matrices $C_{ij}/\sqrt{C_{ii}C_{jj}}$ of the power spectra of the real-space dark matter and total halo samples respectively. In both figures, the three panels correspond, from left to right, to $z = 0$, 0.5 and 1. In all cases I observe that the correlation between different modes, due to non linear mode coupling, is stronger at $z = 0$ and decreases at increasing redshift. At $z = 0$ the correlation matrix of the total halo sample shows strong correlations for $k \gtrsim 0.1 h \text{ Mpc}^{-1}$. In order to obtain robust constraints on α these correlations must be included when fitting our model to the L-BASICC II mean power spectrum. For more detailed studies on the covariance of the power spectrum using theoretical models and large numerical simulations see, e.g., Hamilton et al. (2006), Smith (2009) and Takahashi et al. (2009).

The MCMC requires a prior knowledge of the parameter space. I assume flat priors given by

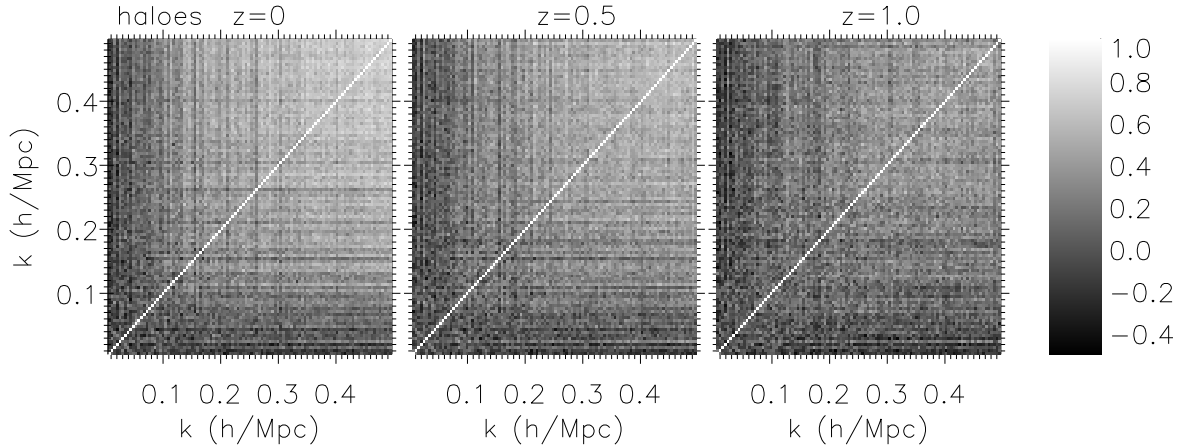


Figure 4.4: Same as in Figure 4.3 but for the total halo samples at $z = 0$ (left), $z = 0.5$ (center) and $z = 1$ (right) in real space. As for dark matter, the mode coupling becomes more important at larger scales as the redshift decreases. A similar result is obtained for the redshift space catalogue and for the other halo catalogues.

- $0 h \text{ Mpc}^{-1} < k_{\star} < 0.35 h \text{ Mpc}^{-1}$,
- $0 \leq A_{\text{MC}} < 10$,
- $0.5 \leq \alpha < 1.5$.

The bias parameter b is analytically marginalised over an infinite flat prior using equation F2 in Lewis & Bridle (2002). In order to obtain an estimate of the amplitude of the model power spectrum, I compute a value of b and its variance by maximizing the likelihood function of equation (4.7) while the other parameters are kept fixed to their mean values obtained from the MCMC.

4.3.2 Non-linear evolution

The circles in Figure 4.5 show the mean real-space dark matter power spectra from the L-BASICC II simulations at $z = 0, 0.5$ and 1 (panels *a*, *b* and *c* respectively). Dot-dashed lines show the corresponding variances from the estimates in the different realizations. In order to highlight the signature of the acoustic oscillations, Figure 4.6 shows, with the same symbols, the power spectra divided by a smooth linear theory power spectrum without BAOs computed using the fitting formulas of Eisenstein & Hu (1998). The comparison with the linear power spectrum (dashed lines) shows that non linearities change the broad band shape of the power spectrum at small scales and damp the BAO feature. I explore the constraints on the stretch parameter obtained by applying the model described in section 4.2 to these measurements.

The lines in the panels *a*, *b* and *c* of Figure 4.7 show the mean value of α obtained from the measurements at $z = 0, 0.5$ and 1 (solid lines), together with its correspondent 68%

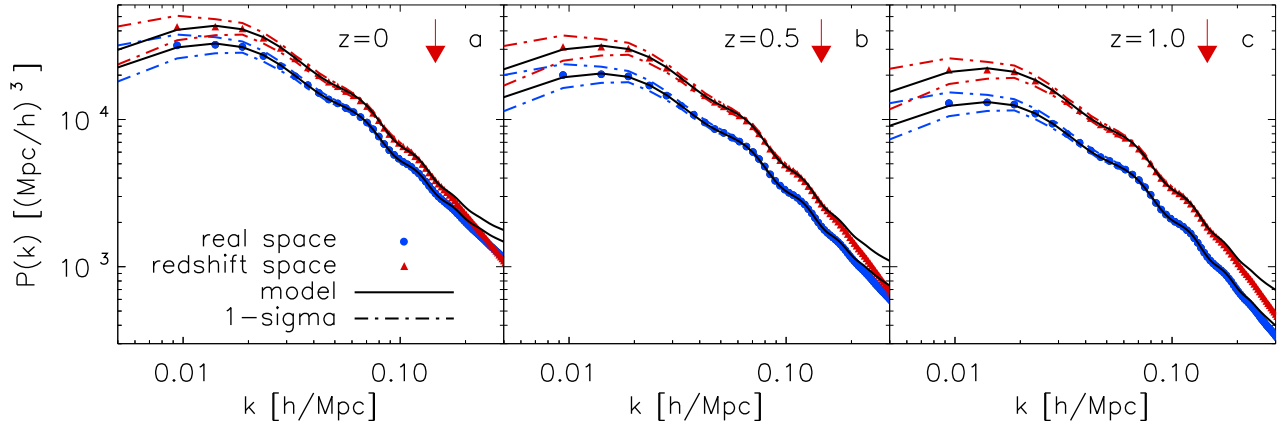


Figure 4.5: Mean power spectra computed from the simulations (circles for real space and triangles for redshift space), their variance (dash-dotted lines) and the model power spectrum as obtained through the fitting (solid lines) as function of the wavenumber in comoving units for the dark matter catalogue at redshift 0, 0.5 and 1.0 (left, centre and right respectively), in log-log scaling. The maximum wavenumber used for the fit is $k_{\max} = 0.15 h \text{ Mpc}^{-1}$ and is indicated by the vertical arrow.

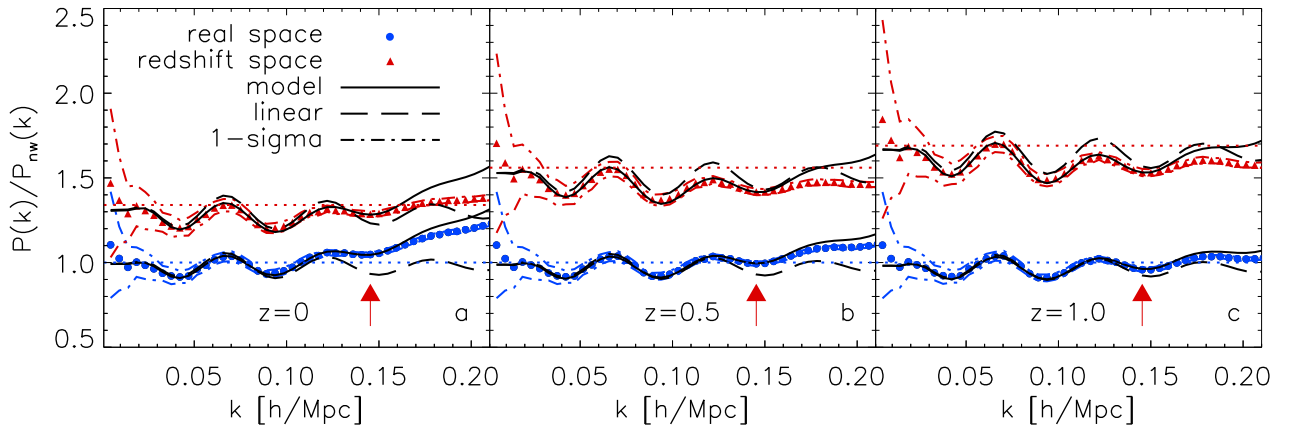


Figure 4.6: Power spectra of Figure 4.5 divided by a smooth reference power spectrum (Eisenstein & Hu, 1998) in order to enhance the BAO oscillations, in linear scaling. For comparison the linear power spectrum, divided by the smooth power spectrum, is shown (dashed lines). The upper horizontal lines are drawn to the values corresponding to the Kaiser boost factor (section 4.3.3 and Table 4.5). The smooth power spectrum is the same for all the plots. The maximum wavenumber used for the fit is $k_{\max} = 0.15 h \text{ Mpc}^{-1}$ and is indicated by the vertical arrow.

and 95% confidence levels (dot-dashed lines), as function of k_{\max} , the maximum value of k included in the fit. As smaller scales (larger values of k_{\max}) are taken into account, the width of the allowed region for α decreases due to the larger number of modes included in

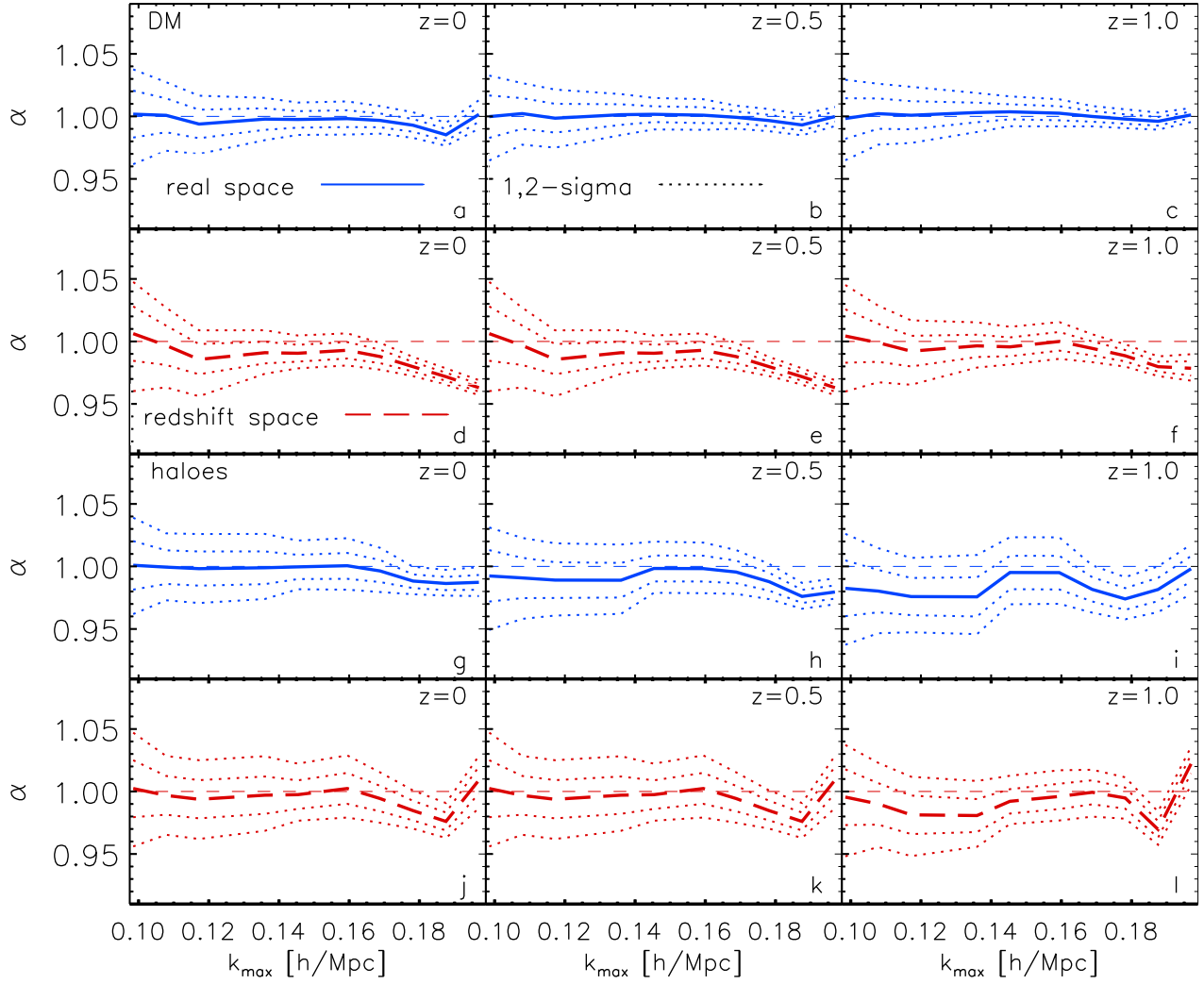


Figure 4.7: Mean value of α obtained from the MCMC (blue solid line for real space, red long-dashed line for redshift space), $1, 2 - \sigma$ confidence level (dotted lines) as function of k_{\max} for dark matter (real space: panels *a*, *b* and *c*; redshift space: panels *d*, *e* and *f*) and the total halo catalogue (real space: panels *g*, *h* and *i*; redshift space: panels *j*, *k* and *l*) at $z=0, 0.5, 1$ from left to right. The horizontal dashed lines indicate $\alpha = 1$.

the fit. At $z = 0$, the mean value of α remains consistent with 1 at a $1 - \sigma$ level for $k_{\max} \lesssim 0.16 h \text{ Mpc}^{-1}$, with $\alpha = 0.999 \pm 0.007$ for $k_{\max} = 0.15 h \text{ Mpc}^{-1}$. At higher redshifts the value of k_{\max} for which this holds increases, due to the smaller impact of non-linearities. The first row of the upper part of Table 4.4 lists the obtained values of α for $k_{\max} = 0.15 h \text{ Mpc}^{-1}$. The solid lines in Figures 4.5 and 4.6 show the model power spectrum of equation (4.4) computed using the mean values of the four parameters obtained for this range in k . This model is able to accurately describe the effects of non-linear evolution in both the broad-

	$z = 0$	$z = 0.5$	$z = 1$	
α_{real}	DM	0.999 ± 0.007	1.001 ± 0.006	1.001 ± 0.006
	tot	1.001 ± 0.011	0.995 ± 0.011	0.994 ± 0.014
	11	0.999 ± 0.014	1.006 ± 0.014	0.999 ± 0.017
	22	1.006 ± 0.017	1.006 ± 0.013	1.005 ± 0.023
	33	1.003 ± 0.016	0.997 ± 0.012	0.987 ± 0.016
	12	1.002 ± 0.013	1.004 ± 0.01	0.987 ± 0.015
	13	1.002 ± 0.01	0.991 ± 0.012	0.991 ± 0.018
	23	0.995 ± 0.013	1.004 ± 0.014	1.005 ± 0.013
α_{red}	DM	0.994 ± 0.007	1.001 ± 0.007	1.005 ± 0.008
	tot	1.002 ± 0.012	0.997 ± 0.01	0.987 ± 0.012
	11	0.999 ± 0.016	1.008 ± 0.016	0.998 ± 0.016
	22	1.007 ± 0.02	1.01 ± 0.018	1.006 ± 0.026
	33	0.998 ± 0.017	0.994 ± 0.014	0.981 ± 0.015
	12	1.002 ± 0.014	1.006 ± 0.012	0.982 ± 0.014
	13	1.008 ± 0.011	0.993 ± 0.012	0.978 ± 0.018
	23	0.997 ± 0.015	1.006 ± 0.014	1.006 ± 0.014

Table 4.4: Mean values of α and their $1\text{-}\sigma$ confidence levels as recovered from the mean dark matter and halo samples power spectra of the three redshifts outputs of the L-BASICC II simulations for $k_{max} = 0.15 h \text{ Mpc}^{-1}$. The upper part is for real space, the lower for redshift space. See Section 4.1.2 for the definition of the different samples listed in the second column.

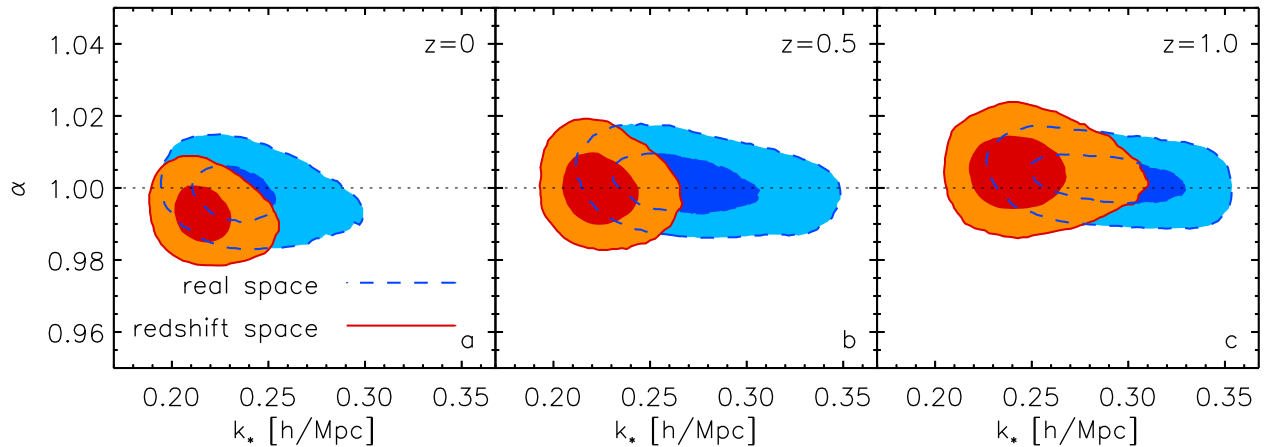


Figure 4.8: 1 and 2σ contours of likelihood map in the $k_* - \alpha$ plane obtained from the MCMC for dark matter at redshift 0 (left), 0.5 (centre), 1 (right) and $k_{max} = 0.15 h \text{ Mpc}^{-1}$. Background areas within dashed lines are for real space, foreground ones within solid lines are for redshift space.

band shape of the power spectrum and the damping of the acoustic oscillations, up to the maximum value of k included in the fit, which is indicated by a vertical arrow.

The dashed contours in Figure 4.8 show the two-dimensional marginalized constraints in the $k_* - \alpha$ plane obtained for $k_{max} = 0.15 h \text{ Mpc}^{-1}$ at $z = 0, 0.5$ and 1 (panels *a*, *b* and *c* respectively). The contours correspond to $\Delta\chi^2 = 2.3$ and 6.17 which, assuming a two-dimensional gaussian likelihood, are equivalent to the 68% and 95% confidence levels. This convention is used throughout the chapter. While the constraints on the stretch

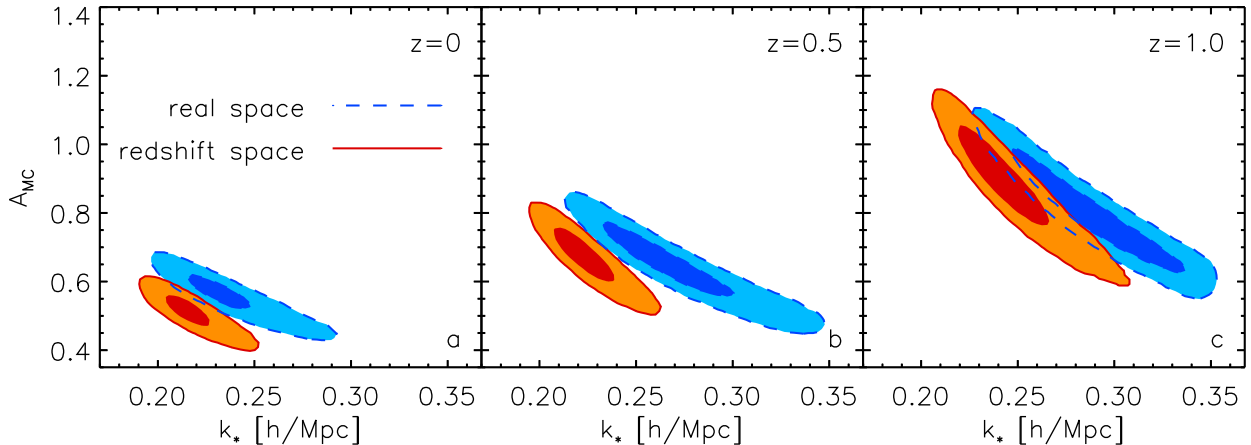


Figure 4.9: 1 and 2 σ contours of likelihood map in the $k_* - A_{\text{MC}}$ plane obtained from the MCMC for dark matter at $z = 0$ (left), 0.5 (centre), 1 (right) for $k_{\text{max}} = 0.15 h \text{ Mpc}^{-1}$. Background areas within dashed lines are for real space, foreground ones within solid lines are for redshift space.

parameter are very tight, there is a wide allowed region for k_* whose mean value is larger than the theoretical prediction of Equation (2.24). The mean value k_* shows a tendency to increase with redshift, as the BAO feature is less damped, but the allowed range for this parameter is too large to compare this evolution with $D_1(z)^{-1}$. The wide allowed range for k_* is caused by a strong degeneracy between this parameter and A_{MC} . This can be seen in Figure 4.9, which shows the two-dimensional constraints in the $k_* - A_{\text{MC}}$ plane for the dark matter power spectrum at $z = 0, 0.5$ and 1. The degeneracy arises because it is possible to provide a good description of the overall shape of the power spectrum by compensating an increase in the damping of the first term of equation (4.4) (a decrease of k_*) by increasing the amplitude of the mode coupling contribution (using a higher value of A_{MC}). Besides this, the value of A_{MC} obtained at $z = 0$ is about 30% smaller than the expected, confirming that the $P_{22}(k, z)$ is somewhat bigger than the sum of the RPT two and three mode coupling. This makes the value of k_* larger than the theoretical value of equation (2.24). In Figure 4.9 it is also noticeable that the values of A_{MC} increase with redshift due to the smaller relative amplitude of $P_{22}(k)$, which decreases as the growth factor squared, with respect to the linear power spectrum.

4.3.3 Redshift space distortions

If we were to observe dark matter directly and to measure its distribution using the redshift, the large scale amplitude of the measured power spectrum would be boosted by the coherent inflow towards overdensities and its shape would be damped by fingers-of-god. With numerical simulations, thanks to the knowledge of the position and velocity of dark matter particles, it is however possible to test the impact of redshift space distortions on the dark matter distribution.

Figure 4.5 shows the mean redshift-space dark matter power spectra (triangles) from the L-BASICC II simulations at $z = 0, 0.5$ and 1 (panels *a*, *b* and *c* respectively), together with the corresponding variances from our ensemble of simulations (dot-dashed lines). Figure 4.6 shows the same power spectra divided by a smooth linear theory power spectrum without acoustic oscillations. Since the smooth power spectrum is the same in real and redshift-space, it is possible to see both the increase in amplitude and the change in shape towards smaller scales in the latter case. In this section I test if the parameterization of the model of equation (4.4) contains enough freedom to take into account these distortions.

The dashed lines in the panels *d*, *e* and *f* of Figure 4.7 show the mean value of the stretch parameter obtained by applying the model of equation (4.4) to the mean redshift-space power spectra as a function of k_{\max} at $z = 0, 0.5$ and 1 , respectively. The dot-dashed lines indicate the corresponding 68% and 95% confidence levels. At $z = 1$, also when dealing with redshift-space information the model is able to recover constraints on α consistent with one at the $1 - \sigma$ level for $k < 0.18 h \text{ Mpc}^{-1}$. The constraints degrade at lower redshifts as non-linear redshift space distortions become more important and, at $z = 0$, our results are only marginally consistent with $\alpha = 1$. The first row of the lower part of Table 4.4 lists the constraints on α obtained for $k_{\max} = 0.15 h \text{ Mpc}^{-1}$. In all cases, the errors on this parameter increase with respect to the real-space case. In all the panels of Figures 4.5 and 4.6 the solid upper line shows the model power spectrum in redshift space with the parameters fixed to the mean value obtained from the MCMC. This decrease in accuracy is due to the combination of two facts: first, I do not include explicitly redshift space distortions in the model; second, the impact of fingers-of-god is very important and modifies substantially the mildly non-linear shape of the power spectrum.

The shaded contours within solid lines in Figure 4.8 show the two-dimensional 68% and 95% marginalized constraints in the $k_{\star} - \alpha$ plane obtained from the mean redshift-space power spectrum from the L-BASICC II simulations for $k_{\max} = 0.15 h \text{ Mpc}^{-1}$ at $z = 0$ (panel *a*), 0.5 (*b*) and 1 (*c*). As in the case of real-space, there is no degeneracy between these parameters. Redshift space distortions increase the damping of the BAO signal. This is reflected in the mean values of k_{\star} being systematically lower than the ones obtained from real-space data. Figure 4.9 shows the correspondent constraints in the $k_{\star} - A_{\text{MC}}$ plane. The scale-dependent effects introduced by redshift-space distortions cause these two parameters to follow a different degeneracy than in the real-space case although the qualitative behaviour is maintained.

Using equation (3.5), it is possible to compute the theoretical expectation value of the Kaiser boost factor, which for the dark matter case, where $b = 1$, is simply given as $S_{\text{lin}} = 1 + 2f/3 + f/5$. This value can be compared with the ratio of the real and redshift space power spectra, $S_{\text{fit}} = P_{\text{s}}(k, z)/P_{\text{r}}(k, z)$, directly measured from the L-BASICC-II simulations on large scales, where non-linear effects and scale dependent redshift space distortions are negligible. At linear order, these two power spectra are $P_{\text{r}}(k, z) \approx P_{\text{lin}}(k, z)$ and $P_{\text{s}}(k, z) \approx b_{\text{s}}^2 P_{\text{lin}}(k, z)$. Therefore, the value of S_{fit} can be obtained by computing the bias b_{s} of the redshift space power spectrum as described in Section 4.3.1. The values of S_{fit} obtained for the dark matter case are listed, together with the theoretical values S_{lin} , in Table 4.5. The three values of S_{lin} are also indicated in Figure 4.6 with the upper dotted

	b_{eff}	b	S_{lin}	S_{fit}	
$z = 0$	DM	1	1.003 ± 0.003	1.34	1.32 ± 0.01
	tot	1.89	1.89 ± 0.01	1.17	1.17 ± 0.01
	11	1.63	1.65 ± 0.01	1.20	1.20 ± 0.02
	22	1.90	1.84 ± 0.01	1.17	1.17 ± 0.02
	33	2.54	2.49 ± 0.01	1.12	1.12 ± 0.02
	12	1.76	1.75 ± 0.01	1.18	1.17 ± 0.02
	13	2.04	2.04 ± 0.01	1.16	1.17 ± 0.01
	23	2.20	2.12 ± 0.01	1.14	1.15 ± 0.02
$z = 0.5$	DM	1	0.999 ± 0.003	1.56	1.55 ± 0.01
	tot	2.73	2.65 ± 0.01	1.18	1.18 ± 0.01
	11	2.31	2.33 ± 0.01	1.22	1.22 ± 0.02
	22	2.59	2.57 ± 0.02	1.19	1.19 ± 0.02
	33	3.42	3.39 ± 0.02	1.14	1.14 ± 0.02
	12	2.45	2.45 ± 0.01	1.20	1.21 ± 0.02
	13	2.81	2.79 ± 0.01	1.18	1.18 ± 0.01
	23	2.98	2.95 ± 0.02	1.17	1.17 ± 0.02
$z = 1$	DM	1	0.996 ± 0.003	1.69	1.70 ± 0.01
	tot	3.87	3.80 ± 0.02	1.15	1.16 ± 0.01
	11	3.27	3.37 ± 0.02	1.18	1.20 ± 0.02
	22	3.58	3.67 ± 0.03	1.17	1.18 ± 0.03
	33	4.62	4.73 ± 0.03	1.13	1.14 ± 0.02
	12	3.42	3.50 ± 0.02	1.17	1.18 ± 0.02
	13	3.89	3.98 ± 0.02	1.15	1.15 ± 0.02
	23	4.07	4.18 ± 0.03	1.14	1.15 ± 0.02

Table 4.5: Effective linear bias (b_{eff}) computed from the halo model prescription, values of b obtained from the fit in real space as described at the end of section 4.3.1, theoretical linear Kaiser boost factors S_{lin} (equation 3.5) and Kaiser boost factors obtained from the fit (S_{fit}) at all redshift, for dark matter and all the halo catalogues. All the ranges correspond to the 68% confidence level.

lines. As can be seen the agreement between the theoretical and the recovered values is excellent at all redshifts.

4.3.4 Halo bias

Because of gravitational instability, dark matter clusters and forms haloes. In this section I analyse the accuracy of the model of equation (4.4) in describing their distribution, both in real and redshift space.

Real space

As described in Section 3.1, haloes form preferentially where the dark matter density is high and their mass tends to be larger in denser regions. The auto and cross halo power spectra for two mass bins i and j are, at linear order, related to the dark matter one by the scale-independent bias factor of equation (3.3):

$$P_{ij}^{\text{h}}(k, z) = b_{1\text{eff}}(z, i)b_{1\text{eff}}(z, j) P_{\text{DM}}(k, z). \quad (4.10)$$

The results of numerical simulations have shown that this simple picture is only valid on very large scales and that, due to the effects of non-linear evolution, halo bias is a strong function of both scale and halo mass (e.g. Smith et al., 2007; Angulo et al., 2008). These distortions must be carefully modelled in order to obtain unbiased constraints on cosmological parameters from the full shape of the halo power spectrum.

Circles and dot-dashed lines in Figure 4.10 show the mean real space power spectra and the corresponding variances at $z = 0$ for the total halo sample of the simulations, $P_{\text{tot}}^{\text{h}}(k)$ (panel *b*), the three mass bins described in section 4.1.1, $P_{11}^{\text{h}}(k)$, $P_{22}^{\text{h}}(k)$ and $P_{33}^{\text{h}}(k)$ (panels *a*, *d* and *g*), as well as their respective cross power spectra, $P_{12}^{\text{h}}(k)$, $P_{13}^{\text{h}}(k)$ and $P_{23}^{\text{h}}(k)$ (panels *c*, *e* and *f*). To increase the dynamical range of the plot, these power spectra have been divided by the same non-wiggle linear-theory power spectrum as in Figure 4.6.

I obtain constraints on the parameter space defined in section 4.3.1 for different values of k_{max} by applying the model of equation (4.4) to our measurements of the halo auto and cross power spectra. As an example, panels *g*, *h* and *i* of Figure 4.7 show the constraints on α as a function of k_{max} obtained from $P_{\text{tot}}^{\text{h}}(k)$ in real space for $z = 0, 0.5$ and 1 , respectively. The dot-dashed lines correspond to their 68% and 95% confidence levels. Due to the lower number densities of the halo samples, the variances of these power spectra are larger than for the dark matter case and increase with increasing redshift. This leads to an increase in the allowed regions for α with respect to the ones obtained using $P_{\text{DM}}(k)$. Despite this difference, these results show a similar qualitative behavior to the constraints obtained from the dark matter power spectrum, with a mean value consistent with $\alpha = 1$ up to $k \lesssim 0.15 h \text{Mpc}^{-1}$. The constraints on α obtained from the fits at different redshifts for $k_{\text{max}} = 0.15 h \text{Mpc}^{-1}$ are listed in the upper part of Table 4.4. The solid lines in Figure 4.10 show the model power spectrum of equation (4.4) computed using the mean values of the four parameters obtained for this value of k_{max} .

The background shaded areas within dashed lines in Figure 4.11 show the 68% and 95% confidence levels of the two-dimensional constraints in the $k_{\star} - \alpha$ plane as obtained using the mean auto and cross power spectra in real space for the different halo samples at $z = 0$. Although the allowed region is larger than in the dark matter case, the overall result here does not change: α is consistent with 1 and uncorrelated with both k_{\star} and A_{MC} , which makes this results robust. The constraints of the latter two parameters are quite weak due to the same degeneracy described in Section 4.3.2

In contrast to the behaviour found in the analysis of the dark matter power spectrum, when applied to the different halo samples the ability of the model to obtain unbiased constraints on the stretch parameter degrades with increasing redshift and at $z = 1$ they are only marginally consistent with $\alpha = 1$. This is related to the mass resolution of the L-BASICC II simulations: the smallest halo mass that can be resolved corresponds to $M_{\text{halo}} = 1.75 \times 10^{13} h^{-1} M_{\odot}$. While at $z = 0$ these haloes are moderately biased tracers of the underlying dark matter distribution, at $z = 1$ they are much rarer objects that reside in very dense, and thus highly non-linear, regions. Hence, an accurate description of the shape of the power spectrum of such high mass objects at high redshifts requires a more detailed model of the non-linear distortions than that of equation (4.4).

The shape of the cross power spectra $P_{12}^{\text{h}}(k)$, $P_{13}^{\text{h}}(k)$ and $P_{23}^{\text{h}}(k)$ is described as accurately

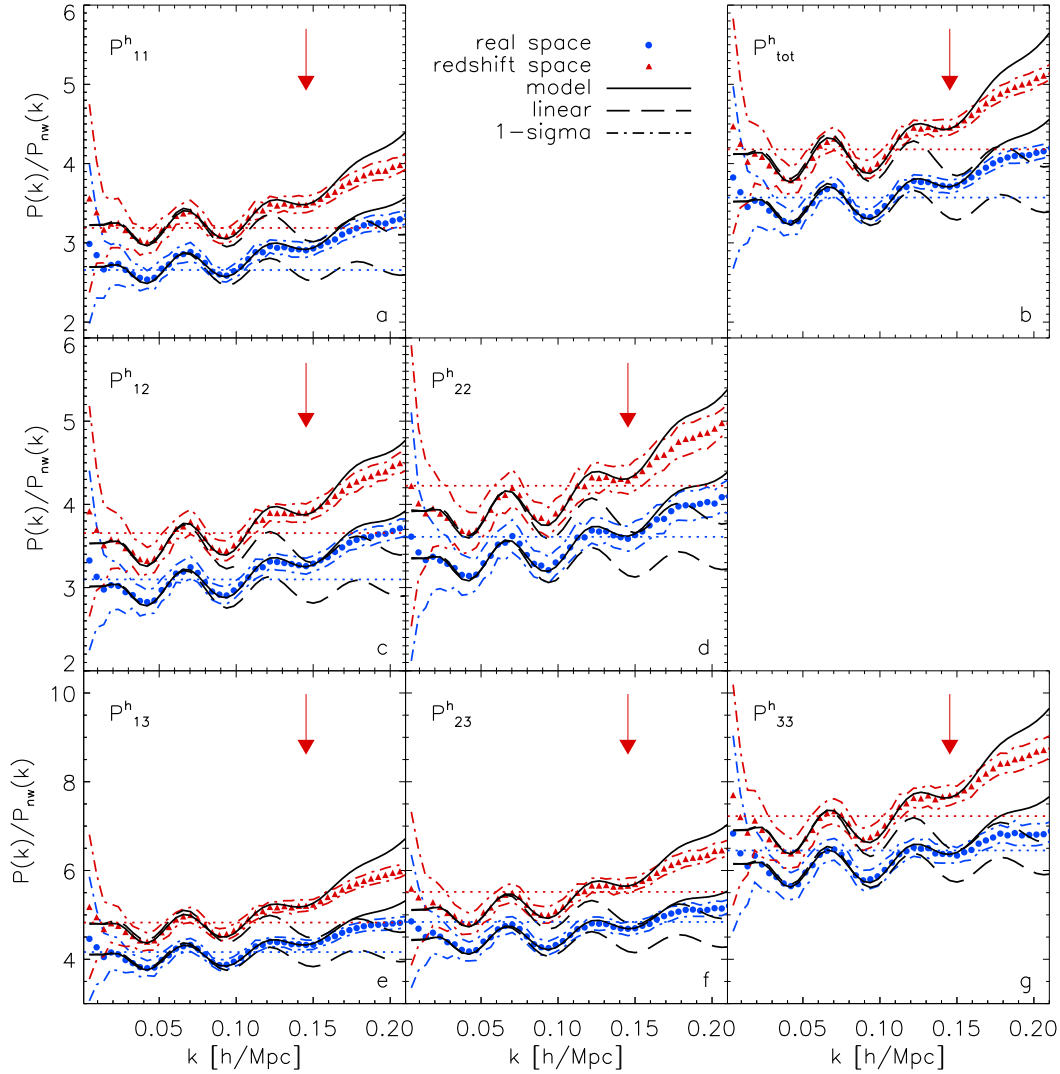


Figure 4.10: Mean power spectra computed from the simulations (circles for real space and triangles for redshift space), their variance (dash-dotted lines), the model power spectrum as obtained through the fitting (solid lines) and the linear power spectrum (dashed lines) as function of the wavenumber in comoving units at $z=0$ for the total halo catalog (*tot*), the three mass bins (*11*, *22* and *33*) and the three cross mass bins (*12*, *13* and *23*) divided by a smooth reference power spectrum (Eisenstein & Hu, 1998). Lower horizontal lines indicate the linear bias, b^2 for the halo mass bin as computed from the halo catalogue prescription, the upper one indicate $b^2 S_{\text{lin}}$ (Table 4.5). The maximum wavenumber used for the fit is $k_{\text{max}} = 0.15 h \text{ Mpc}^{-1}$ and is indicated by the vertical arrow.

as for the other four cases by the model of equation (4.4). As can be seen in Table 4.4, in all cases the constraints on α derived from these measurements are in good agreement with $\alpha = 1$ and are tighter than the ones derived from their corresponding auto power spectra.

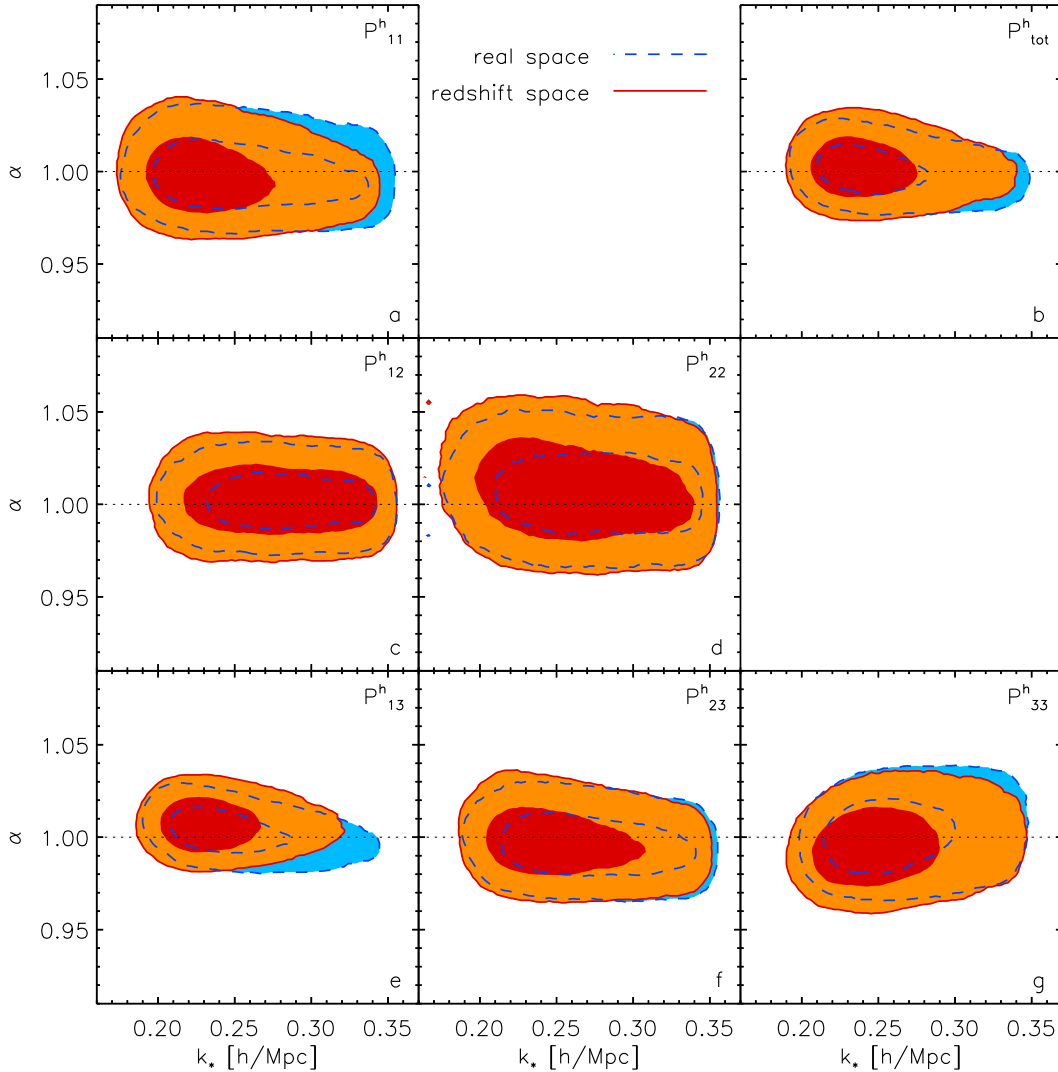


Figure 4.11: 1 and 2 σ contours of the likelihood map obtained from the MCMC in the $k_* - \alpha$ plane for all the haloes catalogues at redshift 0 for $k_{\max} = 0.15 h \text{ Mpc}^{-1}$. Background areas within dashed lines are for real space, foreground ones within solid lines are for redshift space.

As stated in Section 4.1.2, the halo catalogues are affected by the exclusion effect introduced by the Friend-of-Friends algorithm used to identify them. To account for a possible difference in the large scale amplitude of the shot-noise as could be caused by this effect, I repeat the analysis adding a constant term to the model of equation (4.4) which I allow to vary over a wide flat prior. The results indicate that such a term is degenerate with k_* and A_{MC} , while the constraints of α are not affected.

I measure the value of b from all the real space halo power spectra at the three redshifts as described at the end of Section 4.3.1. These values are listed in corresponding column

in Table 4.5. The recovered b^2 is shown by the lower dotted lines in Figure 4.10. Using the linear bias prescriptions of equations (3.3) and (3.4) I compute the effective bias for the halo mass bins listed in Table 4.3: the third column of Table 4.5 lists the effective bias as $b_{\text{eff}} = b_{1\text{eff}}(z, i)$, for $i = \text{tot}, 1, 2, 3$ and $b_{\text{eff}} = \sqrt{b_{1\text{eff}}(z, i)b_{1\text{eff}}(z, j)}$, for $i, j = 1, 2, 3$. The values of b and b_{eff} show a reasonable agreement with the measurements from the simulation with the exception of the high mass sample, for which the mass function is not sufficiently accurate (e.g. Warren et al., 2006).

Redshift space

Redshift space distortions modify the amplitude and shape of the halo power spectra less strongly than in the dark matter case (Smith et al., 2007; Angulo et al., 2008; Matsubara, 2008b). This comes clear when comparing the redshift space halo power spectra at $z = 0$, triangles in Figure 4.10, with the real space counterpart (circles) and with the dark matter power spectra in Figure 4.6. The other two redshifts investigated show the same trend.

On large scales, the impact of the Kaiser effect is reduced because the increase of the clustering signal due to the coherent inflow towards denser regions is relatively less important when $b_1 > 1$ than for values smaller than unity. This picture agrees with the theoretical prediction of equation (3.5), whose values for the halo auto and cross power spectra at $z = 0, 0.5$ and 1 are shown in the second to last column in Table 4.5. The values S_{lin} are computed using b_{eff} , but the results are very similar if it is substituted with the fitted real space bias b_r . The increase in amplitude is of the order of 15-20% and decreases with mass and with increasing redshift.

As already described in Section 3.1, fingers-of-god are caused by random motion of particles within bound structures. In haloes this effect is greatly reduced as their peculiar motion is small.

Panels j , k and l of Figure 4.7 shows the constraints on α as a function of k_{max} obtained from $P_{\text{tot}}^{\text{h}}(k)$ in redshift space for $z = 0, 0.5$ and 1 , respectively. The two-dimensional marginalised constraints in the $k_{\star} - \alpha$ plane obtained by applying the model of equation (4.4) with $k_{\text{max}} = 0.15 h \text{ Mpc}^{-1}$ to the seven redshift space halo power spectra at $z = 0$ are illustrated in Figure 4.11. From both figures it is clear that the difference between real and redshift space constraints obtained for the haloes is less significant than in the dark matter case, which agrees with the expectation described above. As before the constraints on k_{\star} are broaden due to the degeneracy between this parameter and A_{MC} ; nonetheless k_{\star} seems to prefer smaller values in redshift space, in agreement with the more significant damping of the BAO features.

From the fitted real and redshift space bias parameters in the model, b_r and b_s , I can measure the Kaiser boost factor as $S_{\text{fit}} = b_s^2/b_r^2$. These values are listed in the last column of Table 4.5 and they show a remarkable agreement with the theoretical predictions. The upper dotted lines in Figure 4.10 correspond to the value of $b_{\text{eff}}^2 S_{\text{lin}}$.

Chapter 5

Cosmological Parameters

Here I apply the model described and tested in the previous chapter to the measured power spectrum of a luminous red galaxy sample extracted from the seventh data release of the Sloan Digital Sky Survey (Abazajian et al., 2009). In Section 5.1 I describe the galaxy sample and the mock catalogues that we use to estimate the errors. Their power spectra are shown in Section 5.2. Section 5.3.1 illustrates the five cosmological scenarios that I explore combining the galaxy power spectrum with the data from the cosmic microwave background, type 1a supernovae and an accurate measurement of the local Hubble parameter. In Section 5.3.2 I explain briefly how the cosmological parameters are extracted. In Section 5.3.3 I test the model against the mock catalogues power spectrum. Section 5.4 shows the main results of this chapter, the cosmological parameters obtained combining the different experiments for the five models explored. Finally in Section 5.5 I compare my results with similar works recently published. This chapter based on Montesano et al. (2011).

5.1 The galaxy sample and the mock catalogues.

In this section I describe the galaxy sample (Section 5.1.1) and the mock catalogues (Section 5.1.2) that I use.

5.1.1 The luminous red galaxy sample from the 7th data release of SDSS

The data release 7 (DR7, Abazajian et al., 2009) is the last data release of the second phase of SDSS, know as SDSS-II. From the 929,555 galaxies, whose spectra have been measured, we use the subsample of luminous red galaxies (LRGs, Eisenstein et al., 2001) presented in Kazin et al. (2010) and publicly available¹. The catalogue contains 89,791 LRGs, in the redshift range $0.16 < z < 0.44$ ($\bar{z} = 0.314$), from the large contiguous area of 7646 deg^2

¹<http://cosmo.nyu.edu/~eak306/SDSS-LRG.html>

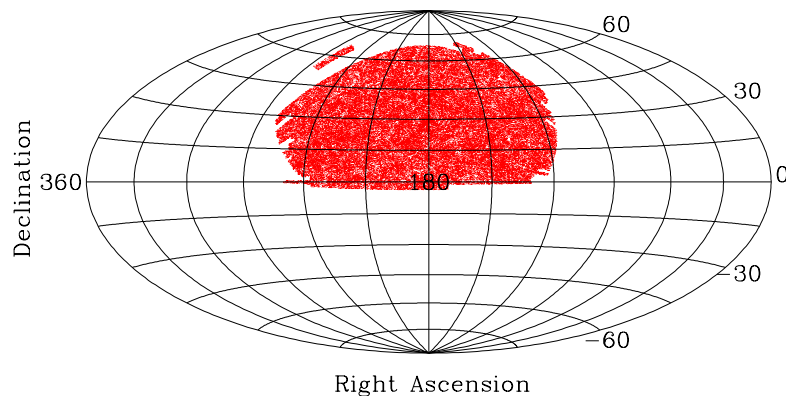


Figure 5.1: Angular distribution of the luminous red galaxies

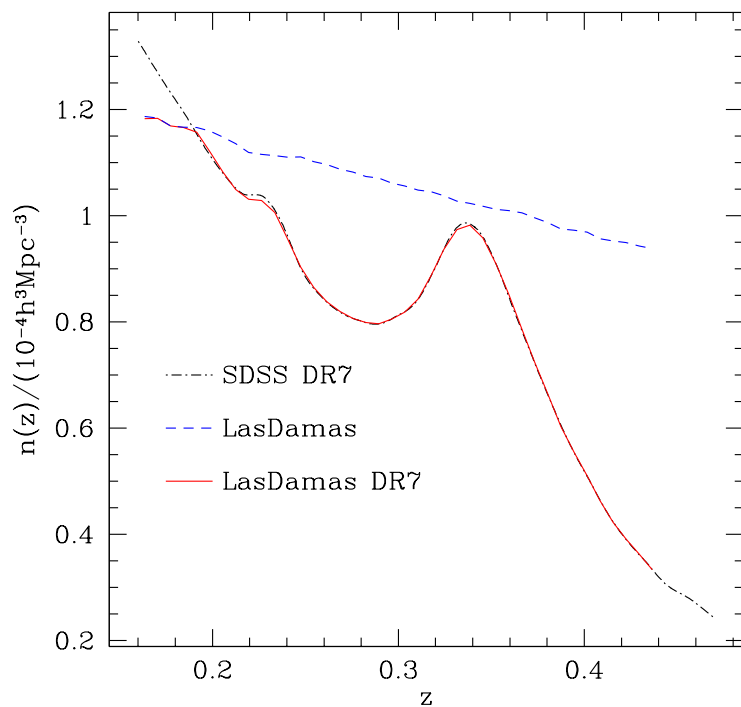


Figure 5.2: Spline fit to the redshift distribution of the LRGs (dot-dashed line) and the original and modified $n(z)$ of the mock catalogues (dashed and solid lines, respectively)

in the Northern Galactic Cap. The full survey also includes three equatorial stripes, that we do not consider. This causes a loss of less than 10% in galaxy number and volume, but the resulting geometry is simpler. Furthermore, the use of the Northern Galactic Cap only allows us to obtain an estimate of the statistical errors more accurate than for the full survey (see Section 5.1.2). Figures 5.1 and 5.2 show, respectively, the LRG angular footprint and, with the dot-dashed line, a smooth spline fit to the number density of the sample as function of redshift. Together with the LRGs catalogue, I use a random one with about fifty times more objects, designed to reproduce the geometry and completeness

matter density	Ω_m	0.25	Table 5.1: Cosmological parameters and specifications of the LasDamas-Oriana simulations
cosmological constant density	Ω_Λ	0.75	
baryonic density	Ω_b	0.04	
Hubble parameter [$\text{km s}^{-1} \text{Mpc}^{-1}$]	H	70	
amplitude of density fluctuations	σ_8	0.8	
scalar spectral index	n_s	1.0	
number of particles	N_p	1280^3	
box size [$h^{-1} \text{Mpc}$]	V	2400	
particle mass [$10^{10} M_\odot$]	M_p	45.73	
softening length [$h^{-1} \text{kpc}$]	ϵ	53	

of the galaxy sample and to have a radial number density proportional to the dot-dashed line in Figure 5.2.

5.1.2 The mock catalogues

In order to test the analysis technique and to estimate the errors associated to the LRG sample, I use the *LasDamas* mock catalogues (McBride et al., in prep.). The mocks have been constructed from a suite of 40 large dark matter N-body simulations, dubbed *Oriana*, that reproduce a part of a universe characterised by a geometrically flat Λ CDM cosmology. The cosmological parameters and specifications of the simulations are listed in Table 5.1. From each simulation a halo catalogue has been extracted using a Friend-of-Friend algorithm with linking length 0.2 times the mean inter-particle separation. In order to match the LRG clustering signal, the haloes have then been populated with mock galaxies using a halo occupation distribution (HOD, Berlind & Weinberg, 2002) within the halo model approach. The HOD parameters have been chosen in order to reproduce the galaxy number density and the projected correlation function of the observed SDSS DR7 samples. From each simulation two (four) mock catalogues of the full SDSS DR7 volume (Northern Galactic Cap only) have been extracted. These mock catalogues, together with the mocks from two smaller companions of Oriana and the corresponding random catalogues, are publicly available².

For this thesis I use the 160 mock catalogues of the LRGs in the Northern Galactic Cap region. I modify the mocks and the corresponding random catalogue, which have the radial number density shown by the dashed line in Figure 5.2, in order to reproduce the one of the LRG. The resulting $n(z)$ is indicated by the solid line. The mock catalogues contain on average 91137 galaxies.

²<http://lss.phy.vanderbilt.edu/lasdamas>

5.2 The power spectra

From the dataset and mock catalogues just described I compute the power spectra and the covariance matrix that will be used in the rest of the chapter. They are presented in this section.

5.2.1 The LRG power spectrum

To compute the power spectrum and the window function I need to convert the observed angular positions and redshifts of the galaxies and the random points into comoving coordinates. This is done first inferring radial distances from the measured redshifts and then converting the spherical coordinates into cartesian ones. To do the first step I assume as fiducial the cosmology of the LasDamas simulations, shown in Table 5.1.

I compute the power spectrum, as well as the survey window function, using the estimator introduced by Feldman et al. (1994, thereafter FKP). Percival et al. (2004, thereafter PVP) proposed a modification of the FKP approach to take into account the relative biases between populations with different luminosities. In Appendix B.1 I show that, thanks to the fact that the LRG sample is almost volume limited and composed of a relatively homogeneous class of galaxies, the shape of the power spectra recovered with the two methods are in excellent agreement at linear and mildly non-linear scales. In Appendix A.2 I summarise the most important equations of both estimators.

At first I correct the galaxy catalogue for the loss of objects due to fibre collisions (Zehavi et al., 2002; Masjedi et al., 2006). The SDSS spectrographs are fed by optical fibres plugged on plates, forcing the fibres to be separated by at least $55''$. It is then impossible, in a single exposure, to obtain spectra of galaxies nearer than this angular distance. The problem is partially alleviated by multiple exposures, but it is not possible to observe all the objects in crowded regions. Assuming that in a given region of the n galaxies that satisfy the selection criteria one can measure only $m \leq n$ redshifts due to fibre collisions and assuming that the missed galaxies have the same redshift distribution of the observed ones, I assign to the latter a weight $w_i = n/m$. This ensures that the sum of the weights in a given region of the sky is equal to the number of selected galaxies n . Secondly to each LRG and random object at position \mathbf{x} , where the number density is $n(\mathbf{x})$, I associate a weight $w(\mathbf{x}) = (1 + p_w n(\mathbf{x}))^{-1}$, with $p_w = 40000 h^{-3} \text{Mpc}^3$. This value has been chosen in order to minimise the variance of the measured power spectrum in the range $0.02 h \text{Mpc}^{-1} \leq k \leq 0.2 h \text{Mpc}^{-1}$. In Appendix B.1 I show the results of the tests of the impact of different choices of p_w and corrections, namely fibre collision and completeness, on the recovered power spectrum.

To compute the power spectrum I assign the LRGs and the random objects, weighted as described before, to a cubic grid with $N = 1024^3$ cells and side $L = 2200 h^{-1} \text{Mpc}$ using TSC as MAS. For each cell, I compute the $F(\mathbf{x})$ field of equation (A.5a). I then perform the fast Fourier transform using FFTW (Frigo & Johnson, 2005). As I have done in Section 4.1.2 with the L-BASICC simulations, I correct each Fourier mode as shown in the first line of equation (A.4b). Finally I spherically average the Fourier modes and subtract the

shot noise of equation (A.9a).

The window function is evaluated similarly. I assign the objects of the random catalogue to four cubic grids with $N = 1024^3$ cells and sides $L = 2200, 4400, 8800$ and $17600 h^{-1}$ Mpc and compute the field $G(\mathbf{x})$ of equation (A.10a). I use the four grids with different dimensions in order to be able to compute the window function up to very large scales. For each box, I perform the FFT, correct the Fourier modes, spherically average and subtract the shot noise (equation A.11a). For each window function $G^2(k)$, I discard all the modes with wave-number $k > 0.65 k_N$ and, when two or more window functions overlap, I consider only the one computed in the larger volume. This choice is motivated by the fact that, for a given band in wavenumber, the larger volume window function has been computed averaging over a larger number of modes than the ones from smaller volumes. Finally I merge the four window functions in order to obtain a single curve.

According to equation (A.8), the observed power spectrum $P_o(k)$ just described is a convolution of the “true” power spectrum $P_t(k)$ with the window function. This convolution is computationally time consuming, in particular when it has to be performed repetitively. Therefore I transform this convolution into a matrix multiplication:

$$P_o(k_i) = \sum_n W(k_i, k_j) P_t(k_j) - C G^2(k_i). \quad (5.1)$$

$W(k_i, k_j) = a_j k_j^2 \int_{-1}^1 d \cos(\theta) G^2(|\mathbf{k}_i - \mathbf{k}_j|)$ is the window matrix normalised such that $\sum_j W(k_i, k_j) = 1 \forall i$. The weights a_j corresponding to the wavenumber k_j are derived using the Gauss-Legendre decomposition. The second term in the right hand side arises from the *integral constraint* (Percival et al., 2007) and C is a constant determined by requiring that $P_o(0) = 0$.

The LRG power spectrum is shown in panel a) of Figure 5.3 with blue dots connected by a solid line. I also show the linear (green dashed line) and the model (red solid line) power spectra computed from the best fit parameters obtained assuming a flat Λ CDM cosmology (see section 5.4.1 for more details). Both power spectra have been convolved with the window function as in equation (5.1). The blue shaded area shows the variance from the mock catalogues. The panel b) shows the same quantities, with the same colour and line coding, but divided by a smooth linear power spectrum without BAOs (Eisenstein & Hu, 1998).

Panel c) in Figure 5.3 shows every third row of the window matrix $W(k_i, k_j)$. Because of the relatively simple and uniform geometry of the sample used, the window function has its maximum at $k = 0 h \text{ Mpc}^{-1}$ and decreases very steeply. This translates into very sharp peaks at $k_j \sim k_i$ in the window matrix rows, as shown in the figure.

5.2.2 The mock power spectra and covariance matrix

I compute the power spectra from the 160 realisations and the window function as described for the LRG sample in the previous section. I then compute the mean $\bar{P}(k)$, the standard deviation and the covariance matrix \mathbf{C} as in equation (4.9).

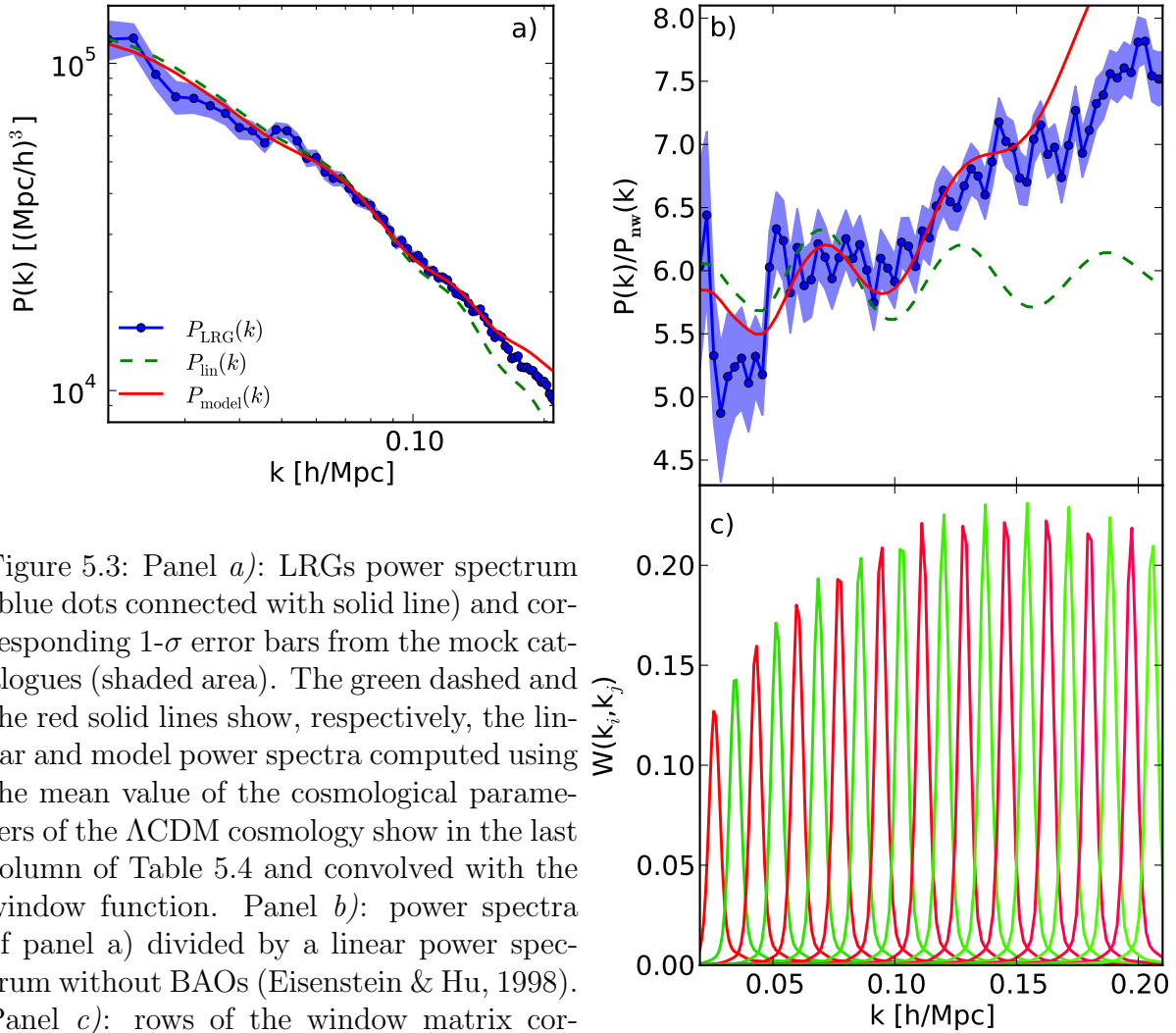


Figure 5.3: Panel *a*): LRGs power spectrum (blue dots connected with solid line) and corresponding $1\text{-}\sigma$ error bars from the mock catalogues (shaded area). The green dashed and the red solid lines show, respectively, the linear and model power spectra computed using the mean value of the cosmological parameters of the Λ CDM cosmology show in the last column of Table 5.4 and convolved with the window function. Panel *b*): power spectra of panel *a*) divided by a linear power spectrum without BAOs (Eisenstein & Hu, 1998). Panel *c*): rows of the window matrix corresponding to the k -bands of the measured LRG power spectrum. For clarity only every third row is shown.

Panel *a*) of Figure 5.4 shows the mean power spectrum and its variance (blue dots with solid line and shaded area) from of the mock catalogues. The green dashed and the red solid lines show the linear and the best fit model power spectra (see Section 5.3.3 for more details) convolved with the window function of the mocks. Panel *b*) of Figure 5.4 shows the same power spectra of panel *a*) divided by a power spectrum without oscillations $P_{\text{nw}}(k)$.

The correlation matrix of the mock catalogues, defined as $C_{ij}/\sqrt{C_{ii}C_{jj}}$, is shown in Figure 5.5. The mode correlation caused by the convolution with the window function is visible in particular near the diagonal. Non linear mode coupling is present at small scales and its strength increases with increasing k . Although the correlation becomes important for $k > 0.2 h \text{ Mpc}^{-1}$, it is non-negligible already at $k \approx 0.1 h \text{ Mpc}^{-1}$. Recently Samushia

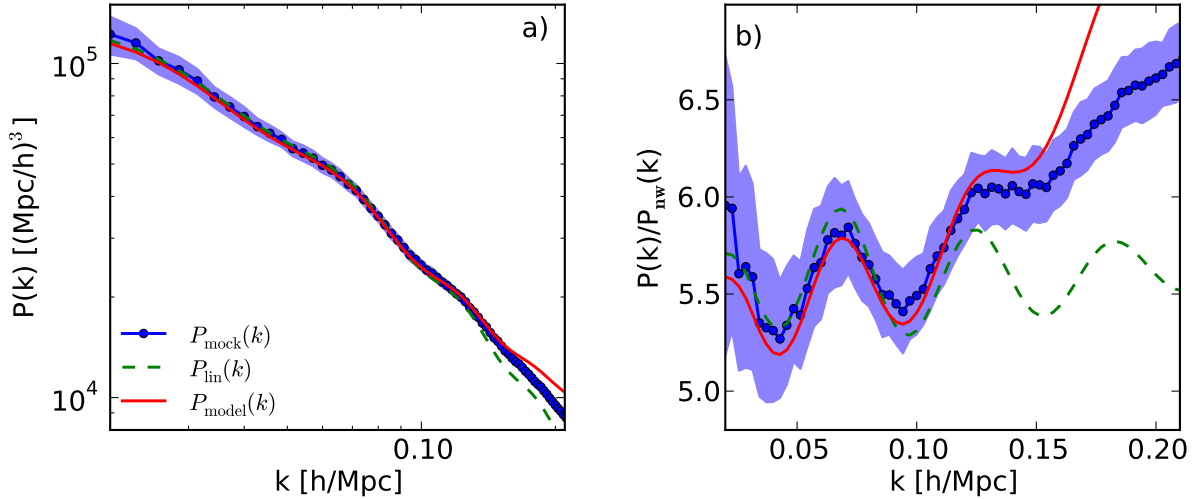


Figure 5.4: Panel *a*): mean power spectrum (blue dots connected by solid line) with $1\text{-}\sigma$ variance (blue shaded area) from the mock catalogues. The linear and model power spectra, convolved with the window function, are shown with green dashed and red solid line, respectively. Panel *b*): same power spectra divided by a linear power spectrum without BAOs (Eisenstein & Hu, 1998)

et al. (2011) showed that different methods to construct the random catalogues can affect the estimated covariance matrix.

The version of the mocks available when writing this thesis does not contain information about the luminosity of the galaxies, completeness or fibre collisions. I cannot therefore test the impact of different estimators and corrections on the errors. However I test the impact of different p_w on the power spectra and errors as measured from the mocks: the results are reported in Appendix B.2.

5.3 Methodology

In Sections 5.3.1 and 5.3.2, I present the parameter spaces used in Section 5.4 and the method used to extract cosmological information. I test the model against the LasDamas and the LRG power spectra (Section 5.3.3).

5.3.1 Parameter spaces

Within the framework outlined in Chapter 2 I analyse five different cosmological models, explored using five different combinations of the LRG power spectrum and the experiments described in Section 3.2. The combinations are: CMB, CMB+ $P_{\text{LRG}}(k)$, CMB+ $P_{\text{LRG}}(k)+H_0$, CMB+ $P_{\text{LRG}}(k)+\text{SNIa}$ and CMB+ $P_{\text{LRG}}(k)+H_0+\text{SNIa}$.

The ‘‘concordance’’ Λ CDM model is the simplest model able to successfully describe a

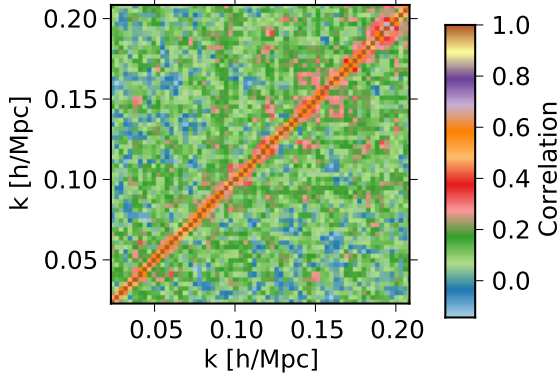


Figure 5.5: Correlation matrix as computed from the mock catalogues.

large variety of cosmological datasets. It describes a geometrically flat ($\Omega_k = 0$) universe with a cosmological constant Λ , whose equation of state parameter $w_{\text{DE}} = -1$ is constant in space and time, and pressureless cold dark matter (CDM) as main components. This cosmology can be characterised by six parameters: the baryon and dark matter density $\omega_b = \Omega_b h^2$, $\omega_{\text{DM}} = \Omega_{\text{DM}} h^2$, the scalar spectral index n_s and the amplitude A_s of the primordial fluctuations, the optical depth τ , assuming instantaneous reionisation, and the ratio between the horizon scale at decoupling and the angular diameter distance to the corresponding redshift Θ :

$$\theta_{\Lambda\text{CDM}} = (\omega_b, \omega_{\text{DM}}, n_s, A_s, \tau, \Theta; b, k_*, A_{\text{MC}}, A_{\text{SZ}}). \quad (5.2)$$

The four parameters after the semicolon are related to the modelling of the matter power spectrum (b , k_* and A_{MC} from equation 4.4) and of the CMB angular power spectrum (A_{SZ} , the amplitude of the contribution to the CMB at large l from the Sunyaev-Zeldovich effect). These parameters will be marginalised over when showing the cosmological constraints in the section 5.4.

If I then drop one or both assumptions about the geometry and the value of w_{DE} , I obtain three cosmologies characterised by the following parameter spaces:

- variable curvature, $w_{\text{DE}} = -1$:

$$\theta_{k\Lambda\text{CDM}} = (\omega_b, \omega_{\text{DM}}, \Omega_k, n_s, A_s, \tau, \Theta; b, k_*, A_{\text{MC}}, A_{\text{SZ}}); \quad (5.3)$$

- zero curvature, $w_{\text{DE}} = \text{const}$:

$$\theta_{w\text{CDM}} = (\omega_b, \omega_{\text{DM}}, w_{\text{DE}}, n_s, A_s, \tau, \Theta; b, k_*, A_{\text{MC}}, A_{\text{SZ}}); \quad (5.4)$$

- variable curvature, $w_{\text{DE}} = \text{const}$:

$$\theta_{kw\text{CDM}} = (\omega_b, \omega_{\text{DM}}, \Omega_k, w_{\text{DE}}, n_s, A_s, \tau, \Theta; b, k_*, A_{\text{MC}}, A_{\text{SZ}}). \quad (5.5)$$

Parameter	lower limit	upper limit
$\omega_b = \Omega_b h^2$	0.005	0.1
$\omega_{\text{DM}} = \Omega_{\text{DM}} h^2$	0.01	0.99
Ω_k	-0.3	0.3
$w_{\text{DE}} (w_0)$	-2	0
w_a	-2	2
n_s	0.5	1.5
$\log(10^{10} A_s)$	2.7	4
τ	0.01	0.8
100Θ	0.5	10
k_\star	0.01	0.35
A_{MC}	0	5
A_{SZ}	0	2

Table 5.2: Prior ranges for the fundamental cosmological and the model parameters

As last case, I consider a flat Universe in which $w_{\text{DE}}(a)$ evolves with time. I adopt the parametrisation proposed by Linder (2003):

$$w_{\text{DE}}(a) = w_0 + w_a(1 - a). \quad (5.6)$$

Although not physically motivated, it can describe accurately a big variety of equations of state derived from scalar fields with the use of only two parameters: its value today, w_0 , and its first derivative with respect to a , w_a . The resulting parameter space is:

$$\theta_{\text{waCDM}} = (\omega_b, \omega_{\text{DM}}, w_0, w_a, n_s, A_s, \tau, \Theta; b, k_\star, A_{\text{MC}}, A_{\text{SZ}}). \quad (5.7)$$

Other cosmological quantities can be derived from the ones just listed. In particular I am interested in:

$$\theta_{\text{der}} = (\Omega_{\text{DE}}, \Omega_{\text{M}}, H, t_0, \sigma_8, z_{\text{re}}). \quad (5.8)$$

The density of dark energy, Ω_{DE} , is obtained from a combination of Ω_k , $\omega_{\text{M}} = \omega_b + \omega_{\text{DM}}$ and Θ . From there, the total matter density $\Omega_{\text{M}} = 1 - \Omega_k - \Omega_{\text{DE}}$, the Hubble parameter $h = \sqrt{\omega_{\text{M}}/\Omega_{\text{M}}}$ and the age of the universe $t_0 = \int_0^1 da / [aH(a)]$ are derived. The present day *rms* of linear density fluctuation in a sphere of radius $8 h^{-1}$ Mpc, σ_8 , is computed from A_s . From τ , H , Ω_b and Ω_{DM} it is possible to estimate the redshift of reionisation z_{re} (Tegmark et al., 1994).

5.3.2 Practical issues

To constrain the sets of cosmological and model parameters just described, I use the Markov Chain Monte Carlo technique as implemented in the free software COSMOMC³ (Cosmological MonteCarlo, Lewis & Bridle, 2002). The CMB and linear matter power spectra are

³<http://cosmologist.info/cosmomc/>

computed with a modified version of CAMB (Code for Anisotropies in the Microwave Background, Lewis et al., 2000) that allows to consider time varying w_{DE} ⁴(Fang et al., 2008). For each choice of parameter space and probes I run eight independent chains. Their execution is stopped when the Gelman & Rubin (1992) criterion $R < 1.02$ is satisfied. The MCMC requires some prior knowledge of the parameter space that is explored. I assume for all the primary parameters (equations 5.2-5.5 and 5.7) flat priors in the ranges listed in Table 5.2. The model parameter b is analytically marginalised over an infinite flat prior as in the previous chapter.

All likelihoods used to compare the results from the cosmological probes described in sections 5.1.1, 3.2.1, 3.2.2 and 3.2.3 with the corresponding models are assumed to be Gaussian. In the case of the LRGs power spectrum I use the likelihood function of equation (4.7).

In section 5.1.1 I assumed a fiducial cosmology in order to convert redshifts and angles to physical coordinates. Different choices of the parameters result in modifications of the measured LRG power spectrum. The ideal case would be to recompute, for each step of the MCMC chain, the power spectrum and the window function according to the given cosmology, but this is not computationally feasible. It is possible to incorporate these distortions in the power spectrum thanks to the factor α of equation (4.5). Thus at each step of the chain I multiply the wave-number of the model power by $1/\alpha$ and its amplitude by α^3 in order to rescale it to the fiducial cosmology.

5.3.3 Testing the model

In this section I fit the model of equation (4.4) against the mock catalogues in order to test whether it provides an accurate description of the measured power spectrum and unbiased constraints on the dark energy equation of state parameter also when a complex geometry is involved. I also test the stability of the cosmological parameters of in the $w\text{CDM}$ case as the maximum k included in the analysis varies, when CMB and the $P_{\text{LRG}}(k)$ are combined.

Mock catalogues

In this section I follow the method described in Section 4.3.1 and assume all the parameters fixed, except for w_{DE} . Under this assumption, equation (4.5) links univocally variations of the dark energy equation of state parameter to stretches α of the model power spectrum. Therefore I consider the latter as a free parameter.

Using a MCMC approach, I explore the parameter space defined by $\theta = (k_*, b, A_{\text{MC}}, \alpha)$. I chose priors with a constant probability within the following ranges:

- $0 h \text{ Mpc}^{-1} < k_* < 0.35 h \text{ Mpc}^{-1}$,
- $0 \leq A_{\text{MC}} < 10$,
- $0.5 \leq \alpha < 1.5$.

⁴<http://camb.info/ppf/>

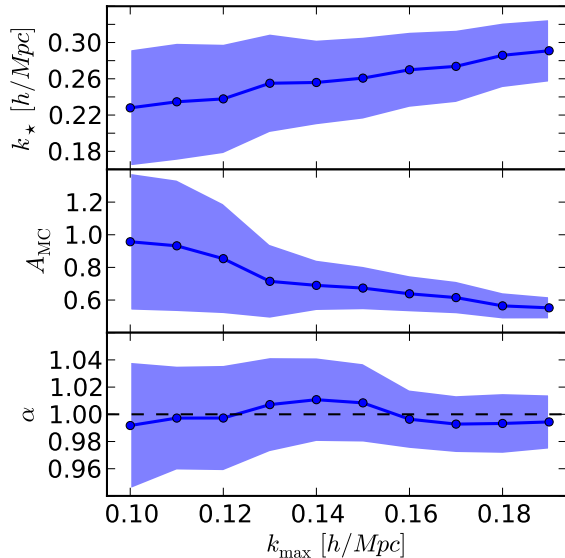


Figure 5.6: Marginalised constraints on the parameters k_* , A_{MC} and α as function of the maximum value of k (k_{max}) used to fit the model of equation (4.4) to the LasDamas mean power spectrum. The mean values and the standard deviation are indicated, respectively, by circles connected with solid lines and shaded areas. Before the convolution with the window function the model is computed for $k \leq 0.2 h \text{ Mpc}^{-1}$.

The bias b is marginalised analytically over an infinite flat prior.

Figure 5.6 shows, from top to bottom, the one-dimensional marginalised constraints on the parameters k_* , A_{MC} and α when varying the maximum value of the wave number k_{max} of the measured power spectrum used to perform the fit; we keep the minimum k fixed to $0.02 h \text{ Mpc}^{-1}$. The blue circles connected by solid lines and the shaded areas correspond to the mean and the standard deviation of these parameters. For every k_{max} the model is evaluated for $k \leq 0.2 h \text{ Mpc}^{-1}$ and then convolved with the window function. Since each row of $W(k_i, k_j)$ is sharply peaked at $k_j \sim k_i$, the main contribution to $P_o(k_i)$ comes from modes near k_i ; therefore the constraints shown in Figure 5.6 depend weakly on the exact wave number range in which the model is computed, as long as it is larger than the range of the measured power spectrum that I fit. As k_{max} increases, more modes are included in the fit and the errors decrease. The value of α that I obtain are compatible with unity for all the k_{max} considered. In Section 4.3 I show that, in the redshift range of the LRGs catalogue, the model is accurate for $k \lesssim 0.15 h \text{ Mpc}^{-1}$. Considering that the volume of the L-BASICC II simulations is much larger than the one sampled by the LRGs and consequently that the errors in the former case are smaller than in the latter, I decide to further consider scales $0.02 h \text{ Mpc}^{-1} \leq k \leq 0.15 h \text{ Mpc}^{-1}$. The constraints on k_* and A_{MC} exhibit, respectively, a monotonic increase and decrease as function of k_{max} . As explained Section 4.3, the approximate mode coupling power in equation (4.4) is about 30% larger than the exact value at $k \approx 0.15 - 0.2 h \text{ Mpc}^{-1}$: this forces A_{MC} to decrease to $\sim 0.7 - 0.6$ and k_* to increase in order to maintain the shape of the resulting power spectrum unvaried.

Figure 5.7 shows the two-dimensional marginalised constraints in the $k_* - \alpha$ plane as obtained from the mock catalogues for $k_{\text{max}} = 0.15 h \text{ Mpc}^{-1}$. The inner dark and outer light shaded areas represent regions whose volumes are 68% and 95% of the total likelihood. This representation of the two-dimensional constraints will be used through all section 5.4. The independence of α from k_* or A_{MC} makes the constraints on the former robust. The latter

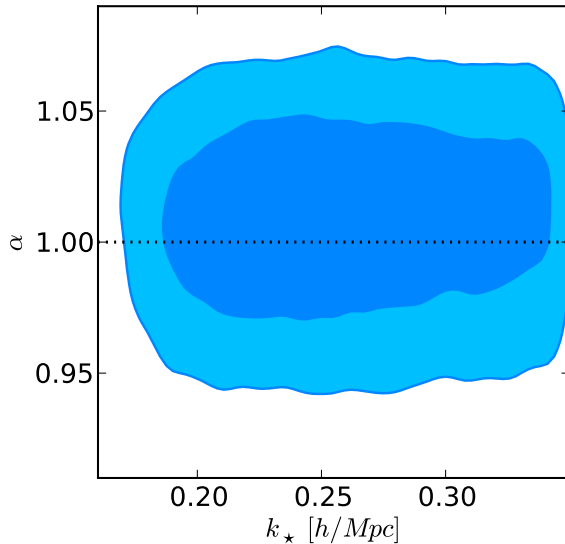


Figure 5.7: Two-dimensional marginalised constraints in the $k_* - \alpha$ plane obtained applying the model of equation (4.4) to the LasDamas mean power spectrum. The results are shown for $k_{\max} = 0.15 h \text{ Mpc}^{-1}$. The inner dark and outer light areas represent the 68% and 95% confidence level, respectively.

two parameters, instead, are strongly degenerate, as it is possible to describe accurately the overall shape of the power spectrum compensating an increase (decrease) of k_* with a decrease (increase) of A_{MC} .

The model power spectrum indicated by a solid line in both panels of Figures 5.4 has been computed using the mean values of the parameters as obtained in this section using $k_{\max} = 0.15 h \text{ Mpc}^{-1}$: $k_* = 0.26 h \text{ Mpc}^{-1}$, $A_{\text{MC}} = 0.67$. The bias has been computed maximising the likelihood of equation (4.7) with all the other parameters fixed.

The luminous red galaxy sample

After testing the robustness of our model at mildly non-linear scales, I test here the dependence of the cosmological parameters upon k_{\max} . I use the Λ CDM cosmology defined in equation (5.4) and the combination of the LRG power spectrum and CMB measurements. Figure 5.8 shows the one-dimensional marginalised constraints on the parameters ω_b , ω_{DM} , w_{DE} , Ω_{DE} , σ_8 and h as function of k_{\max} . The circles connected by solid lines and the shaded areas show the mean and the standard deviation as obtained from the MCMC. The model is computed for $k < 0.2 h \text{ Mpc}^{-1}$ and then convolved with the window function; as before, the measured parameters are insensitive to its exact value. Although some parameters are more stable with respect to changes of k_{\max} than others, there are no significant trends or deviations.

I also test the impact of using CMB measurements from WMAP only. In this case I obtain the same constraints, but with errors larger by 5-10%, due to the loss of information at small angular scales, i.e. large multipoles l . Appendix B.3 describes how the results just described depend upon p_w and w_i .

A more extensive analysis of the Λ CDM cosmology is presented in section 5.4.3.

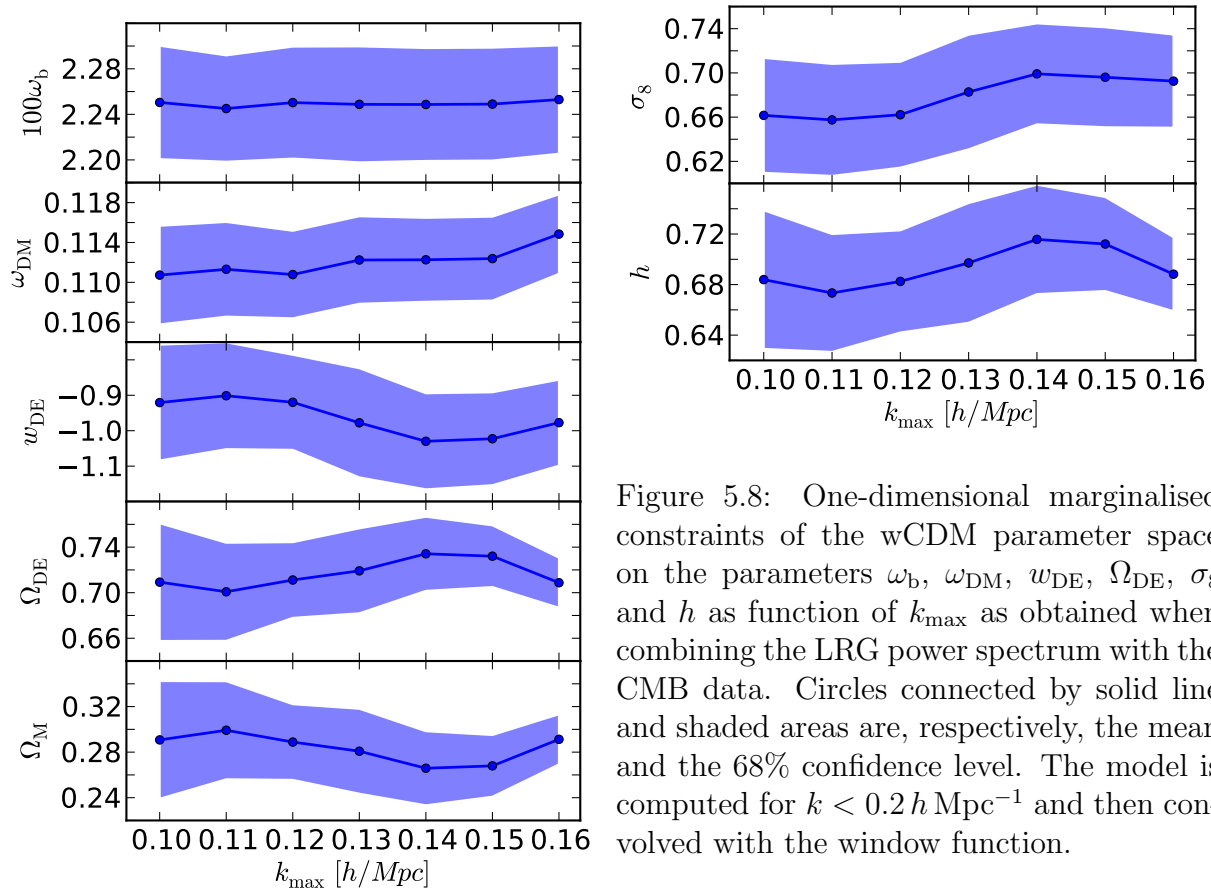


Figure 5.8: One-dimensional marginalised constraints of the w CDM parameter space on the parameters ω_b , ω_{DM} , w_{DE} , Ω_{DE} , σ_8 and h as function of k_{\max} as obtained when combining the LRG power spectrum with the CMB data. Circles connected by solid line and shaded areas are, respectively, the mean and the 68% confidence level. The model is computed for $k < 0.2 h \text{ Mpc}^{-1}$ and then convolved with the window function.

5.4 Results: the cosmological parameters

In this section I present the constraints on the cosmological parameters obtained from the five cosmological scenarios presented in section 5.3.1.

5.4.1 The concordance cosmology

The flat Λ CDM cosmology, parametrized by the first six quantities of equation (5.2), is the minimal model able to describe data coming from a variety of independent probes. Table 5.3 summarises the complete list of one-dimensional constraints for the primary and derived cosmological parameters obtained in this section. I quote the mean values and width of the posterior distribution containing 68% of the total area⁵ as obtained for the five different combinations of the four experiments used in this work. This convention will be followed in the rest of this chapter.

The CMB experiments described in section 3.2.3 provide measurements of the temperature and polarization angular power spectra with very high accuracy. The blue shaded

⁵For a Gaussian distribution this corresponds to the standard deviation.

Table 5.3: Marginalised constraints on the cosmological parameters of the Λ CDM parameter space from the combination of probes listed in the header of the table. The quoted values are the mean and widths of the posterior distribution containing 68% of the total area.

	CMB	CMB+ $P(k)$	CMB+ $P(k)$ + H_0	CMB+ $P(k)$ +SNIa	CMB+ $P(k)$ + H_0 +SNIa
$100\omega_b$	$2.254^{+0.052}_{-0.052}$	$2.258^{+0.048}_{-0.048}$	$2.259^{+0.050}_{-0.049}$	$2.252^{+0.047}_{-0.047}$	$2.260^{+0.047}_{-0.047}$
$100\omega_{\text{DM}}$	$10.96^{+0.52}_{-0.52}$	$11.23^{+0.36}_{-0.36}$	$11.10^{+0.35}_{-0.35}$	$11.22^{+0.34}_{-0.33}$	$11.13^{+0.33}_{-0.32}$
100Θ	$1.0400^{+0.0023}_{-0.0022}$	$1.0404^{+0.0020}_{-0.0020}$	$1.0406^{+0.0020}_{-0.0021}$	$1.0403^{+0.0021}_{-0.0020}$	$1.0406^{+0.0020}_{-0.0020}$
τ	$0.088^{+0.015}_{-0.015}$	$0.087^{+0.014}_{-0.014}$	$0.086^{+0.014}_{-0.014}$	$0.085^{+0.014}_{-0.015}$	$0.087^{+0.014}_{-0.014}$
n_s	$0.963^{+0.013}_{-0.013}$	$0.963^{+0.011}_{-0.012}$	$0.963^{+0.011}_{-0.011}$	$0.961^{+0.012}_{-0.011}$	$0.963^{+0.011}_{-0.011}$
$\log(10^{10} A_s)$	$3.065^{+0.033}_{-0.033}$	$3.075^{+0.031}_{-0.031}$	$3.068^{+0.033}_{-0.033}$	$3.070^{+0.032}_{-0.032}$	$3.071^{+0.032}_{-0.032}$
Ω_{DE}	$0.741^{+0.026}_{-0.026}$	$0.730^{+0.018}_{-0.018}$	$0.737^{+0.017}_{-0.017}$	$0.730^{+0.017}_{-0.017}$	$0.735^{+0.015}_{-0.016}$
Age [Gyr]	$13. - 0.112^{+0.111}$	$13.723^{+0.094}_{-0.094}$	$13.711^{+0.095}_{-0.093}$	$13.735^{+0.094}_{-0.092}$	$13.710^{+0.091}_{-0.094}$
Ω_{M}	$0.259^{+0.026}_{-0.026}$	$0.270^{+0.018}_{-0.018}$	$0.263^{+0.017}_{-0.017}$	$0.270^{+0.017}_{-0.017}$	$0.265^{+0.016}_{-0.015}$
σ_8	$0.796^{+0.027}_{-0.027}$	$0.807^{+0.022}_{-0.022}$	$0.799^{+0.022}_{-0.022}$	$0.804^{+0.021}_{-0.021}$	$0.802^{+0.021}_{-0.021}$
z_{re}	$10.4^{+1.2}_{-1.2}$	$10.4^{+1.1}_{-1.2}$	$10.3^{+1.2}_{-1.2}$	$10.3^{+1.2}_{-1.2}$	$10.4^{+1.2}_{-1.2}$
H_0 [km s $^{-1}$ Mpc $^{-1}$]	$71.7^{+2.4}_{-2.3}$	$70.8^{+1.6}_{-1.6}$	$71.3^{+1.5}_{-1.5}$	$70.7^{+1.5}_{-1.5}$	$71.2^{+1.4}_{-1.4}$

areas enclosed within dashed lines in panel a) of Figure 5.9 show the 68% and 95% confidence level in the $\Omega_{\text{DM}} - H_0$ as obtained when CMB information only is used. The apparent position of the peaks in the CMB power spectra is proportional to their physical scale, which depends on the composition of the early universe (baryons, dark matter and radiation), and the comoving angular diameter distance to the last scattering surface, a function of H_0 and of the density and equation of state parameters of matter, dark energy and curvature. Since here I consider a flat geometry and fix w_{DE} to -1, a degeneracy between the matter density and the Hubble parameter appears. It has been shown by Percival et al. (2002) that this effect, together with the preservation of the relative amplitude of the peaks, leads, in a Λ CDM universe, to a degeneracy along the curve defined by $\Omega_{\text{M}}h^3 \simeq \text{const}$, which is highlighted in Figure 5.9, panel a), by the dotted line. The accurate detection of the third peak in the temperature power spectrum, whose relative amplitude with respect to the first two is proportional to the matter-radiation ratio, helps reducing this degeneracy. I obtain $\Omega_{\text{M}} = 0.259 \pm 0.026$, $H_0 = 71.7^{+2.4}_{-2.3}$ km s $^{-1}$ Mpc $^{-1}$ and $\omega_{\text{DM}} = (10.96 \pm 0.52) \times 10^{-2}$.

The inclusion of information from the large scale structure can break or reduce some of the degeneracies in the CMB. The shape of the power spectrum depends upon $\Omega_{\text{M}}h$ and, more weakly, $\Omega_{\text{b}}/\Omega_{\text{M}}$ (e.g., Efstathiou et al., 2002; Sánchez & Cole, 2008). Thanks to this,

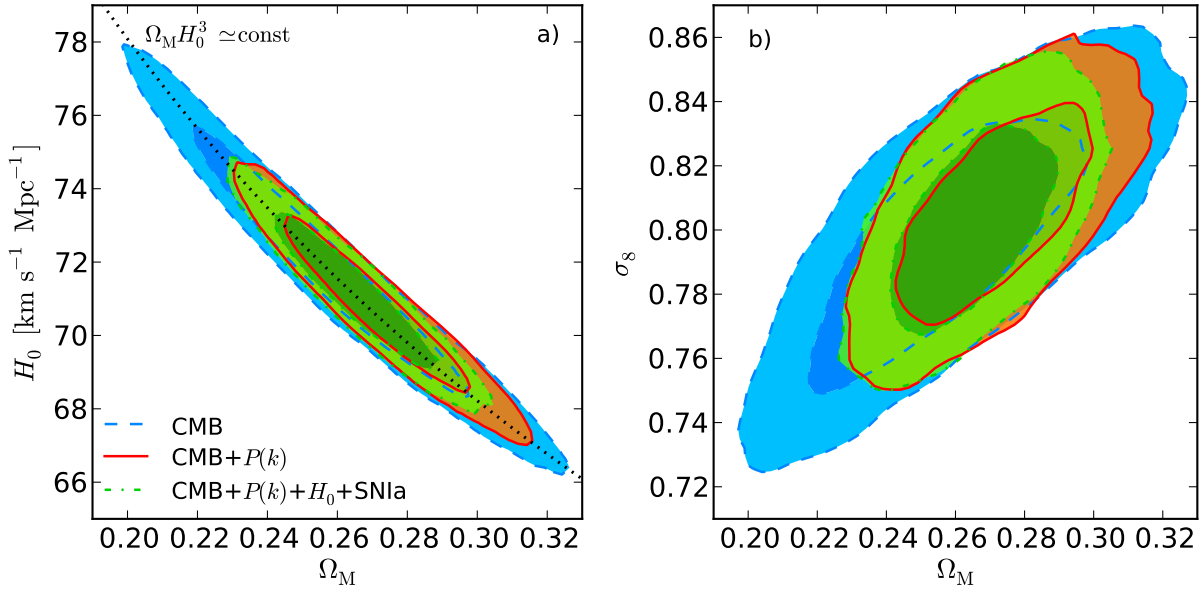


Figure 5.9: Panel *a*): two-dimensional marginalised constraints of the Λ CDM parameter space in the $\Omega_M - H_0$ plane. Blue, red and green shaded areas enclosed in dashed, solid and dot-dashed lines show the constraints from CMB alone, CMB+ $P_{\text{LRG}}(k)$ and CMB+ $P_{\text{LRG}}(k)$ + H_0 +SNIa, respectively. The inner darker and the outer lighter areas correspond to the 68% and 95% confidence level. The black dotted line that runs across the figure shows the locus defined by equation $\Omega_M H_0^3 \simeq \text{const}$. Panel *b*): two-dimensional marginalised constraints in the $\Omega_M - \sigma_8$ plane, for the same combinations of experiments.

the errors on the cosmological parameters decrease up to about 30%. In particular, I measure a decrease in the allowed region by about one third in the three parameters considered before: $\Omega_M = 0.27 \pm 0.018$, $H_0 = 70.8 \pm 1.60 \text{ km s}^{-1} \text{ Mpc}^{-1}$ and $\omega_{\text{DM}} = (11.23 \pm 0.36) \times 10^{-2}$. The two-dimensional constraints in the $\Omega_M - H_0$ plane are shown in panel a) of Figure 5.9 with the red shaded areas within solid lines.

When the SNIa and H_0 measurements are also used, I obtain $\Omega_M = 0.265 \pm 0.015$, $H_0 = 71.2 \pm 1.4 \text{ km s}^{-1} \text{ Mpc}^{-1}$ and $\omega_{\text{DM}} = (11.13_{-0.32}^{+0.33}) \times 10^{-2}$, which means a 10-15% increase in accuracy. The two-dimensional 68% and 95% confidence levels for the former two parameters, when all the four probes are used, are shown in panel a) of Figure 5.9 by the green shaded areas enclosed inside the dot-dashed lines.

Panel b) of Figure 5.9 shows the two-dimensional marginalised constraints in the $\Omega_M - \sigma_8$ plane for the same combination of datasets with the same colours and line styles as panel a). The correlation between the two parameters is caused by the fact that an increase (decrease) of Ω_M causes a decrease (increase) in the amplitude of the power spectrum that can be compensated by a larger (smaller) value of σ_8 . For the three cases shown in the figure I find that the one-dimensional constraints on the latter parameter are, respectively, $\sigma_8 = 0.796 \pm 0.027$, $\sigma_8 = 0.807 \pm 0.022$ and $\sigma_8 = 0.802 \pm 0.021$; the error on the latter two decreases by 20 and 22% respectively to the CMB alone result.

	no systematics	MLCS2K2
$100\omega_b$	$2.258^{+0.046}_{-0.048}$	$2.244^{+0.047}_{-0.046}$
$100\omega_{\text{DM}}$	$11.16^{+0.28}_{-0.29}$	$11.61^{+0.31}_{-0.31}$
100Θ	$1.0405^{+0.0020}_{-0.0020}$	$1.0402^{+0.0021}_{-0.0020}$
τ	$0.087^{+0.014}_{-0.014}$	$0.084^{+0.014}_{-0.014}$
n_s	$0.963^{+0.011}_{-0.011}$	$0.957^{+0.011}_{-0.011}$
$\log(10^{10} A_s)$	$3.072^{+0.033}_{-0.033}$	$3.081^{+0.031}_{-0.032}$
Ω_{DE}	$0.734^{+0.013}_{-0.013}$	$0.709^{+0.016}_{-0.016}$
Age [Gyr]	$13. - 0.089^{+0.089}$	$13.765^{+0.090}_{-0.090}$
Ω_{M}	$0.266^{+0.013}_{-0.013}$	$0.291^{+0.016}_{-0.016}$
σ_8	$0.803^{+0.020}_{-0.020}$	$0.822^{+0.021}_{-0.021}$
z_{re}	$10.4^{+1.2}_{-1.2}$	$10.3^{+1.2}_{-1.2}$
H_0 [$\text{km s}^{-1} \text{Mpc}^{-1}$]	$71.0^{+1.2}_{-1.2}$	$69.1^{+1.3}_{-1.3}$

Table 5.4: Marginalised constraints on the cosmological parameters of the Λ CDM parameter space from the combination of CMB+ $P_{\text{LRG}}(k)$ + H_0 +SNIa when systematic errors are not considered and when the MLCS2K2 SNIa light curve fitter is used.

The solid lines in panels a) and b) of Figure 5.3 show the model power spectrum computed using the cosmological parameters listed in the last column of Table 5.3 and the model parameters $k_* = 0.29 h \text{Mpc}^{-1}$ and $A_{\text{MC}} = 0.77$, as obtained from the MCMC for $k_{\text{max}} = 0.15 h \text{Mpc}^{-1}$. The bias has been computed maximising the likelihood of equation (4.7) with all the other parameters fixed.

Effects of supernovae systematics and light curve fitters

Uncertainties in the modelling of SNIa can affect the cosmological parameters and associated errors extracted using a given dataset. To test the impact of systematics and light curve fitters on the results just presented, I re-analyse the Λ CDM cosmology with two different SNIa settings. First I use the same Union2 set, but neglecting the systematic errors provided with the data; then I substitute this dataset with the SDSS SN sample analysed with MLCS2K2; both datasets are described in Section 3.2.1. The one-dimensional constraints that I extract from the combination of all four probes using these supernovae data are listed in Table 5.4. As expected, and in agreement with Amanullah et al. (2010), ignoring systematic errors globally reduces the errors on the recovered values of the parameters without changing sensibly the mean value. For example I obtain $\Omega_{\text{M}} = 0.266 \pm 0.013$ (14% decrease with respect to the corresponding case in Table 5.3), $H_0 = 71.0^{+1.2}_{-1.2} \text{km s}^{-1} \text{Mpc}^{-1}$ (12%), $\omega_{\text{DM}} = (11.16^{+0.28}_{-0.29}) \times 10^{-2}$ (14%) and $\sigma_8 = 0.803 \pm 0.020$ (5%). On the other hand, the use of MLCS2K2 changes the posterior distribution sensibly, without influencing its width. We measure that Ω_{M} , ω_{DM} and H_0 change by more than $1.5\text{-}2\sigma$. This shift agrees with the findings in Kessler et al. (2009) and suggests that the choice of the model used to fit the light curves can bias sensibly the cosmological results obtained.

Table 5.5: Marginalised constraints on the cosmological parameters of the Λ CDM parameter space from the combination of probes listed in the header of the table. The quoted values are as in Table 5.3.

	CMB	CMB+ $P(k)$	CMB+ $P(k)$ + H_0	CMB+ $P(k)$ +SNIa	CMB+ $P(k)$ + H_0 +SNIa
$100\omega_b$	$2.232^{+0.052}_{-0.050}$	$2.250^{+0.048}_{-0.047}$	$2.252^{+0.050}_{-0.049}$	$2.245^{+0.050}_{-0.048}$	$2.247^{+0.049}_{-0.050}$
$100\omega_{\text{DM}}$	$11.06^{+0.50}_{-0.50}$	$11.29^{+0.44}_{-0.45}$	$11.30^{+0.45}_{-0.45}$	$11.30^{+0.42}_{-0.41}$	$11.31^{+0.43}_{-0.44}$
100Θ	$1.0396^{+0.0022}_{-0.0022}$	$1.0401^{+0.0022}_{-0.0021}$	$1.0402^{+0.0022}_{-0.0022}$	$1.0400^{+0.0021}_{-0.0021}$	$1.0400^{+0.0022}_{-0.0021}$
τ	$0.086^{+0.014}_{-0.015}$	$0.085^{+0.014}_{-0.014}$	$0.085^{+0.014}_{-0.014}$	$0.085^{+0.014}_{-0.014}$	$0.085^{+0.015}_{-0.014}$
$100\Omega_k$	$-4.90^{+4.39}_{-5.10}$	$0.16^{+0.54}_{-0.54}$	$0.30^{+0.49}_{-0.49}$	$0.14^{+0.51}_{-0.53}$	$0.30^{+0.48}_{-0.47}$
n_s	$0.956^{+0.013}_{-0.013}$	$0.961^{+0.012}_{-0.012}$	$0.961^{+0.012}_{-0.012}$	$0.960^{+0.012}_{-0.012}$	$0.960^{+0.012}_{-0.012}$
$\log(10^{10} A_s)$	$3.062^{+0.033}_{-0.033}$	$3.072^{+0.030}_{-0.031}$	$3.073^{+0.032}_{-0.032}$	$3.072^{+0.032}_{-0.032}$	$3.073^{+0.033}_{-0.033}$
Ω_{DE}	$0.597^{+0.132}_{-0.149}$	$0.731^{+0.019}_{-0.019}$	$0.736^{+0.016}_{-0.016}$	$0.730^{+0.016}_{-0.016}$	$0.734^{+0.015}_{-0.015}$
Age [Gyr]	$15 - 1.37^{+1.46}$	$13.65^{+0.27}_{-0.27}$	$13.58^{+0.23}_{-0.24}$	$13.67^{+0.26}_{-0.26}$	$13.59^{+0.24}_{-0.24}$
Ω_M	$0.452^{+0.200}_{-0.175}$	$0.267^{+0.020}_{-0.021}$	$0.261^{+0.017}_{-0.017}$	$0.269^{+0.018}_{-0.017}$	$0.263^{+0.016}_{-0.015}$
σ_8	$0.773^{+0.032}_{-0.032}$	$0.808^{+0.024}_{-0.025}$	$0.809^{+0.026}_{-0.026}$	$0.808^{+0.025}_{-0.025}$	$0.810^{+0.025}_{-0.026}$
z_{re}	$10.3^{+1.2}_{-1.2}$	$10.3^{+1.2}_{-1.1}$	$10.3^{+1.2}_{-1.2}$	$10.3^{+1.2}_{-1.1}$	$10.4^{+1.2}_{-1.2}$
H_0 [km s $^{-1}$ Mpc $^{-1}$]	$57.3^{+11.5}_{-12.0}$	$71.3^{+2.5}_{-2.4}$	$72.1^{+2.1}_{-2.0}$	$71.1^{+2.2}_{-2.2}$	$71.9^{+1.9}_{-2.0}$

5.4.2 Curvature

In this section I analyse the cosmological constraints obtained when the curvature of space is considered as a free parameter. The full list of parameters (mean plus the 68% confidence level) is shown in Table 5.5 for the combination of experiments listed in the header of the table.

The blue shaded areas within dashed lines in panel a) of Figure 5.10 and in Figure 5.11 show the two-dimensional marginalised constraints in the $\Omega_{\text{DE}} - \Omega_M$ and $\Omega_{\text{DE}} - H_0$ planes, respectively, as obtained from CMB data alone. The plots show a very strong degeneracy between these parameters. As stated in Section 5.4.1, the apparent size of the CMB acoustic peaks depends on their physical size and the angular diameter distance. Given that the density of curvature, Ω_k , is small and that it scales as the inverse square of the scale factor, it affects much more D_A than the dynamics of the early universe. Thus it is always possible to find combinations of Ω_k , ω_m and ω_b that keep fixed the location of the CMB peaks. Therefore, the constraints on the derived parameters are much weaker than the ones obtained in the previous section: $\Omega_{\text{DE}} = 0.6^{+0.13}_{-0.15}$, $\Omega_M = 0.45^{+0.20}_{-0.17}$ and $H_0 = 57 \pm 12$ km s $^{-1}$ Mpc $^{-1}$. The measured curvature, $\Omega_k = (-4.9^{+4.4}_{-5.1}) \times 10^{-2}$, is compatible with flatness at about the 1σ level.

Both panels of Figure 5.10 and Figure 5.11 show, with red shaded areas enclosed in solid

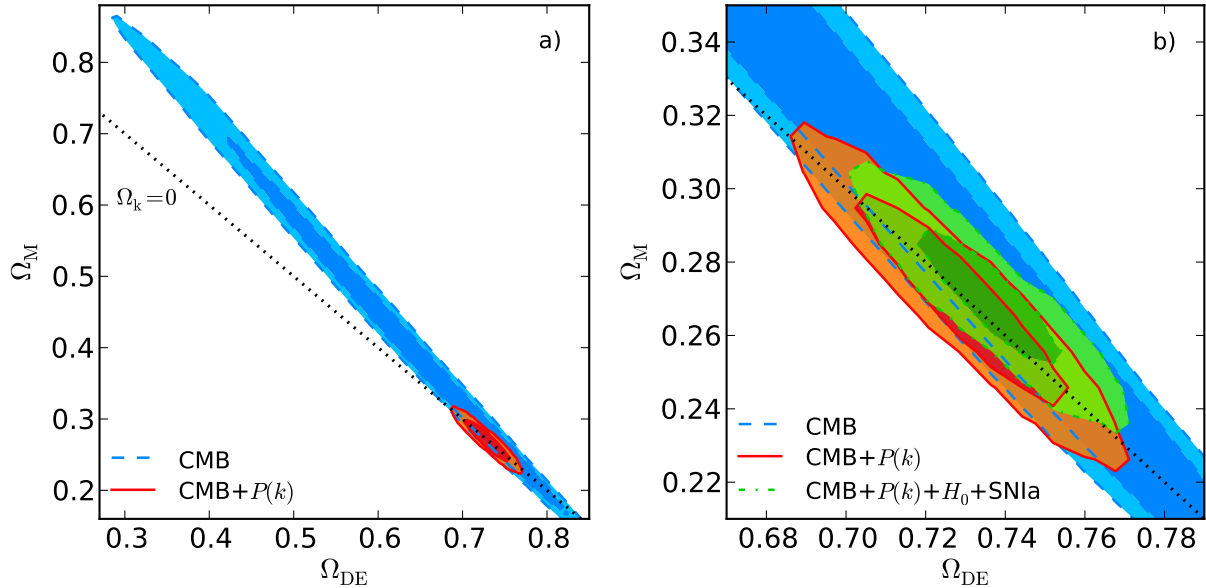


Figure 5.10: Two-dimensional marginalised constraints of the $k\Lambda\text{CDM}$ parameter space in the $\Omega_{\text{DE}} - \Omega_{\text{M}}$ plane. Colour and line coding is the same as in Figure 5.9. Panel *b)* zooms into panel *a)* in order to highlight the constraints obtained when combining CMB with the other datasets used in this work. The diagonal dotted line corresponds to a flat Universe.

lines, the same parameter planes as above when explored combining CMB and large scale structure information. Panel *b)* of Figure 5.10 shows a zoom of the constraints of panel *a)* in the area around $\Omega_{\text{DE}} = 0.73$ and $\Omega_{\text{M}} = 0.28$ in order to show with more details the constraints when more information is added to CMB data. The galaxy power spectrum is very sensitive to the matter density. Additionally the BAOs allow to measure the angular diameter distance to the mean redshift of the LRG sample, $\bar{z} = 0.28$. The degeneracies in the CMB alone are therefore strongly reduced when LSS measurements are included. The four variables discussed in the previous paragraphs become $\Omega_{\text{DE}} = 0.731 \pm 0.019$, $\Omega_{\text{M}} = 0.267_{-0.021}^{+0.020}$, $H_0 = 71.3 \pm 2.5$ and $\Omega_{\text{k}} = (1.6 \pm 5.4) \times 10^{-3}$: their errors are almost one order of magnitude smaller than in the CMB only case. With respect to the corresponding ΛCDM case, the uncertainties on the first three quantities increase up to 50%.

The inclusion of SNIa and H_0 measurement decreases the errors on curvature by about 10% ($\Omega_{\text{k}} = (3_{-4.7}^{+4.8}) \times 10^{-3}$) and on the other three parameters considered before by circa 20% ($\Omega_{\text{DE}} = 0.734_{-0.015}^{+0.015}$, $\Omega_{\text{M}} = 0.263_{-0.015}^{+0.016}$ and $H_0 = 71.9_{-2.0}^{+1.9}$). When comparing with the results from the previous section, the errors on dark energy and matter density are unchanged, while increasing by less than 40% for the Hubble parameters. The two-dimensional marginalised constraints in the $\Omega_{\text{DE}} - \Omega_{\text{M}}$ and $\Omega_{\text{DE}} - H_0$ planes are shown in panel *b)* of Figure 5.10 and in Figure 5.11 with green shaded lines enclosed by dot-dashed lines.

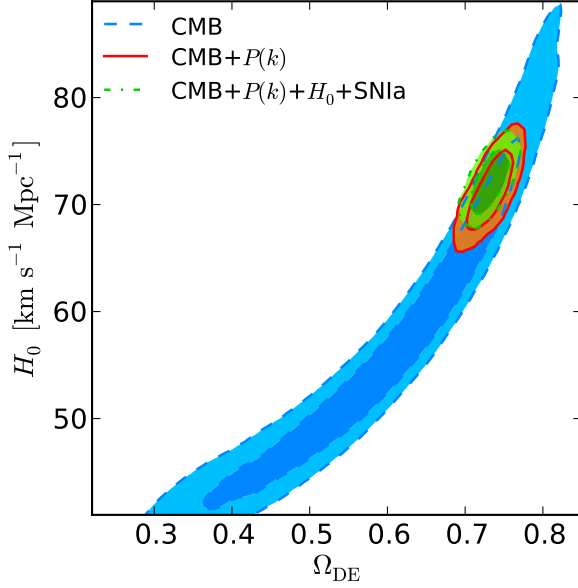


Figure 5.11: Two-dimensional marginalised constraints of the Λ CDM parameter space in the $\Omega_{\text{DE}} - H_0$ plane. Colour and line coding is the same as in Figure 5.9.

Table 5.6: Marginalised constraints on the cosmological parameters of the w CDM parameter space from the combination of probes listed in the header of the table. The quoted values are as in Table 5.3.

	CMB	CMB+ $P(k)$	CMB+ $P(k)$ + H_0	CMB+ $P(k)$ +SNIa	CMB+ $P(k)$ + H_0 +SNIa
$100\omega_b$	$2.242^{+0.053}_{-0.054}$	$2.251^{+0.049}_{-0.050}$	$2.256^{+0.049}_{-0.049}$	$2.250^{+0.051}_{-0.052}$	$2.257^{+0.048}_{-0.050}$
$100\omega_{\text{DM}}$	$11.01^{+0.53}_{-0.53}$	$11.25^{+0.43}_{-0.43}$	$11.28^{+0.44}_{-0.44}$	$11.26^{+0.40}_{-0.41}$	$11.25^{+0.40}_{-0.40}$
100Θ	$1.0397^{+0.0023}_{-0.0022}$	$1.0402^{+0.0022}_{-0.0022}$	$1.0403^{+0.0021}_{-0.0021}$	$1.0403^{+0.0021}_{-0.0021}$	$1.0404^{+0.0020}_{-0.0020}$
τ	$0.088^{+0.015}_{-0.015}$	$0.086^{+0.015}_{-0.015}$	$0.087^{+0.014}_{-0.014}$	$0.086^{+0.015}_{-0.014}$	$0.086^{+0.014}_{-0.014}$
w_{DE}	$-0.742^{+0.324}_{-0.303}$	$-1.022^{+0.129}_{-0.128}$	$-1.069^{+0.107}_{-0.106}$	$-1.009^{+0.069}_{-0.069}$	$-1.025^{+0.066}_{-0.065}$
n_s	$0.959^{+0.014}_{-0.014}$	$0.962^{+0.012}_{-0.012}$	$0.962^{+0.012}_{-0.012}$	$0.961^{+0.012}_{-0.012}$	$0.963^{+0.012}_{-0.012}$
$\log(10^{10} A_s)$	$3.064^{+0.032}_{-0.033}$	$3.073^{+0.034}_{-0.033}$	$3.076^{+0.033}_{-0.032}$	$3.073^{+0.032}_{-0.032}$	$3.074^{+0.032}_{-0.031}$
Ω_{DE}	$0.637^{+0.123}_{-0.133}$	$0.732^{+0.028}_{-0.028}$	$0.743^{+0.020}_{-0.020}$	$0.729^{+0.018}_{-0.018}$	$0.735^{+0.015}_{-0.016}$
Age [Gyr]	$14.062^{+0.431}_{-0.396}$	$13.733^{+0.118}_{-0.117}$	$13.692^{+0.095}_{-0.099}$	$13.736^{+0.102}_{-0.102}$	$13.713^{+0.090}_{-0.089}$
Ω_{M}	$0.363^{+0.133}_{-0.123}$	$0.268^{+0.028}_{-0.028}$	$0.257^{+0.020}_{-0.020}$	$0.271^{+0.018}_{-0.018}$	$0.265^{+0.016}_{-0.015}$
σ_8	$0.726^{+0.085}_{-0.090}$	$0.818^{+0.065}_{-0.064}$	$0.838^{+0.059}_{-0.060}$	$0.810^{+0.042}_{-0.043}$	$0.817^{+0.043}_{-0.042}$
z_{re}	$10.6^{+1.2}_{-1.2}$	$10.4^{+1.2}_{-1.2}$	$10.4^{+1.1}_{-1.1}$	$10.4^{+1.2}_{-1.2}$	$10.3^{+1.2}_{-1.2}$
H_0 [km s $^{-1}$ Mpc $^{-1}$]	$63.1^{+10.6}_{-11.2}$	$71.2^{+3.8}_{-3.8}$	$72.8^{+2.8}_{-2.8}$	$70.7^{+2.0}_{-2.0}$	$71.4^{+1.7}_{-1.7}$

5.4.3 Beyond the cosmological constant

In sections 5.4.1 and 5.4.2 I assume that dark energy is modelled as a cosmological constant. Despite its simplicity and its success in describing simultaneously many independent observations, the present day value of the density of dark energy does not have a solid physical explanation; this led, in the past decade, to the exploration of a large number of alternative models, most of which present a time dependent equation of state parameter⁶. Ideally, one would like to be able to constrain the full time, or redshift, dependence of $w_{\text{DE}}(z)$ in order to restrict the range of possible models. Usually, parametric forms for this parameter are assumed, which allow to measure time dependencies, but do not necessarily reproduce the correct $w_{\text{DE}}(z)$. It is possible to overcome some of these limitations with non-parametric approaches and principal component analysis (see e.g., Huterer & Starkman, 2003; Serra et al., 2009; Holsclaw et al., 2010). In this section I assume the simplest parametric form possible: w_{DE} is a constant, independent of time, with a flat prior in the range $[-2, 0]$. Deviations from this value would suggest that the cosmological constant is not a viable model of dark energy. If this is the case, the results shown in the previous two sections could be biased as consequence of wrongly assuming that dark energy is described by Λ . In section 5.4.5 I will analyse an alternative scenario in which w_{DE} is parametrized as a linear function of the scale factor.

Table 5.6 lists the constraints on the cosmological parameters as obtained for the different combinations of datasets analysed in this work. They are in perfect agreement with the ones presented with the previous two parameter spaces.

The left panel of Figure 5.12 shows the constraints in the $\Omega_{\text{DE}} - w_{\text{DE}}$ plane. The horizontal dotted line corresponds to $w_{\text{DE}} = -1$. If the CMB alone is considered a strong degeneracy between these two parameters is present, as shown by the blue shaded areas enclosed by dashed lines. The reason for this degeneracy is analogous to the case analysed in the previous section when curvature is left as a free parameter. In fact, while dark energy is subdominant at early times and does not influence the physical scale of the acoustic peaks, its equation of state and density have a strong effect in the angular diameter distance to the last scattering surface. Thus different combinations of ω_{DM} , ω_{b} and w_{DE} can result in the same apparent position of the acoustic oscillations in the CMB temperature power spectrum. The constraints on the dark energy density and equation of state parameters are therefore very weak: $\Omega_{\text{DE}} = 0.64_{-0.13}^{+0.12}$ and $w_{\text{DE}} = -0.74_{-0.30}^{+0.32}$.

With the inclusion of the LRG data, the degeneracies of the CMB only case are broken, as shown in the panel a) of Figure 5.12 (solid line enclosing red areas). From the same figure it is clear that the impact of supernovae and H_0 (dot-dashed line enclosing green areas) information is much larger in this framework than in the previous two. In order to understand what causes such a difference, I show in panel b) of Figure 5.12 also the two-dimensional constraints obtained from the combination of CMB+ $P_{\text{LRG}}(k)$ +SNIa (dashed lines enclosing blue areas). The horizontal line corresponds to $w_{\text{DE}} = -1$. The plot shows clearly that supernovae have a large constraining power for this parameter space. The supernovae luminosity-distance relation traces the expansion history of the Universe and

⁶All theories of modified gravity can be also represented through an effective $w_{\text{DE}}(z)$.

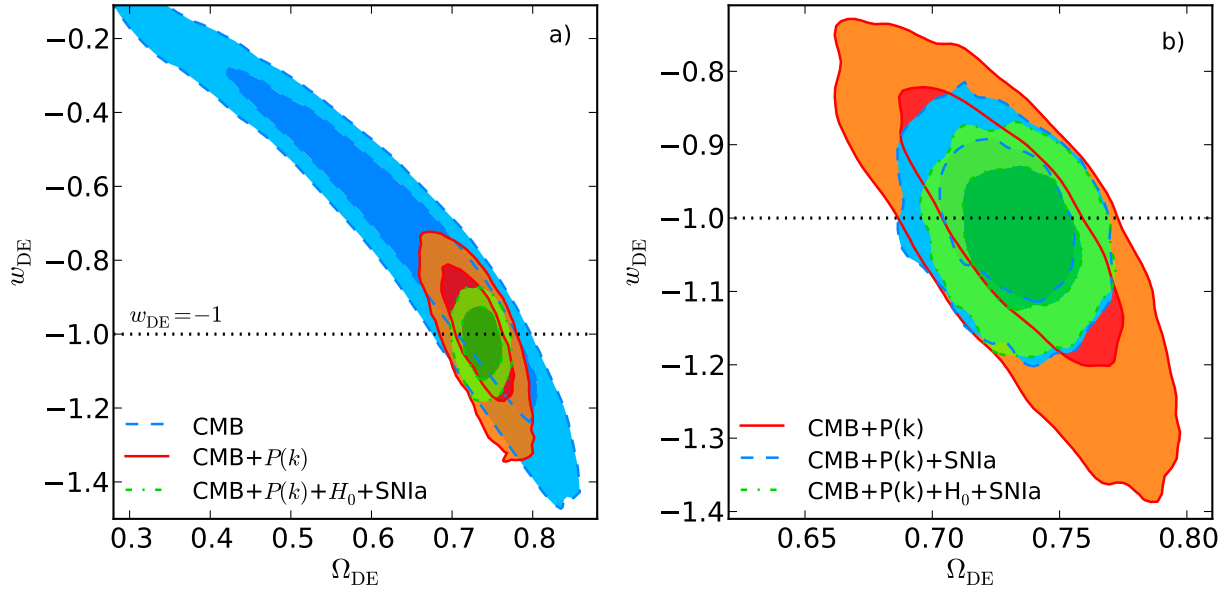


Figure 5.12: Panel *a*): two-dimensional marginalised constraints of the w CDM parameter space in the $w_{\text{DE}} - \Omega_{\text{DE}}$ plane. Colour and line coding is the same as in Figure 5.9. Panel *b*): same as the panel *a*), but for $\text{CMB}+P_{\text{LRG}}(k)$, red areas within solid lines, $\text{CMB}+P_{\text{LRG}}(k)+\text{SNIa}$, blue areas within dashed lines, and $\text{CMB}+P_{\text{LRG}}(k)+H_0+\text{SNIa}$, green areas within dot-dashed lines. Note that the right panel is a zoom of the left one in the region occupied by the $\text{CMB}+P_{\text{LRG}}(k)$ contours. The dotted horizontal lines show $w_{\text{DE}} = -1$

clearly identifies the transition between the deceleration and acceleration phases (Riess et al., 2004). This transition depends on the densities of the cosmic components and is very sensitive to the dark energy equation of state. The inclusion of a precise measurement of H_0 increases the precision on the parameters by a small factor. The constraints on the dark energy equation of state are i) $w_{\text{DE}} = -1.02 \pm 0.13$, from $\text{CMB}+P_{\text{LRG}}(k)$, ii) $w_{\text{DE}} = -1.07 \pm 0.11$, from $\text{CMB}+P_{\text{LRG}}(k)+H_0$, iii) $w_{\text{DE}} = -1.009 \pm 0.069$, $\text{CMB}+P_{\text{LRG}}(k)+\text{SNIa}$ and iv) $w_{\text{DE}} = -1.025^{+0.066}_{-0.065}$, from $\text{CMB}+P_{\text{LRG}}(k)+H_0+\text{SNIa}$. Therefore the inclusion of the large scale structure measurements decreases the error on w_{DE} by about a factor 3 and SNIa further halve it.

The main result of this section is that, when combining CMB, LSS, SNIa information with the prior on H_0 , the equation of state of dark energy parameter is constrained to be -1 with about 6.5% accuracy. This, although perfectly compatible with the cosmological constant models, does not exclude other dark energy scenarios. Excluding CMB, which has very little constraining power, the other three experiments give access only to redshift $z \lesssim 1$. Furthermore many dark energy models can be tuned in order to mimic Λ at low redshifts and deviate from it at earlier epochs. In order to narrow down the range of possible models even further, more precise measurements spanning a larger range of redshifts, together with the inclusion of tests of the growth of structures, will be necessary.

	no systematics	MLCS2K2
$100\omega_b$	$2.257^{+0.047}_{-0.048}$	$2.264^{+0.048}_{-0.049}$
$100\omega_{\text{DM}}$	$11.21^{+0.40}_{-0.40}$	$11.05^{+0.41}_{-0.41}$
100Θ	$1.0405^{+0.0021}_{-0.0021}$	$1.0411^{+0.0021}_{-0.0022}$
τ	$0.087^{+0.014}_{-0.014}$	$0.089^{+0.014}_{-0.014}$
w_{DE}	$-1.007^{+0.046}_{-0.046}$	$-0.875^{+0.054}_{-0.055}$
n_s	$0.962^{+0.012}_{-0.012}$	$0.964^{+0.012}_{-0.012}$
$\log(10^{10} A_s)$	$3.074^{+0.032}_{-0.032}$	$3.072^{+0.032}_{-0.033}$
Ω_{DE}	$0.732^{+0.013}_{-0.014}$	$0.704^{+0.017}_{-0.017}$
Age [Gyr]	$13.719^{+0.091}_{-0.090}$	$13.795^{+0.095}_{-0.093}$
Ω_{M}	$0.268^{+0.014}_{-0.013}$	$0.296^{+0.017}_{-0.017}$
σ_8	$0.809^{+0.036}_{-0.036}$	$0.752^{+0.037}_{-0.037}$
z_{re}	$10.4^{+1.2}_{-1.1}$	$10.5^{+1.1}_{-1.2}$
H_0 [km s ⁻¹ Mpc ⁻¹]	$71.0^{+1.2}_{-1.2}$	$67.2^{+1.5}_{-1.5}$

Table 5.7: Marginalised constraints on the cosmological parameters of the Λ CDM parameter space from the combination of CMB+ $P_{\text{LRG}}(k)$ + H_0 +SNIa when systematic errors are not considered and when the MLCS2K2 SNIa light curve fitter is used.

Effects of supernovae systematics and light curve fitters

Similarly to what has been done in section 5.4.1, I test the impact of SNIa systematic effects and different light curve fitters on the measured cosmological parameters. The constraints for these two cases are listed in Table 5.7. As before, I find that neglecting systematics does not change the mean values of the parameters, but generally reduces the associated errors. In particular the constraints on the dark energy equation of state are reduced by almost 30%, $w_{\text{DE}} = -1.01 \pm 0.046$. The use of the data from the SDSS SN project, with the light curves fitted with MLCS2K2, changes some of the parameters, as for instance H_0 , w_{DE} and Ω_{M} , by more than 2- σ with respect to the values in my standard case. In particular I measure w_{DE} to be $-0.875^{+0.054}_{-0.055}$. This highlights, better than for the Λ CDM case, the importance of SNIa modelling in improving cosmological constraints from future generation experiments.

5.4.4 Curvature and dark energy equation of state as free parameters

I now analyse the accuracy that can be achieved when both w_{DE} and Ω_k are considered as free parameters. The full list of constraints on the cosmological parameters for the kwCDM cosmology is summarised in Table 5.8.

The introduction of an extra degree of freedom with respect to the previous two sections affects the CMB degeneracy already discussed. The two-dimensional marginalised

Table 5.8: Marginalised constraints on the cosmological parameters of the Λ CDM parameter space from the combination of probes listed in the header of the table. The quoted values are as in Table 5.3.

	CMB	CMB+ $P(k)$	CMB+ $P(k)$ + H_0	CMB+ $P(k)$ +SNIa	CMB+ $P(k)$ + H_0 +SNIa
$100\omega_b$	$2.236^{+0.052}_{-0.052}$	$2.241^{+0.047}_{-0.047}$	$2.255^{+0.048}_{-0.048}$	$2.246^{+0.047}_{-0.047}$	$2.251^{+0.050}_{-0.049}$
$100\omega_{\text{DM}}$	$11.04^{+0.52}_{-0.52}$	$11.29^{+0.43}_{-0.44}$	$11.32^{+0.46}_{-0.45}$	$11.27^{+0.43}_{-0.43}$	$11.30^{+0.45}_{-0.46}$
100Θ	$1.0397^{+0.0022}_{-0.0022}$	$1.0400^{+0.0020}_{-0.0021}$	$1.0401^{+0.0021}_{-0.0021}$	$1.0401^{+0.0022}_{-0.0022}$	$1.0402^{+0.0021}_{-0.0022}$
τ	$0.087^{+0.014}_{-0.014}$	$0.086^{+0.014}_{-0.014}$	$0.087^{+0.015}_{-0.015}$	$0.086^{+0.014}_{-0.014}$	$0.085^{+0.014}_{-0.014}$
$100\Omega_k$	$-2.72^{+6.28}_{-6.51}$	$2.72^{+2.18}_{-2.13}$	$1.69^{+2.11}_{-1.92}$	$0.33^{+0.71}_{-0.72}$	$0.45^{+0.65}_{-0.65}$
w_{DE}	$-0.907^{+0.524}_{-0.607}$	$-0.685^{+0.200}_{-0.207}$	$-0.856^{+0.262}_{-0.272}$	$-0.973^{+0.091}_{-0.088}$	$-0.981^{+0.083}_{-0.084}$
n_s	$0.956^{+0.013}_{-0.013}$	$0.959^{+0.012}_{-0.012}$	$0.962^{+0.012}_{-0.012}$	$0.960^{+0.012}_{-0.012}$	$0.961^{+0.012}_{-0.012}$
$\log(10^{10} A_s)$	$3.063^{+0.033}_{-0.032}$	$3.074^{+0.032}_{-0.032}$	$3.077^{+0.032}_{-0.033}$	$3.072^{+0.032}_{-0.032}$	$3.073^{+0.031}_{-0.032}$
Ω_{DE}	$0.566^{+0.139}_{-0.153}$	$0.671^{+0.047}_{-0.045}$	$0.710^{+0.042}_{-0.043}$	$0.728^{+0.017}_{-0.017}$	$0.733^{+0.016}_{-0.017}$
Age [Gyr]	$15.01^{+1.78}_{-1.88}$	$13.11^{+0.47}_{-0.45}$	$13.24^{+0.57}_{-0.58}$	$13.61^{+0.33}_{-0.32}$	$13.53^{+0.29}_{-0.29}$
Ω_M	$0.461^{+0.197}_{-0.176}$	$0.302^{+0.030}_{-0.031}$	$0.273^{+0.026}_{-0.026}$	$0.268^{+0.017}_{-0.017}$	$0.262^{+0.016}_{-0.016}$
σ_8	$0.725^{+0.109}_{-0.117}$	$0.692^{+0.080}_{-0.077}$	$0.757^{+0.106}_{-0.102}$	$0.797^{+0.044}_{-0.045}$	$0.802^{+0.044}_{-0.043}$
z_{re}	$10.6^{+1.3}_{-1.3}$	$10.7^{+1.2}_{-1.2}$	$10.6^{+1.2}_{-1.2}$	$10.4^{+1.2}_{-1.1}$	$10.4^{+1.2}_{-1.2}$
H_0 [km s $^{-1}$ Mpc $^{-1}$]	$56.7^{+11.2}_{-11.5}$	$67.2^{+3.4}_{-3.3}$	$70.8^{+3.2}_{-3.2}$	$71.0^{+2.2}_{-2.2}$	$71.9^{+2.0}_{-2.0}$

constraints in the $w_{\text{DE}} - \Omega_k$ and $w_{\text{DE}} - \Omega_{\text{DE}}$ planes from CMB data only are shown in the panels of Figure 5.13 with the blue shaded areas within dashed lines. By comparing panel b) of Figure 5.13 with panel a) of Figure 5.12 it becomes clear that the allowed area in the parameter space increases because of the larger degeneracy. This causes the errors on Ω_k and w_{DE} to increase by 50-60% with respect to the corresponding cases in sections 5.4.2 and 5.4.3.

The red contours within solid lines in both panels of Figure 5.13 show the constraints in the $w_{\text{DE}} - \Omega_k$ and $w_{\text{DE}} - \Omega_{\text{DE}}$ planes from the combination of CMB with the LRG data. The inclusion of the power spectrum reduces the region allowed by CMB alone to a one-dimensional degeneracy, that can be broken using the information of the amplitude of $P_{\text{LRG}}(k)$. Because of this a degeneracy arises between the bias and the shape of the power spectrum when both the curvature and the dark energy equation of state are treated as free parameters. When considering the range of scales $0.02 h \text{ Mpc}^{-1} \leq k \leq 0.15 h \text{ Mpc}^{-1}$ larger values of w_{DE} , Ω_M and Ω_k and lower values of σ_8 can be compensated by unphysically large biases b and larger values of A_{MC} in order to obtain a comparable χ^2 . The use of a finite flat prior on b would decrease the large Ω_k and w_{DE} tail and reduce the degeneracy. Alternatively, the detection of the turnover in the power spectrum, not possible nowadays

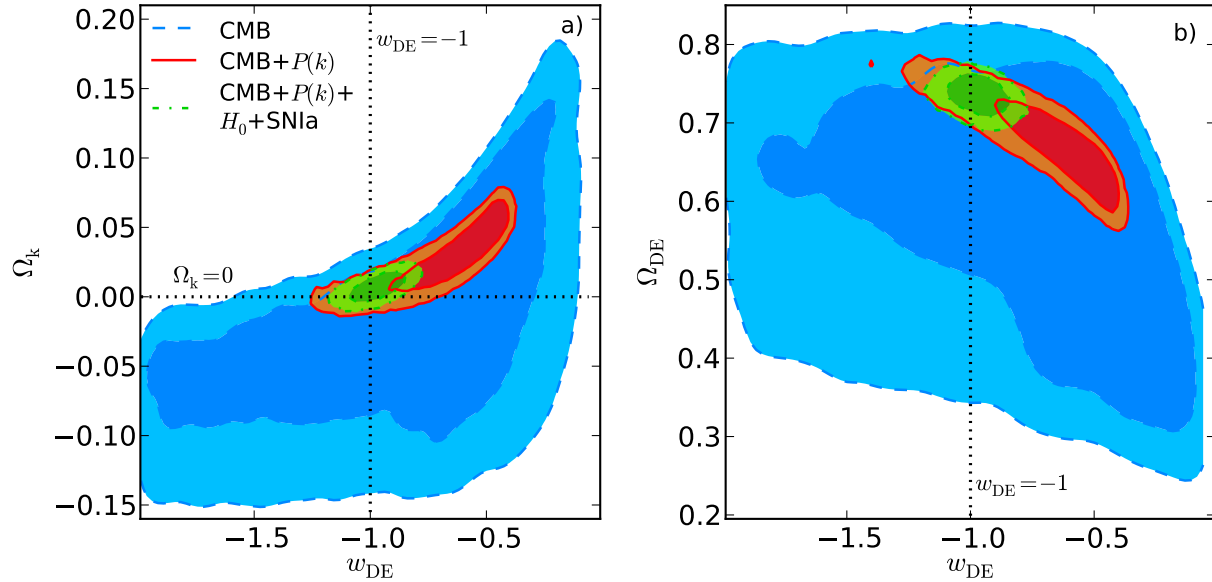


Figure 5.13: Panel *a)*: two-dimensional marginalised constraints of the kwCDM parameter space in the $w_{\text{DE}} - \Omega_k$ plane. Colour and line coding is the same as in Figure 5.9. The horizontal and vertical dotted lines show the values of these parameters for the flat Λ CDM case. Panel *b)*: two-dimensional marginalised constraints in the $w_{\text{DE}} - \Omega_{\text{DE}}$ plane. The vertical dotted line shows $w_{\text{DE}} = -1$

because of the still too small volume probed by galaxy surveys, might help in constraining better its overall shape and break the degeneracy just described.

The addition of H_0 and supernovae measurements breaks the bias-shape degeneracy, returning parameters perfectly consistent with the Λ CDM cosmology. As for the previous section, the biggest change in precision is due to the SN, which improves the accuracy of the three parameters previously discussed by a factor 2-3. The final constraints, when all four probes are used, are shown in the two panels of Figure 5.13 by the green shaded areas enclosed within dot-dashed lines. For the quantities shown in the plot we obtain $\Omega_k = (4.5 \pm 6.5) \times 10^{-3}$ (36% increase in the errors with respect to $k\Lambda$ CDM case), $w_{\text{DE}} = -0.981_{-0.084}^{+0.083}$ (29% increase in the errors with respect to the wCDM case) and $\Omega_{\text{DE}} = 0.733_{-0.017}^{+0.016}$ (8% increase with respect to both).

5.4.5 Time varying dark energy equation of state parameter

In section 5.4.3 I encode possible deviations from the cosmological constant model with a constant effective dark energy equation of state. In this section I include explicitly a time dependency on w_{DE} through the simple parameterization of equation (5.6). I treat the two parameters of this model, w_0 and w_a as free. I consider only the case in which the curvature is held fixed to 0. The constraints on the cosmological parameters for the cosmology analysed in this section from the different combinations of probes are listed in

Table 5.9: Marginalised constraints on the cosmological parameters of the w aCDM parameter space from the combination of probes listed in the header of the table. The quoted values are as in Table 5.3.

	CMB	CMB+ $P(k)$	CMB+ $P(k)$ + H_0	CMB+ $P(k)$ +SNIa	CMB+ $P(k)$ + H_0 +SNIa
$100\omega_b$	$2.249^{+0.052}_{-0.053}$	$2.253^{+0.050}_{-0.049}$	$2.255^{+0.049}_{-0.049}$	$2.251^{+0.050}_{-0.050}$	$2.257^{+0.049}_{-0.048}$
$100\omega_{\text{DM}}$	$10.99^{+0.52}_{-0.52}$	$11.27^{+0.43}_{-0.43}$	$11.31^{+0.43}_{-0.43}$	$11.30^{+0.43}_{-0.44}$	$11.29^{+0.45}_{-0.45}$
100Θ	$1.0399^{+0.0022}_{-0.0022}$	$1.0402^{+0.0022}_{-0.0022}$	$1.0402^{+0.0021}_{-0.0021}$	$1.0401^{+0.0022}_{-0.0022}$	$1.0403^{+0.0021}_{-0.0021}$
τ	$0.088^{+0.015}_{-0.015}$	$0.086^{+0.014}_{-0.014}$	$0.086^{+0.014}_{-0.014}$	$0.086^{+0.015}_{-0.015}$	$0.086^{+0.014}_{-0.014}$
w_0	$-0.71^{+0.47}_{-0.49}$	$-0.75^{+0.44}_{-0.48}$	$-1.04^{+0.31}_{-0.31}$	$-0.98^{+0.14}_{-0.14}$	$-1.00^{+0.14}_{-0.14}$
w_a	$-0.32^{+1.00}_{-1.01}$	$-0.63^{+1.07}_{-0.99}$	$-0.11^{+0.85}_{-0.86}$	$-0.15^{+0.52}_{-0.52}$	$-0.13^{+0.53}_{-0.53}$
n_s	$0.961^{+0.014}_{-0.013}$	$0.961^{+0.012}_{-0.012}$	$0.962^{+0.012}_{-0.012}$	$0.960^{+0.012}_{-0.012}$	$0.962^{+0.012}_{-0.012}$
$\log(10^{10} A_s)$	$3.065^{+0.033}_{-0.033}$	$3.074^{+0.031}_{-0.032}$	$3.075^{+0.032}_{-0.033}$	$3.074^{+0.032}_{-0.033}$	$3.075^{+0.032}_{-0.032}$
Ω_{DE}	$0.665^{+0.102}_{-0.102}$	$0.702^{+0.055}_{-0.054}$	$0.741^{+0.027}_{-0.028}$	$0.728^{+0.018}_{-0.018}$	$0.734^{+0.016}_{-0.016}$
Age [Gyr]	$13.921^{+0.295}_{-0.295}$	$13.741^{+0.118}_{-0.115}$	$13.699^{+0.102}_{-0.104}$	$13.733^{+0.109}_{-0.105}$	$13.710^{+0.104}_{-0.104}$
Ω_{M}	$0.335^{+0.102}_{-0.102}$	$0.298^{+0.054}_{-0.055}$	$0.259^{+0.028}_{-0.027}$	$0.272^{+0.018}_{-0.018}$	$0.266^{+0.016}_{-0.016}$
σ_8	$0.742^{+0.082}_{-0.080}$	$0.770^{+0.108}_{-0.104}$	$0.837^{+0.077}_{-0.076}$	$0.810^{+0.043}_{-0.044}$	$0.818^{+0.045}_{-0.045}$
z_{re}	$10.5^{+1.2}_{-1.2}$	$10.4^{+1.2}_{-1.2}$	$10.4^{+1.2}_{-1.2}$	$10.4^{+1.2}_{-1.2}$	$10.4^{+1.1}_{-1.1}$
H_0 [km s $^{-1}$ Mpc $^{-1}$]	$65.0^{+9.9}_{-9.7}$	$68.2^{+6.4}_{-6.2}$	$72.6^{+3.7}_{-3.7}$	$70.6^{+2.0}_{-2.0}$	$71.4^{+1.7}_{-1.7}$

Table 5.9.

Panel a) of Figure 5.14 shows the two-dimensional marginalised constraints in the $w_0 - w_a$ plane from CMB alone (blue shaded areas within dashed lines), CMB plus LRG power spectrum (red shaded areas within solid lines) and the combination of CMB, $P_{\text{LRG}}(k)$, H_0 and SNIa (green shaded areas within dot-dashed lines). The vertical and horizontal dotted lines at $w_0 = -1$ and $w_a = 0$ show the values of the two parameters for the Λ CDM case. In the three cases a degeneracy is visible, which is reduced as more independent data are included. From CMB alone I obtain $w_0 = -0.71^{+0.47}_{-0.49}$ and $w_a = -0.32^{+1.00}_{-1.01}$; the inclusion of the LRGs power spectrum information does not change substantially the one-dimensional constraints ($w_0 = -0.75^{+0.44}_{-0.48}$ and $w_a = -0.63^{+1.07}_{-0.99}$) but increases by almost a factor 2 the figure of merit (Albrecht et al., 2006). As shown in the previous two sections, supernovae have an important role in constraining dark energy properties and the inclusion of their information reduces the errors in the two parameters by about a factor 3 and 2, with respect to the CMB+ P_{LRG} case. The one-dimensional constraints from the combination of all the datasets are $w_0 = -1.00 \pm 0.14$ and $w_a = -0.13 \pm 0.53$. The attempt to constrain also the time evolution of the dark energy equation of state parameter results in a degradation of its value at present.

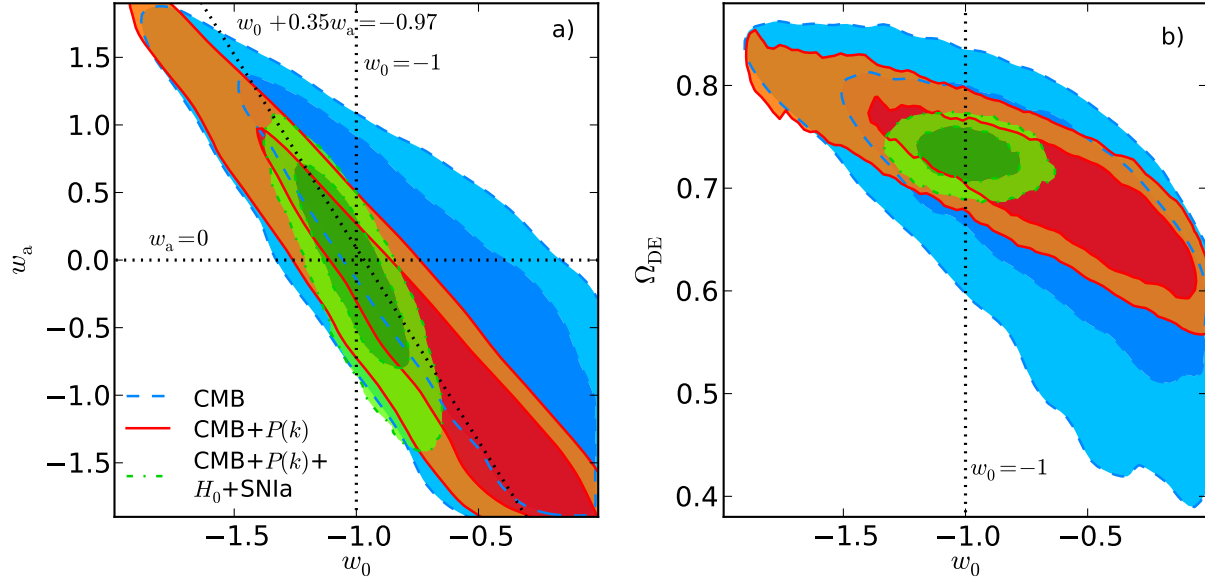


Figure 5.14: Panel *a*): two-dimensional marginalised constraints of the w aCDM parameter space in the $w_0 - w_a$ plane. Colour and line coding is the same as in Figure 5.9. The vertical and horizontal dotted lines show the values of these parameters for the flat Λ CDM case ($w_0 = -1$ and $w_a = 0$). The dotted diagonal line shows the equation $w_{\text{DE}}(a_p) = -0.97 = w_0 + (1 - a_p)w_a$, where $a_p = 0.65$ is the pivot scale factor from the combination of CMB and $P_{\text{LRG}}(k)$ (see text). Panel *b*): two-dimensional marginalised constraints in the $w_0 - \Omega_{\text{DE}}$ plane. The vertical line is for $w_0 = -1$.

From these results it is possible to reconstruct the time dependence of the dark energy equation of state parameter. The thick dashed, solid and dot-dashed lines in Figure 5.15 show the value of $w_{\text{DE}}(z)$ from CMB, CMB plus $P_{\text{LRG}}(k)$ and the combination of the four probes, respectively. The corresponding $1\text{-}\sigma$ errors, which vary with redshift, are indicated by the shaded areas within the thin lines. They are computed according to Albrecht et al. (2006) as:

$$\langle \delta w_{\text{DE}}^2(a) \rangle = \langle (\delta w_0 + (1 - a)\delta w_a)^2 \rangle. \quad (5.9)$$

In the redshift range shown in the plot, w_{DE} is always compatible with a cosmological constant at the 1σ level. Furthermore the errors show a minimum at a redshift called “pivot” (Huterer & Turner, 2001; Hu & Jain, 2004; Albrecht et al., 2006). For the three cases shown in Figure 5.15, I obtain a pivot redshift of $z_p = 0.4$ (CMB), $z_p = 0.54$ (CMB+ $P_{\text{LRG}}(k)$) and $z_p = 0.3$ (CMB+ $P_{\text{LRG}}(k)$ + H_0 +SNIa) and an equation of state $w_{\text{DE}}(z_p) = -0.80 \pm 0.37$, $w_{\text{DE}}(z_p) = -0.97 \pm 0.29$ and $w_{\text{DE}}(z_p) = -1.03 \pm 0.07$. It is interesting to note that in the last case the precision is comparable to the one presented in Section 5.4.3. The diagonal dotted line in panel a) of Figure 5.14 shows that the degeneracy between w_0 and w_a is very close to $w_0 + (1 - a_p)w_a = -0.97$, where $a_p = 0.65$ is the pivot scale factor from the CMB+ $P_{\text{LRG}}(k)$ constraints.

Panel b) of Figure 5.14 shows the two-dimensional marginalised constraints in the

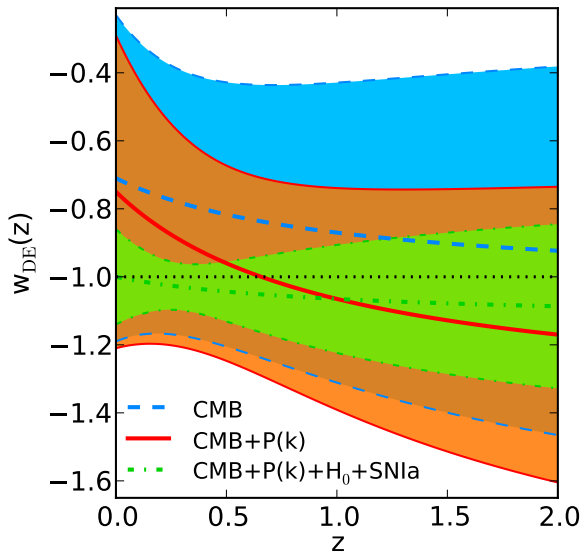


Figure 5.15: $w_{\text{DE}}(z)$ as function of the redshift z as obtained from the constraints shown in panel a) of Figure 5.14. The thick dashed blue, solid red and green dot-dashed lines correspond to the mean $w_{\text{DE}}(z)$ for CMB, CMB+ $P_{\text{LRG}}(k)$ and CMB+ $P_{\text{LRG}}(k)+H_0+\text{SNIa}$. The blue, red and green shaded areas enclosed within the outermost dashed, solid and dot-dashed lines show the 68% confidence level for the same three combinations as computed from equation (5.9).

$w_0 - \Omega_{\text{DE}}$ plane. This figure illustrates that the addition of large scale structure information to the CMB data halves the errors on the dark energy density from $\Omega_{\text{DE}} = 0.66 \pm 0.10$ to $\Omega_{\text{DE}} = 0.702 \pm 0.055$. The inclusion of SNIa and H_0 measurements decreases the errors further by 70% to $\Omega_{\text{DE}} = 0.734 \pm 0.016$.

5.5 Comparison with previous studies

In this section I compare the results shown in this chapter with some recent works focused on the analysis of the large scale structure of the Universe.

The LRG distribution from the SDSS DR7 has already been used in order to extract cosmological parameters by Reid et al. (2010a). The analysis in that work differs from the one I have performed mostly in five important details: i) all the LRGs from the Northern Galactic Cap and the 3 southern stripes were used (110576 galaxies in 7931 deg²), ii) thanks to the count-in-cylinders technique (CiC, Reid & Spergel, 2009; Reid et al., 2009), the authors extracted a halo catalogue from the LRG distribution and then computed the halo power spectrum, iii) they computed the covariance matrix from 10000 lognormal catalogues (LN, Coles & Jones, 1991), iv) they used a model based on HALOFIT (Smith et al., 2003), that required additional calibration against numerical simulations and v) they analysed the power spectrum in the range $0.02 h \text{ Mpc}^{-1} < k < 0.2 h \text{ Mpc}^{-1}$. The advantage of using the reconstructed underlying density field, instead of the galaxies, is that the intra-halo peculiar motions, which cause the fingers-of-god, are erased, leaving weaker small scale redshift-space distortions. They combine their LRG power spectrum with the 5th year data from the WMAP satellite (WMAP5, Komatsu et al., 2009) and the Union Supernovae dataset. The comparison between the results in table 3 of Reid et al. (2010a) and the corresponding ones in this chapter (third column in Tables 5.3, 5.5, 5.6

and third and fifth columns in Table 5.8) shows that, with the exception of the Λ CDM case and despite the smaller k modes used here, the errors that I obtain are slightly smaller and that there are significant offsets in some of the parameters. For the CMB+ $P_{\text{LRG}}(k)$ in the $k\Lambda$ CDM, w CDM cosmologies and for the CMB+ $P_{\text{LRG}}(k)$ +SNIa in the k wCDM case I find our values of Ω_{M} and of H_0 to be 1.8-2.5 σ larger and smaller, respectively, than the results reported in Reid et al. (2010a). In the two latter cases the reported values of the dark energy equation of state parameter are $w_{\text{DE}} = -0.79 \pm 0.15$ and $w_{\text{DE}} = -0.99 \pm 0.11$ (to be compared with my results of $w_{\text{DE}} = -1.02 \pm 0.13$ and $w_{\text{DE}} = -0.97 \pm 0.09$). As a test, I apply the model of equation (4.4) to the power spectrum from Reid et al. (2010a)⁷ and I explore the w CDM parameter space. This shows that i) the decrease of the recovered errors is not related to the use of the small scale CMB information (ACBAR, BOOMERanG, CBI, QUAD), ii) the offsets just discussed are related to differences in the shape of the measured power spectrum or window function and not to the model used.

Percival et al. (2010) analysed almost 900,000 galaxies from the combination of the full SDSS DR7 galaxy sample and the two-degree Field Galaxy Redshift Survey (2dFGRS, Colless et al., 2003) and extracted the BAO feature from the power spectrum in 7 redshift bins. The main cosmological implications are shown in their table 5 and can be compared with the third column in Tables 5.3, 5.5 and 5.6 and with Table 5.8. Their overall results are compatible with the ones presented in Section 5.4 and with the findings of Reid et al. (2010a). Despite the much smaller sample that I use, the constraints that I obtain are comparable or tighter than the ones of Percival et al. (2010). As an example, for the w CDM case I measure, from CMB+ $P_{\text{LRG}}(k)$, $w_{\text{DE}} = -1.02 \pm 0.13$, while they report the value $w_{\text{DE}} = -0.97 \pm 0.17$, which corresponds to an improvement of about 25% in my results. This comparison suggests the importance of the use of the full information content in the galaxy power spectrum, as already noticed by different authors (e.g., Sánchez et al., 2008; Shoji et al., 2009; Blake et al., 2011).

The correlation function has also been intensively used with similar goals. Sánchez et al. (2009) applied the model of equation (4.2) to the correlation function for the LRG sample from the SDSS DR6, as measured by Cabré & Gaztañaga (2009a). Combining this with Union SNIa sample and the CMB measurements from WMAP5, as well as the position of the BAO peak along the line of sight in the two-dimensional correlation function from Gaztañaga et al. (2009), they extracted cosmological parameters for the same parameter spaces presented in this chapter. The overall results of Sánchez et al. (2009) are consistent with the ones presented in section 5.4. Combining the CMB and large scale structure information, the constraints in Sánchez et al. (2009) are very similar to the results of this thesis. Interestingly the errors on the cosmological parameters presented here are systematically smaller when curvature is kept as a free variable and larger for the w CDM and $w\Lambda$ CDM cases. This shows that the models and the measurements of the power spectrum and the correlation function, although generally coherent, might have some small differences in the sensitivity to cosmological parameters for different parameter spaces. In the k wCDM case, the constraints of Sánchez et al. (2009) show the same bias-shape

⁷publicly available at <http://lambda.gsfc.nasa.gov/toolbox/lrgdr/>

degeneracy that shifts the values of Ω_k and w_{DE} towards higher values with respect to the flat Λ CDM paradigm (compare panel a of Figure 5.13 with figure 14 in Sánchez et al. 2009). The inclusion of SNIa and of H_0 (radial BAO) in mine (their) analysis leads to the tightest constraints in both works. For flat and non flat Λ CDM models, the differences are negligible, while for the other three cases, where SNIa measurements play an important role, the errors that I obtain are larger: this is due to the inclusion in my analysis of the supernovae systematic errors, which were neglected in Sánchez et al. (2009). When I do not use the systematics, I obtain tighter constraints, shown by the middle column of Table 5.7. In this case I measure the dark energy equation of state parameter to be $w_{DE} = -1.007 \pm 0.046$, about 11% tighter than the corresponding value measured by Sánchez et al. (2009) $w_{DE} = -0.969 \pm 0.052$.

A more recent analysis of the correlation function from the DR7 LRG sample has been made by Chuang et al. (2010), using a simplified version of the model presented by Reid et al. (2010a). They combined this measurement with WMAP7 and Union2 data in order to extract cosmological parameters. Some of their constraints are offset by 1-2 σ with respect to my findings, while their measurements of the dark energy equation of state parameter are compatible with what I obtain, once the SNIa systematics are neglected. Carnero et al. (2011) measured the angular correlation function and detected the BAO feature from the LRGs in the SDSS DR7 photometric catalogue, which consists of a sample of about 1.5 million galaxies. Fixing all the other parameters, except H_0 , to the best fit from WMAP7, they measure w_{DE} to be -1.03 ± 0.16 .

Also the small scale clustering has been used to perform cosmological analyses. From the small scale projected correlation function and mass-number ratio in clusters, modelled in the halo model framework, Tinker et al. (2011) extracted cosmological and model parameters, obtaining, when combining with WMAP7, $\Omega_M = 0.290 \pm 0.016$ and $\sigma_8 = 0.826 \pm 0.02$. The difference between these results and the values of Table 5.3 might be due to the smaller number of cosmological degrees of freedom and the higher number of model parameters.

In a recent article Blake et al. (2011) presented the first cosmological results from the WiggleZ survey (Drinkwater et al., 2010). They used a sample of about 130,000 emission line galaxies across 1000 deg² in the redshift range $0.3 < z < 0.9$. From the correlation function, the power spectrum, the BAOs and the band-filtered correlation function of the sample (Xu et al., 2010) they extracted BAO parameters, like the effective distance $D_V(z)$ of equation (4.6) and the ‘‘acoustic parameter’’, defined by $A(z) \equiv D_V \sqrt{\Omega_M H_0^2} / cz$ (Eisenstein et al., 2005). From those, they measured cosmological parameters for the Λ CDM and the wCDM models. When using LSS information only, the uncertainties are large but the results show a strong preference for the presence of dark energy, with $w_{DE} = -1.6_{-0.7}^{+0.6}$. Combining the BAO parameters with WMAP7 distance priors they measured the dark energy equation of state parameter to be $w_{DE} = -0.982_{-0.189}^{+0.154}$, which became $w_{DE} = -1.026 \pm 0.081$ if also Union2 SN are used. Those results are in agreement with mine, although their uncertainties are about 20-30% larger than the ones that I show in Table 5.6. The agreement between my results and the findings in Blake et al. (2011) shows that both analyses, despite the differences in the galaxies selected, the survey volume and geometry and the procedure used to extract cosmological information, are robust enough

for the precision achievable today.

Conclusion and outlook

The increasing quantity and quality of information from large galaxy redshift surveys demands models able to describe the clustering of the galaxy distribution with high accuracy. The shape of the power spectrum, the tool most commonly used to analyse galaxy clustering, is distorted by non-linear evolution, bias and redshift-space distortions. These effects complicate the relation between the observations and the predictions of linear perturbation theory, making the interpretation of these measurements in terms of constraints on cosmological parameters more difficult.

In Chapter 4 I present a model for the full shape of the large-scale power spectrum which is based on RPT and is analogous to the approach followed by Crocce & Scoccimarro (2008) and Sánchez et al. (2008) for the two-point correlation function. I compare the model against power spectra measured from a suite of 50 large volume, moderate resolution N-body simulations, called L-BASICC II (Angulo et al., 2008; Sánchez et al., 2008). My results indicate that the simple model presented here can provide an accurate description of the full shape of the power spectrum taking into account the effects of non-linear evolution, redshift space distortions and halo bias for scales $k \lesssim 0.15 h \text{ Mpc}^{-1}$, making it a valuable tool for the analysis of real datasets.

When applied to the dark matter distribution, the accuracy of the model in recovering the shape of the power spectrum increases with redshift, as non-linear effects become less important. Even though this holds both in real and redshift space, in the latter case the model performs slightly worse, since it does not include explicitly the effect of scale dependent redshift space distortions. The model also gives a correct description of the shape of the halo power spectrum for different mass ranges both for real and redshift space information. In the latter case, due to the absence of the non-linear contribution from the fingers-of-god effect, the scale dependence of the redshift space distortions is simplified and the obtained constraints on the stretch parameter are similar to the ones of the real space case.

Sánchez et al. (2008) performed a similar analysis for the shape of the large scale two-point correlation function. Their results showed that non-linear evolution, redshift space distortions and bias are simpler to deal with for the case of the correlation function than for

the power spectrum, where the signature is highly scale dependent. However, it is necessary to pursue complementary approaches to constrain cosmological parameters, in order to allow for a comparison of the obtained results and a check for possible systematics. The model for the shape of the power spectrum presented here is proven to provide constraints on the stretch parameter α similar to the ones obtained by Sánchez et al. (2008). Thus, with an accurate modelling, it is possible to extract cosmological information with the same precision from both statistics.

Using a similar set of simulations to the L-BASICC II, Angulo et al. (2008) tested a model in which the information from the broad band shape of the power spectrum is discarded in order to extract a measurement of the BAO oscillations alone. A comparison of their results with mine shows that the extra information in the full shape of the power spectrum helps to improve the obtained constraints over the BAO alone case (see also, e.g., Shoji et al., 2009). In fact, despite the relatively small number of wave modes included in our analysis, the constraints that we obtain on α are slightly tighter than those of Angulo et al. (2008).

In Chapter 5 I apply this model to the power spectrum of about 90,000 luminous red galaxies, extracted from the spectroscopic part of the seventh data release of the Sloan Digital Sky survey. To estimate the covariance matrix I make use of the 160 LasDamas mock catalogues which mimic the angular and redshift distribution of the observed LRGs.

Combining the large scale structure information with measurements of the CMB temperature and polarisation power spectrum from the seven year data release of WMAP, ACBAR, BOOMERanG, CBI and QUAD, the luminosity-distance relation from the Union2 supernova sample and a precise determination of the local Hubble parameter as a prior, I explore the constraints in five different cosmological parameter spaces described in Section 5.3.1. The first two are the flat Λ CDM concordance model and a similar one where curvature is a free parameter (k Λ CDM). I also consider three cases in which the dark energy equation of state has a parametric form: in two cases it is assumed to be constant, with and without the assumption of a flat geometry (w Λ CDM and kw Λ CDM), and in the last case (wa Λ CDM) I model w_{DE} as a simple linear function of the scale factor as in equation (5.6).

Overall, I obtain tight constraints on the cosmological parameters for the five cases analysed and I do not detect deviations from the flat Λ CDM paradigm. The different combinations of the four experiments used in this analysis do not show evidence of tensions between cosmological probes. I find that the curvature is null at $1-\sigma$ level with errors of the order of $10^{-2} - 10^{-3}$. I measure the dark energy equation of state parameter to be consistent with a cosmological constant with 13% uncertainty for CMB+ $P_{\text{LRG}}(k)$ and 6.5% uncertainty for CMB+ $P_{\text{LRG}}(k)$ + H_0 +SNIa in the flat w Λ CDM case. If I discard the systematic errors in the SNIa, the precision increases to 4.6%. In the kw Λ CDM, because of the added degree of freedom, I have a degradation of the constraints by 8.4%, when combining all the four samples. The constraints obtained with the CMB and large scale structure together are shifted by $1.5-2\sigma$ with respect to the best fit Λ CDM because of a degeneracy between the bias and the power spectrum shape that allows very large, and unphysical, values of the bias when w_{DE} , Ω_{M} , Ω_{k} increase and σ_8 decreases. If I assume the parametric form of equation (5.6) for the dark energy equation of state, I do not detect

any time variation and I obtain $w_{\text{DE}}(z = 0.54) = -0.97 \pm 0.29$ (CMB+ $P_{\text{LRG}}(k)$) and $w_{\text{DE}}(z = 0.3) = -1.03 \pm 0.069$ (all four experiments combined). The latter is only slightly worse than the flat Λ CDM result.

In the near future new and larger galaxy catalogues, in which the redshifts are measured spectroscopically, like BOSS and HETDEX, or photometrically, like Pan-STARRS and DES, will become available, together with the new measurements of the CMB anisotropies from the Planck satellite (Ade et al., 2011). These datasets will enable scientists to improve the constraints presented in Chapter 5 even further. Some of these experiments are explicitly designed to extract from the data the maximum amount of information about dark energy. This will allow to exclude many classes of dark energy models or of modifications of general relativity. In order to use the full information from the power of these new large scale observations and to avoid introducing systematic effects, accurate models of the large scale distribution, scale dependent bias and redshift space distortions are necessary. In Chapter 4 I demonstrate that the model of equation (4.4) is accurate enough to describe the power spectrum shape also for surveys with volumes larger than available nowadays. However, extensions of the model with a more accurate treatment of the non-linear contribution and the explicit inclusion of bias and redshift space distortions would allow to include smaller scales in the analysis than now possible, helping to improve the quality of the cosmological constraints.

Appendix A

Power spectrum

Power spectra are typically computed using a Fast Fourier transform (FFT) algorithm in order to speed up the computation of the Fourier transform of the density field $\delta(\mathbf{x})$. Appendix A.1 describes the distortions in the power spectrum due to this procedure and reviews different methods to correct them. Appendix A.2 lists the basic equations of the FKP and PVP estimators proposed, respectively, by Feldman et al. (1994) and Percival et al. (2004), which allow to measure the power spectra of galaxy samples or mock simulations, taking into account their complex geometries.

A.1 Fast Fourier transform and corrections

The power spectrum is a statistical tool that allows to characterise gravitational clustering and is defined by equation (2.21a). For a finite number N of points tracing the underlying density field $\delta(\mathbf{k})$ in a limited volume V , the power spectrum becomes (Jing, 2005):

$$P(k) = \langle |\delta(\mathbf{k})|^2 \rangle - \frac{1}{\bar{n}}, \quad (\text{A.1})$$

with $\bar{n} = N/V$ the mean number density of particles. The term $1/\bar{n}$ is commonly called shot noise, is white, i.e. scale independent, and is given by the discretisation of the density field.

In order to increase the computation speed of the Fourier transform of the density field, I use a fast Fourier transform (FFT) algorithm. The drawback of the FFT is that it requires to convolve the density field $\delta(\mathbf{x})$ with a regular grid. The conversion of $\delta(\mathbf{x})$ into a density field $\delta^d(\mathbf{x})$ on a grid with cell size H is governed by the mass assignment scheme (MAS) function $W(\mathbf{x})$. When the power spectrum is computed convolving the density with the MAS, equation (A.1) becomes (Hockney & Eastwood, 1989)

$$\langle |\delta^d(\mathbf{k})|^2 \rangle = \sum_{\mathbf{n}} |W(\mathbf{k} + 2k_N \mathbf{n})|^2 P(\mathbf{k} + 2k_N \mathbf{n}) + \frac{1}{\bar{n}} \sum_{\mathbf{n}} |W(\mathbf{k} + 2k_N \mathbf{n})|^2, \quad (\text{A.2})$$

where \mathbf{n} is a three dimensional integer vector and $k_N = \pi/H$ is the Nyquist wave number and represent the larger value of \mathbf{k} that is possible to achieve with the FFT. $W(\mathbf{k})$ is the Fourier transform of the MAS.

Three MAS most commonly used are the nearest grid point (NGP), cloud in cell (CIC) and triangular shaped cloud (TSC). In three dimensions, they are defined by $W(\mathbf{x}) = \prod_{i=1}^3 W(x_i)$, where $x_i = x, y, z$ for $i = 1, 2, 3$ and:

$$W_{\text{NGP}}(x) = \begin{cases} 1 & |x| < 0.5, \\ 0 & |x| \geq 0.5, \end{cases} \quad (\text{A.3a})$$

$$W_{\text{CIC}}(x) = \begin{cases} 1 - |x| & |x| < 1, \\ 0 & |x| \geq 1, \end{cases} \quad (\text{A.3b})$$

$$W_{\text{TSC}}(x) = \begin{cases} 0.75 - x^2 & |x| < 0.5, \\ \frac{(1.5-|x|)^2}{2} & 0.5 \leq |x| < 1.5, \\ 0 & |x| \geq 1.5. \end{cases} \quad (\text{A.3c})$$

The Fourier transform of the MAS is given by

$$W(\mathbf{k}) = \left[\prod_{i=1}^3 \frac{\sin(\pi k_i/2k_N)}{\pi k_i/2k_N} \right]^p, \quad (\text{A.3d})$$

with p the order of the MAS ($p = 1$ for NGC, $p = 2$ for CIC and $p = 3$ for TSC).

The computation of the power spectrum with a FFT algorithm is divided roughly in the following steps :

1. creation of a density field assigning the particles to a grid using a chosen MAS;
2. Fourier transform of the gridded density field - I have performed this step using the free software FFTW;
3. spherical average of the density field in Fourier space to obtain the left hand side of equation(A.2);
4. solve equation (A.2) to obtain $P(k)$.

In Jing (2005), the last point is solved with an iterative procedure based on the assumption that the PS can be approximated by a power law at $k > k_N$. This assumption is a viable approximation when computing the power spectrum for dark matter, but it is not applicable when dealing with the halo-halo power spectrum (see Figure 4.1 and section 4.1.2). It is also possible to approximate the solution dividing the computed $\langle \delta^d(\mathbf{k}) \rangle$ by $W(\mathbf{k})$ (e.g. Angulo et al., 2008) or by $[\sum_{\mathbf{n}} |W(\mathbf{k} + 2k_N \mathbf{n})|^2]^{1/2}$ (e.g. Jeong & Komatsu, 2009). So the last two steps of the computation become:

- 3) correction of the amplitude of each Fourier mode for the effect of the MAS;

- 4) spherical average of the density field in Fourier space to obtain the left hand side of equation (A.2).

The recovered power spectra for the two corrections described above are

$$P_1(k) = \frac{\langle |\delta^d(\mathbf{k})|^2 \rangle}{W^2(\mathbf{k})} - \frac{1}{\bar{n}} = P(k) + \sum_{|\mathbf{n}| \neq 0} \left[\frac{|W(\mathbf{k}')|^2 P(\mathbf{k}')}{W^2(\mathbf{k})} + \frac{1}{\bar{n}} \frac{|W(\mathbf{k}')|^2}{W^2(\mathbf{k})} \right], \quad (\text{A.4a})$$

and

$$P_2(k) = \frac{\langle |\delta^d(\mathbf{k})|^2 \rangle}{\sum_{\mathbf{n}} |W(\mathbf{k} + 2k_N \mathbf{n})|^2} - \frac{1}{\bar{n}} = P(k) \times \left[1 + \frac{\sum_{|\mathbf{n}| \neq 0} |W(\mathbf{k}')|^2 P(\mathbf{k}')}{W^2(k) P(k)} - \frac{\sum_{|\mathbf{n}| \neq 0} |W(\mathbf{k}')|^2}{W^2(\mathbf{k})} + \dots \right], \quad (\text{A.4b})$$

where $\mathbf{k}' = \mathbf{k} + 2k_N \mathbf{n}$. Equation (A.4b) makes use of the fact that $\sum_{\mathbf{n}} |W(\mathbf{k}')|^2$ is finite and that for $|\mathbf{k}| \lesssim k_N$, $\sum_{|\mathbf{n}| \neq 0} |W(\mathbf{k}')| \leq |W(\mathbf{k})|$ and $P(\mathbf{k}') \leq P(\mathbf{k})$.

I test the impact of the MAS and corrections on the measured power spectrum. To do this I compare the power spectra computed with the standard Fourier transform (FT) and with the FFT algorithm. For the FFT I use a grid of 200^3 cells, filled using one of the three MAS. I also switch on and off the corrections in equations (A.4). In order to have the same number of modes in the two cases, the values of \mathbf{k} used for the FT calculation are the same as for the FFT. The power spectra for all the cases are computed in 48 logarithmic bins between $k = 0.01 h \text{ Mpc}^{-1}$ and $k_N = 0.47 h \text{ Mpc}^{-1}$. Figure A.1 shows the results of this test as the ratio between the FFT and the FT power spectra as function of the wave-number k . Panels *a*, *b* and *c* correspond, respectively, to the power spectra computed with NGP, CIC and TSC as MAS. In each panel the solid line is for the uncorrected power spectrum $P_{\text{unc}}(k) = \langle |\delta^d(k)|^2 \rangle - 1/\bar{n}$, the dashed line is for the $P_1(k)$ while the dash-dotted one is for $P_2(k)$. Since $\sum_{\mathbf{n}} |W(\mathbf{k} + 2k_N \mathbf{n})|^2 = 1$ in the NGP case, $P_2(k) = P_{\text{unc}}(k)$. The correction of the $\langle |\delta^d(k)|^2 \rangle$ increases drastically the agreement with the real $P(k)$, and the achieved accuracy is larger the higher the order of the MAS is. Furthermore the correction in equation (A.4b) works slightly better than equation (A.4a), because of the inclusion, in the correcting factor, of small contribution from large values of \mathbf{k} . In the light of these results, in this thesis I use the TSC as MAS correcting the power spectrum as in equation (A.4b). Choosing a very conservative limit, I assume that the FFT gives a correct answer for the power spectrum if $P_{\text{FFT}}(k)/P_{\text{FT}}(k) \lesssim 0.5\%$: this holds for $k \approx 0.314 h \text{ Mpc}^{-1} = 67\% k_N$, which is indicated by the vertical dotted line in Figure A.1.

A.2 The galaxy power spectrum: basic equations to account for the geometry

The procedure described in the previous appendix is largely independent of the geometry of the catalogue for which the power spectrum is computed. When the geometry is non

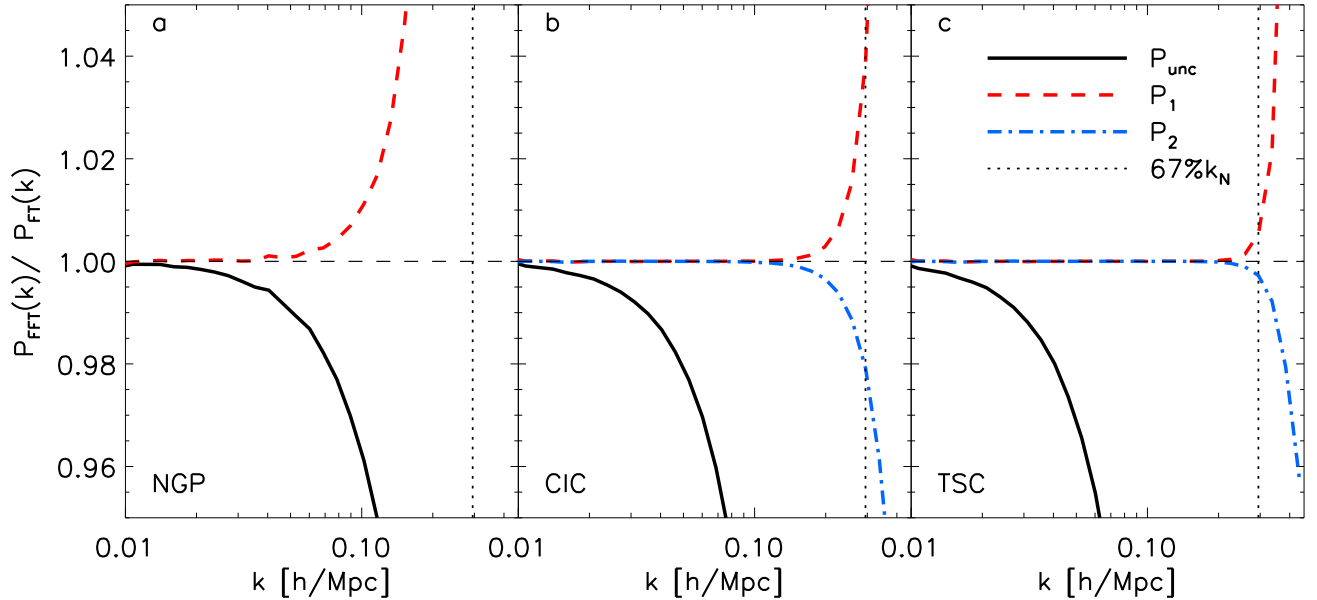


Figure A.1: Ratio between the power spectrum computed using the FFT and the one computed with the standard FT versus the wavenumber k . For clearness the error bars are not shown (for $k \gtrsim 0.03 h \text{ Mpc}^{-1}$ their amplitude is comparable with the thickness of the lines). The FFT is computed on a grid of 200^3 cells, that has been filled using the NGP (left panel), CIC (central panel) and TSC (right panel). The solid black line is the ratio between the uncorrected $P_{\text{FFT}}(k)$ and the $P_{\text{FT}}(k)$, while the dashed red line and the dash-dotted blue line indicate the $P_{\text{FFT}}(k)$ corrected as in equations (A.4a) and (A.4b) respectively. Since $\sum_{\mathbf{n}} |W(\mathbf{k} + 2k_{\text{N}}\mathbf{n})|^2 = 1$, $P_2(k)$ is equivalent to the uncorrected power spectrum in the NGP case. The dotted vertical line outlines the $67\%k_{\text{N}}$.

trivial, as it is for catalogues obtained from galaxy redshift surveys, the effects due the redshift distribution and the angular footprint need to be accounted for in order to measure meaningful power spectra and be able to compare them with theoretical models. In this thesis this is done thanks to the estimator proposed by Feldman et al. (1994), which alongside with the galaxy catalogue requires a random one created to have the same radial and angular distribution of the data. In this section I summarise the basic equations of the FKP and PVP estimators used to compute the power spectrum and the window function from galaxy surveys. PVP is a generalisation of FKP and takes in account the change of the galaxy bias with the luminosity of the galaxies (see e.g., Davis & Geller, 1976; Norberg et al., 2001, 2002; Zehavi et al., 2002; Phleps et al., 2006).

The observed power spectrum $P_o(k)$ is obtained from the squared average Fourier transform of the weighted density field defined by

$$\text{FKP: } F(\mathbf{x}) = \frac{1}{N} w(\mathbf{x}) [n_{\text{g}}(\mathbf{x}) - \alpha n_{\text{r}}(\mathbf{x})], \quad (\text{A.5a})$$

$$\text{PVP: } F(\mathbf{x}) = \frac{1}{N} \int dL \frac{w(\mathbf{x}, L)}{b(\mathbf{x}, L)} [n_g(\mathbf{x}, L) - \alpha n_r(\mathbf{x}, L)], \quad (\text{A.5b})$$

where $n_g(\mathbf{x}, L)$ and $n_r(\mathbf{x}, L)$ are the number density of galaxies and randoms of luminosity L at position \mathbf{x} . The corresponding quantities of equation (A.5a) can be obtained integrating over the luminosity. $w(\mathbf{x})$, $w(\mathbf{x}, L)$ are weighting functions and $b(\mathbf{x}, L)$, only PVP, is the bias, relative to a specific galaxy population with luminosity L_* . The normalisation N is defined by

$$\text{FKP: } N^2 = \int d^3x \bar{n}^2(\mathbf{x}) w^2(\mathbf{x}), \quad (\text{A.6a})$$

$$\text{PVP: } N^2 = \int d^3x \left[\int dL \bar{n}(\mathbf{x}, L) w(\mathbf{x}, L) \right]^2, \quad (\text{A.6b})$$

where $\bar{n}(\mathbf{x})$ and $\bar{n}(\mathbf{x}, L)$ are the mean expected number densities, i.e. in absence of clustering, of galaxies of luminosity L at position \mathbf{x} . Finally α is a constant introduced to match the two catalogues and is chosen requiring that¹ $\langle F(\mathbf{x}) \rangle = 0$:

$$\text{FKP: } \alpha = \frac{\int d^3x w(\mathbf{x}) n_g(\mathbf{x})}{\int d^3x w(\mathbf{x}) n_r(\mathbf{x})}, \quad (\text{A.7a})$$

$$\text{PVP: } \alpha = \frac{\int d^3x dL [w(\mathbf{x}, L)/b(\mathbf{x}, L)] n_g(\mathbf{x}, L)}{\int d^3x dL [w(\mathbf{x}, L)/b(\mathbf{x}, L)] n_r(\mathbf{x}, L)}. \quad (\text{A.7b})$$

The observed power spectrum can be then written for both estimators as:

$$P_o(\mathbf{k}) = \int \frac{dk'^3}{(2\pi)^3} P_t(\mathbf{k}') G^2(\mathbf{k} - \mathbf{k}') = \langle |F(\mathbf{k})|^2 \rangle - P_{\text{sn}}, \quad (\text{A.8})$$

where $P_t(\mathbf{k}')$ is the “true” underlying power spectrum, the shot noise P_{sn} is given by

$$\text{FKP: } P_{\text{sn}} = \frac{1 + \alpha}{N^2} \int d^3x \bar{n}(\mathbf{x}) w^2(\mathbf{x}), \quad (\text{A.9a})$$

$$\text{PVP: } P_{\text{sn}} = \frac{1 + \alpha}{N^2} \int d^3x dL \bar{n}(\mathbf{x}, L) \frac{w^2(\mathbf{x}, L)}{b^2(\mathbf{x}, L)} \quad (\text{A.9b})$$

and $G^2(k)$ is the window function, which encodes information about the survey geometry.

Applying the same procedure that brings from the definition of equations (A.5) to equation (A.8) to the field

$$\text{FKP: } \bar{G}(\mathbf{x}) = \frac{1}{N} \bar{n}(\mathbf{x}) w(\mathbf{x}), \quad (\text{A.10a})$$

$$\text{PVP: } \bar{G}(\mathbf{x}) = \frac{1}{N} \int dL \bar{n}(\mathbf{x}, L) w(\mathbf{x}, L). \quad (\text{A.10b})$$

¹In FKP, the authors use a definition of α such that $N = 1$.

it is possible to measure the window function as $G^2(k) = \langle |\bar{G}(k)|^2 \rangle - G_{\text{sn}}$, where the associated shot noise G_{sn} is

$$\text{FKP: } G_{\text{sn}} = \frac{1}{N^2} \int d^3x \bar{n}(\mathbf{x}) w^2(\mathbf{x}), \quad (\text{A.11a})$$

$$\text{PVP: } G_{\text{sn}} = \frac{1}{N^2} \int d^3x dL \bar{n}(\mathbf{x}, L) w^2(\mathbf{x}, L). \quad (\text{A.11b})$$

In Chapter 5, I use the weighting functions, designed to minimise the variance, proposed in FKP and Cole et al. (2005):

$$\text{FKP: } w(\mathbf{x}) = \frac{w_i}{1 + P(k)n(\mathbf{x})} \quad (\text{A.12a})$$

$$\text{PVP: } w(\mathbf{x}, L) = \frac{w_i b^2(\mathbf{x}, L)}{1 + P(k) \int dL b^2(\mathbf{x}, L) n(\mathbf{x}, L)}. \quad (\text{A.12b})$$

The intrinsic weight of the objects, w_i , can contain information about completeness and/or fibre collision (Zehavi et al., 2002; Masjedi et al., 2006). $P(k)$ is an estimate of the recovered power spectrum and it is usually substituted with a constant p_w , chosen in order to minimise the variance around the wave-number \bar{k} for which $P(\bar{k}) \sim p_w$.

Appendix **B**

Impact of weights on power spectra and cosmological constraints

In Appendices B.1 and B.2 I test the impact of the values of p_w and w_i , introduced at the end of Appendix A.2, and of the two estimators FKP and PVP, on the power spectra and window functions measured from the LRG and mock catalogues described in Section 5.1. Appendix B.3 describes the influence of p_w and w_i on the measured cosmological parameters.

B.1 Testing the luminous red galaxies power spectrum

Here I test the impact of different choices of p_w , w_i and estimator on the LRG power spectrum and window function. For both estimators, FKP and PVP, I use four values of $p_w = 40000, 10000, 4000, 0$. I also consider four different intrinsic weights: i) $w_i = 1$ (all the objects have equal weight), ii) $w_i = c$ (areas with low completeness have less weight than areas with higher one), iii) $w_i = fc$ (the loss of galaxies due to fibre collisions is compensated as described in Section 5.2.1) and iv) $w_i = c \times fc$ (both completeness and fibre collision corrections are applied).

The left panels of Figure B.1 show the differences in the power spectra measured with FKP (upper part) and PVP (lower part) estimators for the different choices of p_w and w_i . For clarity, in the figure I show only the combinations of $p_w = 40000, 0$ (red dashed and blue solid lines respectively) and $w_i = 1, fc$ (diamonds and up triangles, respectively). The shaded area shows the standard deviation as measured from the mock catalogues for $p_w = 40000$. All the power spectra have been divided by a non-wiggle one with the same cosmological parameters as the mock catalogues. Different choices of p_w change marginally the shape of the power spectrum. The results for $p_w = 10000, 4000$ fall in between the two extreme cases shown in the left panels of Figure B.1.

On the other hand, the correction for fibre collision has an important effect. When

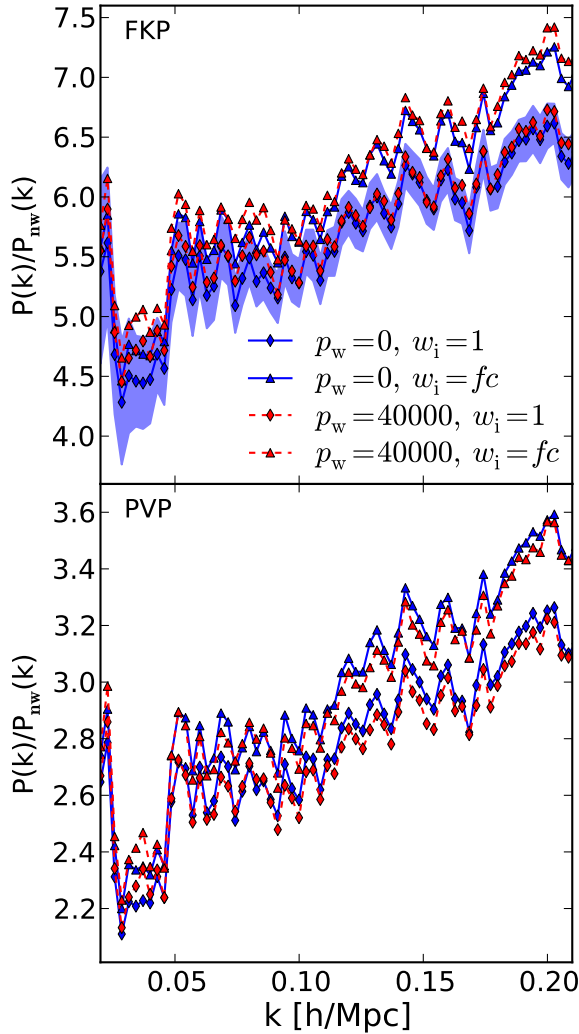


Figure B.1: *Left* panels: comparison between power spectra computed with $p_w = 40000, 0$ (red dashed and blue solid lines) and $w_i = 1, fc$ (diamonds and triangles) divided by a linear power spectrum without BAOs. The upper panel is for the FKP, the lower for PVP. The shaded area denotes the standard deviation computed from the mock catalogues using $p_w = 40000$. *Right* panel: ratio between power spectra computed the FKP and PVP estimators for $p_w = 40000, w_i = fc$. The shaded area shows the standard deviation computed from the mock catalogues with $p_w = 40000$. The dotted horizontal line is the mean of the ratio in the plotted interval. The other choices of p_w and w_i show similar behaviour.

obtaining spectra of crowded fields, not all the objects of interest can be targeted with a limited number of pointings. Because of this loss of objects, the amplitude of the highest peaks in the density field decreases, while the low density regions are unaffected. This causes the amplitude of the fluctuations, and consequently of the power spectrum, to be lower. I have indeed measured a few percent scale independent decrease in the amplitude of $\langle |F(\mathbf{k})|^2 \rangle$ (i.e. the power spectrum before subtracting the shot noise) in the case when fibre collision correction is not applied. This difference is visible in the large scale, low k , limit in the left two panels of Figure B.1 where the power spectrum with the fibre

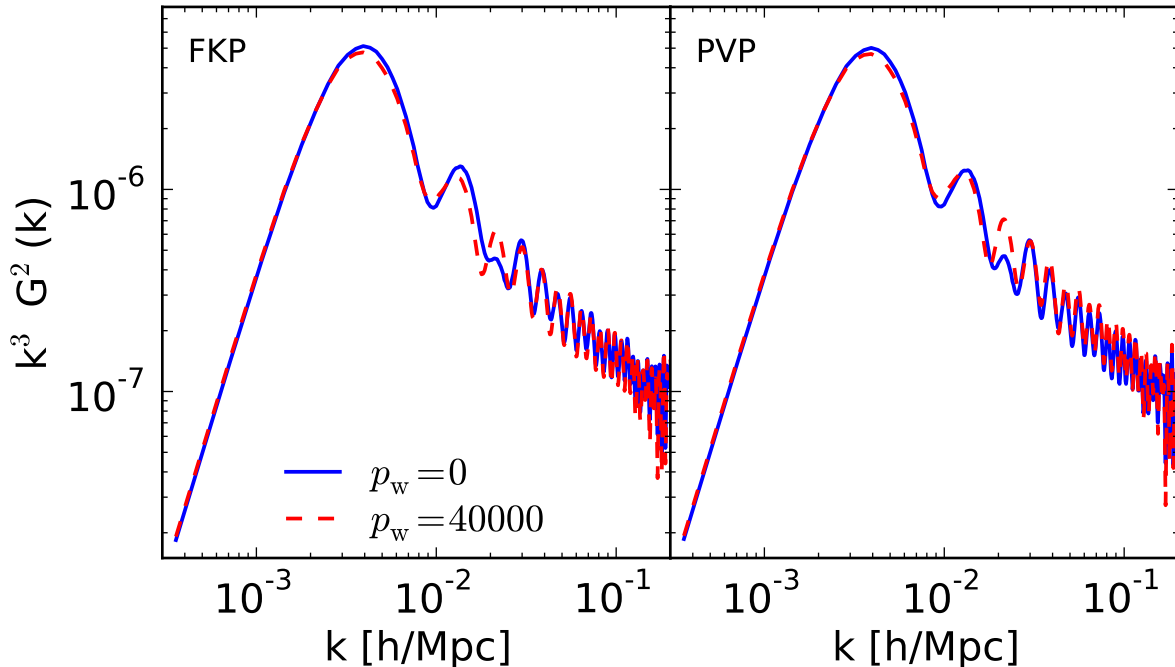


Figure B.2: Window functions $G^2(k)$ multiplied by the cube of the wave-number k as function of k for $p_w = 0, 40000$ (solid and dashed lines, respectively) for $w_i = 1$. The left panel is for FKP, the right for PVP.

collision (triangles) is always larger than the one without (diamonds). On the other hand the shot noise (equations A.9) depends on the expected non-clustered number density (\bar{n}) and the associated weights, which are not influenced (or influenced in a uniform way) by fibre collisions. This causes the shot noise to be the same in both cases, changing the shape of the final power spectrum $P_o(k)$. This effect is clearly visible in the small scale, large k , limit in the left panels of Figure B.1, where the fibre collision corrected power spectra become increasingly larger than the non corrected ones. I do not show the results when completeness correction is included, since the measured power spectra overlap almost exactly the non corrected ones. This is because both the galaxy and the random catalogues are weighted in the same way, therefore the density fluctuation field $F(\mathbf{k})$ is unchanged.

Comparing the two left panels of Figure B.1, it is clear that the choice of the estimator has a strong impact on the recovered power spectra: in the PVP case the amplitude is systematically lower than for FKP. The right panel of Figure B.1 shows the ratio of the power spectra computed with the latter estimator with respect to the one computed with the former for the case $p_w = 40000$, $w_i = fc$. As before, the shaded area corresponds to the standard deviation computed from the LasDamas catalogues. Although the amplitude is different, the relative bias between the two estimators is scale invariant in the range $0.02 h\text{Mpc}^{-1} \leq k \leq 0.2 h\text{Mpc}^{-1}$. This is expected from the fact that the galaxy sample that we use is almost volume limited and contains a very uniform population of galaxies.

Recently, Balaguera-Antolínez et al. (2011) have shown that, in volume limited mock

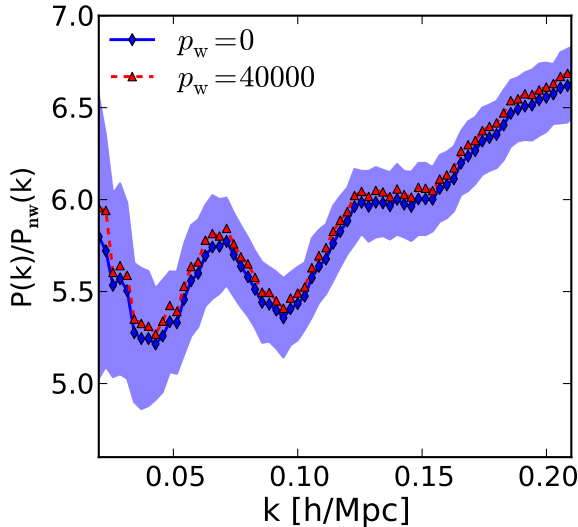


Figure B.3: Comparison between mean mock power spectra computed for $p_w = 40000, 0$ (red dashed with triangles and blue solid lines with diamonds respectively) divided by a power spectrum without oscillations. The shaded area denotes the standard deviation for $p_w = 40000$.

catalogues of the REFLEX II cluster survey, the power spectrum computed with the PVP estimator has higher correlations than the FKP one already at $k > 0.15 h \text{ Mpc}^{-1}$. Because of this and the scale independent relative bias, I can safely use the power spectra as estimated with FKP in order to constrain cosmological parameters.

The window function, describing only the radial and angular selection function of the survey, is not affected by fibre collision effect; on the other hand different choices of p_w and the completeness correction change the weights of equations (A.12), which influence the effective survey volume. As for the power spectrum, I do not measure differences when the completeness weighting is applied. Figure B.2 shows the “dimensionless” window function $k^3 G^2(k)$ computed with FKP (upper panel) and PVP (lower panel) for $p_w = 40000, 0$ (dashed and solid line respectively). Although the overall shape is similar, there are small differences in the oscillations due to different effective volumes in the two cases. The results for $p_w = 10000, 4000$ fall in between the two extreme cases. The difference between the FKP and PVP window functions are negligible. When convolving these window functions with a linear power spectrum as in equation (5.1), the differences in the range $0.02 h \text{ Mpc}^{-1} \leq k \leq 0.2 h \text{ Mpc}^{-1}$ are negligible.

B.2 Testing the power spectra of the mock catalogues

In order to test the impact of p_w on the results from the LasDamas mock catalogues, I compute the power spectra of the 160 mocks, their mean, standard deviation and covariance matrix for $p_w = 40000, 10000, 4000, 0$. Figure B.3 shows the mean power spectra computed for the two extreme cases: the only difference is a small change in amplitude, which confirms the findings of the previous section, i.e. that the impact of different p_w on the computed power spectrum is negligible. The shaded area denotes the standard deviation for $p_w = 40000$.

The choice of p_w has, however, a large effect on the errors. Figure B.4 shows the

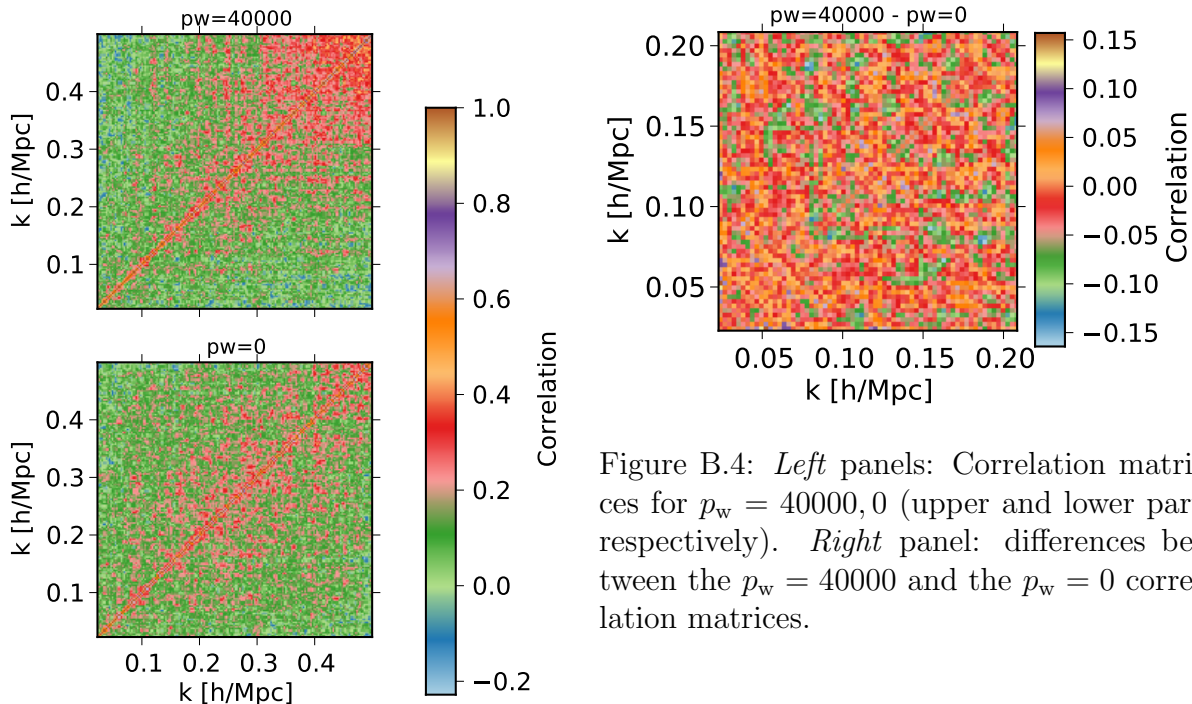


Figure B.4: *Left* panels: Correlation matrices for $p_w = 40000, 0$ (upper and lower part respectively). *Right* panel: differences between the $p_w = 40000$ and the $p_w = 0$ correlation matrices.

correlation matrix for $p_w = 40000$ (upper left panel) and $p_w = 0$ (lower left panel) and their difference (right panel). At $k \sim 0.1 h \text{Mpc}^{-1}$, for $p_w = 40000$ we measure that the correlation is systematically, although not significantly, lower than for $p_w = 0$. This is expected since, when using FKP, $P(k \sim 0.1) \simeq 40000$. At larger wave-number the power spectrum amplitude is smaller than at $k \sim 0.1 h \text{Mpc}^{-1}$ and the variance and the correlation are smaller for small values of p_w . This justifies my choice of using $p_w = 40000$ in our analysis, since the amplitude of the power spectrum is of this order in the range of scales I am interested in. If the analysis were centred on the small scale power spectrum or correlation function, a smaller value of p_w would be preferable.

B.3 Impact on the cosmological parameters

Here I test how the differences in the shape of the LRG power spectrum and the covariance matrix influence the cosmological parameters measured assuming the Λ CDM cosmology. I combine the LSS information with the WMAP7 data.

Contrary to expectations based on the results shown in Appendix B.1, the cosmological parameters are much more sensible to p_w than to w_i . For a fixed p_w the covariance matrix is the same and only the shape of the power spectrum changes. As this is not affected by the completeness corrections, also the cosmological constraints are insensitive to it. The fibre collision correction instead changes the bias, over which I marginalise analytically, without affecting the shot noise amplitude. Differences in the relative amplitude of the latter term

can be absorbed at least partially by the mode coupling amplitude A_{MC} , which is systematically, although not significantly, larger when the loss of galaxies due to fibre collisions is corrected for. Because of this, cosmological constraints remain almost unchanged for different w_i . Changes of p_w instead influence the covariance but only marginally the power spectrum. The differences in the former impact marginally the cosmological parameters, which differ by $0.5 - 1\sigma$, for $p_w = 40000$ and 0 . For example I obtain the dark energy equation of state parameter to be $w_{DE} = -1.02 \pm 0.13$ for $p_w = 40000$ and $w_{DE} = -1.10 \pm 0.14$ for $p_w = 0$.

Given the precision that is possible to achieve with the data used in Chapter 5, the differences just highlighted are not distinguishable from the uncertainties in the parameters. But in future, given the big improvements expected, these effects might become important and will need further analysis.

Bibliography

- Abazajian, K. N., Adelman-McCarthy, J. K., Agüeros, M. A. et al. “The Seventh Data Release of the Sloan Digital Sky Survey”. 2009, *ApJS*, 182, 543. [arXiv:0812.0649](#).
- Abbott, T., Aldering, G., Annis, J. et al. “The Dark Energy Survey”. 2005, *ArXiv Astrophysics e-prints*. [arXiv:astro-ph/0510346](#).
- Ade, P. A. R., Aghanim, N., Arnaud, M. et al. “Planck Early Results: The Planck mission”. 2011, *ArXiv e-prints*. [arXiv:1101.2022](#).
- Albrecht, A., Bernstein, G., Cahn, R. et al. “Report of the Dark Energy Task Force”. 2006, *ArXiv Astrophysics e-prints*. [arXiv:astro-ph/0609591](#).
- Amanullah, R., Lidman, C., Rubin, D. et al. “Spectra and Hubble Space Telescope Light Curves of Six Type Ia Supernovae at $0.511 < z < 1.12$ and the Union2 Compilation”. 2010, *ApJ*, 716, 712. [arXiv:1004.1711](#).
- Angulo, R. E., Baugh, C. M., Frenk, C. S. & Lacey, C. G. “The detectability of baryonic acoustic oscillations in future galaxy surveys”. 2008, *MNRAS*, 383, 755. [arXiv:astro-ph/0702543](#).
- Balaguera-Antolínez, A., Sánchez, A. G., Böhringer, H., Collins, C., Guzzo, L. & Phleps, S. “The REFLEX II galaxy cluster survey: power spectrum analysis”. 2011, *MNRAS*, 413, 386. [arXiv:1012.1322](#).
- Bardeen, J. “Gauge-invariant cosmological perturbations”. 1980, *Phys. Rev. D*, 22, 1882.
- Baumgart, D. J. & Fry, J. N. “Fourier spectra of three-dimensional data”. 1991, *ApJ*, 375, 25.
- Berlind, A. A. & Weinberg, D. H. “The Halo Occupation Distribution: Toward an Empirical Determination of the Relation between Galaxies and Mass”. 2002, *ApJ*, 575, 587. [arXiv:astro-ph/0109001](#).

- Bernardeau, F., Colombi, S., Gaztanaga, E. & Scoccimarro, R. “Large-scale structure of the Universe and cosmological perturbation theory”. 2002, *Phys. R.*, 367, 1.
- Blake, C. & Glazebrook, K. “Probing Dark Energy Using Baryonic Oscillations in the Galaxy Power Spectrum as a Cosmological Ruler”. 2003, *ApJ*, 594, 665. [arXiv:astro-ph/0301632](#).
- Blake, C., Davis, T., Poole, G. et al. “The WiggleZ Dark Energy Survey: testing the cosmological model with baryon acoustic oscillations at $z=0.6$ ”. 2011, *ArXiv e-prints*. [arXiv:1105.2862](#).
- Brown, M. L., Ade, P., Bock, J. et al. “Improved Measurements of the Temperature and Polarization of the Cosmic Microwave Background from QUaD”. 2009, *ApJ*, 705, 978. [arXiv:0906.1003](#).
- Cabré, A. & Gaztañaga, E. “Clustering of luminous red galaxies - I. Large-scale redshift-space distortions”. 2009a, *MNRAS*, 393, 1183. [arXiv:0807.2460](#).
- Cabré, A. & Gaztañaga, E. “Clustering of luminous red galaxies - II. Small-scale redshift-space distortions”. 2009b, *MNRAS*, 396, 1119. [arXiv:0807.2461](#).
- Carlson, J., White, M. & Padmanabhan, N. “Critical look at cosmological perturbation theory techniques”. 2009, *Ph. Rv. D*, 80, 043531. [arXiv:0905.0479](#).
- Carnero, A., Sanchez, E., Crocce, M., Cabre, A. & Gaztanaga, E. “Clustering of Photometric Luminous Red Galaxies II: Cosmological Implications from the Baryon Acoustic Scale”. 2011, *ArXiv e-prints*. [arXiv:1104.5426](#).
- Casas-Miranda, R., Mo, H. J., Sheth, R. K. & Boerner, G. “On the distribution of haloes, galaxies and mass”. 2002, *MNRAS*, 333, 730. [arXiv:astro-ph/0105008](#).
- Christensen, N. & Meyer, R. “Bayesian Methods for Cosmological Parameter Estimation from Cosmic Microwave Background Measurements”. 2000, *preprint (ArXiv:astro-ph/0006401)*. [arXiv:astro-ph/0006401](#).
- Chuang, C.-H., Wang, Y. & Hemantha, M. D. P. “A Robust Distance Measurement and Dark Energy Constraints from the Spherically-Averaged Correlation Function of Sloan Digital Sky Survey Luminous Red Galaxies”. 2010, *ArXiv e-prints*. [arXiv:1008.4822](#).
- Cole, S., Percival, W. J., Peacock, J. A. et al. “The 2dF Galaxy Redshift Survey: power-spectrum analysis of the final data set and cosmological implications”. 2005, *MNRAS*, 362, 505. [arXiv:astro-ph/0501174](#).
- Coles, P. & Jones, B. “A lognormal model for the cosmological mass distribution”. 1991, *MNRAS*, 248, 1.

- Colless, M., Peterson, B. A., Jackson, C. et al. “The 2dF Galaxy Redshift Survey: Final Data Release”. 2003, *ArXiv Astrophysics e-prints*. arXiv:astro-ph/0306581.
- Cooray, A. & Sheth, R. “Halo models of large scale structure”. 2002, *Phys. R.*, 372, 1. arXiv:astro-ph/0206508.
- Copeland, E. J., Sami, M. & Tsujikawa, S. “Dynamics of Dark Energy”. 2006, *International Journal of Modern Physics D*, 15, 1753. arXiv:hep-th/0603057.
- Crocce, M. & Scoccimarro, R. “Renormalized cosmological perturbation theory”. 2006a, *Phys. Rev. D*, 73, 063519.
- Crocce, M. & Scoccimarro, R. “Memory of initial conditions in gravitational clustering”. 2006b, *Phys. Rev. D*, 73, 063520. arXiv:astro-ph/0509419.
- Crocce, M. & Scoccimarro, R. “Nonlinear evolution of baryon acoustic oscillations”. 2008, *Phys. Rev. D*, 77, 2, 023533. arXiv:0704.2783.
- Crocce, M., Cabré, A. & Gaztañaga, E. “Modelling the angular correlation function and its full covariance in photometric galaxy surveys”. 2011, *MNRAS*, 385. arXiv:1004.4640.
- Croton, D. J., Gao, L. & White, S. D. M. “Halo assembly bias and its effects on galaxy clustering”. 2007, *MNRAS*, 374, 1303. arXiv:astro-ph/0605636.
- Dalal, N., White, M., Bond, J. R. & Shirokov, A. “Halo Assembly Bias in Hierarchical Structure Formation”. 2008, *ApJ*, 687, 12. arXiv:0803.3453.
- Davis, M. & Geller, M. J. “Galaxy Correlations as a Function of Morphological Type”. 1976, *ApJ*, 208, 13.
- Davis, M., Efstathiou, G., Frenk, C. S. & White, S. D. M. “The evolution of large-scale structure in a universe dominated by cold dark matter”. 1985, *ApJ*, 292, 371.
- Dodelson, S. *Modern Cosmology*. Academic Press, 2003.
- Drinkwater, M. J., Jurek, R. J., Blake, C. et al. “The WiggleZ Dark Energy Survey: survey design and first data release”. 2010, *MNRAS*, 401, 1429. arXiv:0911.4246.
- Dunkley, J., Komatsu, E., Nolta, M. R. et al. “Five-Year Wilkinson Microwave Anisotropy Probe Observations: Likelihoods and Parameters from the WMAP Data”. 2009, *ApJS*, 180, 306. arXiv:0803.0586.
- Durrer, R. “Gauge Invariant Cosmological Perturbation Theory”. 1994, *Fundamentals of Cosmic Physics*, 15, 209.
- Efstathiou, G., Kaiser, N., Saunders, W., Lawrence, A., Rowan-Robinson, M., Ellis, R. S. & Frenk, C. S. “Largescale Clustering of IRAS Galaxies”. 1990, *MNRAS*, 247, 10P.

- Efstathiou, G., Moody, S., Peacock, J. A. et al. “Evidence for a non-zero Λ and a low matter density from a combined analysis of the 2dF Galaxy Redshift Survey and cosmic microwave background anisotropies”. 2002, *MNRAS*, 330, L29. [arXiv:astro-ph/0109152](#).
- Einstein, A. “Die Feldgleichungen der Gravitation”. 1915, *Sitzungsberichte der Königlich Preussischen Akademie der Wissenschaften*, 844–847.
- Einstein, A. “Die Grundlage der allgemeinen Relativitätstheorie”. 1916, *AnP*, 354, 769.
- Einstein, A. “Kosmologische Betrachtungen zur allgemeinen Relativitätstheorie”. 1917, *Sitzungsberichte der Königlich Preussischen Akademie der Wissenschaften*, 142–152.
- Eisenstein, D. J. & Hu, W. “Baryonic Features in the Matter Transfer Function”. 1998, *ApJ*, 496, 605. [arXiv:astro-ph/9709112](#).
- Eisenstein, D. J. & Hu, W. “Power Spectra for Cold Dark Matter and Its Variants”. 1999, *ApJ*, 511, 5. [arXiv:astro-ph/9710252](#).
- Eisenstein, D. J., Annis, J., Gunn, J. E. et al. “Spectroscopic Target Selection for the Sloan Digital Sky Survey: The Luminous Red Galaxy Sample”. 2001, *AJ*, 122, 2267. [arXiv:astro-ph/0108153](#).
- Eisenstein, D. J., Zehavi, I., Hogg, D. W. et al. “Detection of the Baryon Acoustic Peak in the Large-Scale Correlation Function of SDSS Luminous Red Galaxies”. 2005, *ApJ*, 633, 560. [arXiv:astro-ph/0501171](#).
- Eisenstein, D. J., Weinberg, D. H., Agol, E. et al. “SDSS-III: Massive Spectroscopic Surveys of the Distant Universe, the Milky Way Galaxy, and Extra-Solar Planetary Systems”. 2011, *ArXiv e-prints*. [arXiv:1101.1529](#).
- Fang, W., Hu, W. & Lewis, A. “Crossing the phantom divide with parametrized post-Friedmann dark energy”. 2008, *Phys. Rev. D*, 78, 8, 087303. [arXiv:0808.3125](#).
- Feldman, H. A., Kaiser, N. & Peacock, J. A. “Power-spectrum analysis of three-dimensional redshift surveys”. 1994, *ApJ*, 426, 23. [arXiv:astro-ph/9304022](#).
- Fixsen, D. J., Cheng, E. S., Gales, J. M., Mather, J. C., Shafer, R. A. & Wright, E. L. “The Cosmic Microwave Background Spectrum from the Full COBE FIRAS Data Set”. 1996, *ApJ*, 473, 576. [arXiv:astro-ph/9605054](#).
- Friedmann, A. “Über die Krümmung des Raumes”. 1922, *Zeitschrift für Physik*, 10, 377.
- Friedmann, A. “Über die Möglichkeit einer Welt mit konstanter negativer Krümmung des Raumes”. 1924, *Zeitschrift für Physik*, 21, 326.
- Frigo, M. & Johnson, S. G. “The design and implementation of FFTW3”. 2005, *Proceedings of the IEEE*, 93, 216.

- Fry, J. N. & Gaztanaga, E. “Biasing and hierarchical statistics in large-scale structure”. 1993, *ApJ*, 413, 447. [arXiv:astro-ph/9302009](#).
- Gaztañaga, E., Cabré, A. & Hui, L. “Clustering of luminous red galaxies - IV. Baryon acoustic peak in the line-of-sight direction and a direct measurement of $H(z)$ ”. 2009, *MNRAS*, 399, 1663. [arXiv:0807.3551](#).
- Gelman, A. & Rubin, D. “Inference from iterative simulation using multiple sequences”. 1992, *Stat. Sci.*, 7, 457.
- Gilks, W. R., Richardson, S. & J., S. D. *Markov Chain Monte Carlo Methods in Practice*. Chapman and Hall, London, UK, 1996.
- Gong, Y. & Wang, A. “Reconstruction of the deceleration parameter and the equation of state of dark energy”. 2007, *Phys. Rev. D*, 75, 4, 043520. [arXiv:astro-ph/0612196](#).
- Guy, J., Astier, P., Baumont, S. et al. “SALT2: using distant supernovae to improve the use of type Ia supernovae as distance indicators”. 2007, *A&A*, 466, 11. [arXiv:astro-ph/0701828](#).
- Guzik, J., Bernstein, G. & Smith, R. E. “Systematic effects in the sound horizon scale measurements”. 2007, *MNRAS*, 375, 1329. [arXiv:astro-ph/0605594](#).
- Hamilton, A. J. S., Rimes, C. D. & Scoccimarro, R. “On measuring the covariance matrix of the non-linear power spectrum from simulations”. 2006, *MNRAS*, 371, 1188. [arXiv:astro-ph/0511416](#).
- Hicken, M., Wood-Vasey, W. M., Blondin, S., Challis, P., Jha, S., Kelly, P. L., Rest, A. & Kirshner, R. P. “Improved Dark Energy Constraints from ~ 100 New CfA Supernova Type Ia Light Curves”. 2009, *ApJ*, 700, 1097. [arXiv:0901.4804](#).
- Hill, G. J., Gebhardt, K., Komatsu, E. & MacQueen, P. J. “The Hobby-Eberly Telescope Dark Energy Experiment”. In R. E. Allen, D. V. Nanopoulos, & C. N. Pope, editor, “The New Cosmology: Conference on Strings and Cosmology”, volume 743 of *American Institute of Physics Conference Series*. 2004 224–233.
- Hinshaw, G., Spergel, D. N., Verde, L. et al. “First-Year Wilkinson Microwave Anisotropy Probe (WMAP) Observations: The Angular Power Spectrum”. 2003, *ApJS*, 148, 135. [arXiv:astro-ph/0302217](#).
- Hockney, R. W. & Eastwood, J. W. *Computer Simulation Using Particles*. Taylor & Francis, 1989.
- Holsclaw, T., Alam, U., Sansó, B., Lee, H., Heitmann, K., Habib, S. & Higdon, D. “Non-parametric reconstruction of the dark energy equation of state”. 2010, *Phys. Rev. D*, 82, 10, 103502. [arXiv:1009.5443](#).

- Hu, W., Fukugita, M., Zaldarriaga, M. & Tegmark, M. “Cosmic Microwave Background Observables and Their Cosmological Implications”. 2001, *ApJ*, 549, 669. [arXiv:astro-ph/0006436](#).
- Hu, W. & Haiman, Z. “Redshifting rings of power”. 2003, *Phys. Rev. D*, 68, 6, 063004. [arXiv:astro-ph/0306053](#).
- Hu, W. & Jain, B. “Joint galaxy-lensing observables and the dark energy”. 2004, *Phys. Rev. D*, 70, 4, 043009. [arXiv:astro-ph/0312395](#).
- Hubble, E. “A Relation between Distance and Radial Velocity among Extra-Galactic Nebulae”. 1929, *Proceedings of the National Academy of Science*, 15, 168.
- Huff, E., Schulz, A. E., White, M., Schlegel, D. J. & Warren, M. S. “Simulations of baryon oscillations”. 2007, *APh*, 26, 351. [arXiv:astro-ph/0607061](#).
- Huterer, D. & Turner, M. S. “Probing dark energy: Methods and strategies”. 2001, *Phys. Rev. D*, 64, 12, 123527. [arXiv:astro-ph/0012510](#).
- Huterer, D. & Starkman, G. “Parametrization of Dark-Energy Properties: A Principal-Component Approach”. 2003, *Physical Review Letters*, 90, 3, 031301. [arXiv:astro-ph/0207517](#).
- Jackson, J. C. “A critique of Rees’s theory of primordial gravitational radiation”. 1972, *MNRAS*, 156, 1P.
- Jarosik, N., Bennett, C. L., Dunkley, J. et al. “Seven-year Wilkinson Microwave Anisotropy Probe (WMAP) Observations: Sky Maps, Systematic Errors, and Basic Results”. 2011, *ApJS*, 192, 14. [arXiv:1001.4744](#).
- Jenkins, A., Frenk, C. S., White, S. D. M., Colberg, J. M., Cole, S., Evrard, A. E., Couchman, H. M. P. & Yoshida, N. “The mass function of dark matter haloes”. 2001, *MNRAS*, 321, 372. [arXiv:astro-ph/0005260](#).
- Jennings, E., Baugh, C. M. & Pascoli, S. “Modelling redshift space distortions in hierarchical cosmologies”. 2011, *MNRAS*, 410, 2081. [arXiv:1003.4282](#).
- Jeong, D. & Komatsu, E. “Perturbation Theory Reloaded: Analytical Calculation of Nonlinearity in Baryonic Oscillations in the RealSpace Matter Power Spectrum”. 2006, *ApJ*, 651, 619.
- Jeong, D. & Komatsu, E. “Perturbation Theory Reloaded. II. Nonlinear Bias, Baryon Acoustic Oscillations, and Millennium Simulation in Real Space”. 2009, *ApJ*, 691, 569.
- Jha, S., Riess, A. G. & Kirshner, R. P. “Improved Distances to Type Ia Supernovae with Multicolor Light-Curve Shapes: MLCS2k2”. 2007, *ApJ*, 659, 122. [arXiv:astro-ph/0612666](#).

- Jing, Y. P. “Correcting for the Alias Effect When Measuring the Power Spectrum Using a Fast Fourier Transform”. 2005, *ApJ*, 620, 559. [arXiv:astro-ph/0409240](#).
- Jones, W. C., Ade, P. A. R., Bock, J. J. et al. “A Measurement of the Angular Power Spectrum of the CMB Temperature Anisotropy from the 2003 Flight of BOOMERANG”. 2006, *ApJ*, 647, 823. [arXiv:astro-ph/0507494](#).
- Kaiser, N. “Clustering in real space and in redshift space”. 1987, *MNRAS*, 227, 1.
- Kaiser, N., Aussel, H., Burke, B. E. et al. “Pan-STARRS: A Large Synoptic Survey Telescope Array”. In J. A. Tyson & S. Wolff, editor, “Society of Photo-Optical Instrumentation Engineers (SPIE) Conference Series”, volume 4836 of *Presented at the Society of Photo-Optical Instrumentation Engineers (SPIE) Conference*. 2002 154–164.
- Kazin, E. A., Blanton, M. R., Scoccimarro, R. et al. “The Baryonic Acoustic Feature and Large-Scale Clustering in the Sloan Digital Sky Survey Luminous Red Galaxy Sample”. 2010, *ApJ*, 710, 1444. [arXiv:0908.2598](#).
- Kessler, R., Becker, A. C., Cinabro, D. et al. “First-Year Sloan Digital Sky Survey-II Supernova Results: Hubble Diagram and Cosmological Parameters”. 2009, *ApJS*, 185, 32. [arXiv:0908.4274](#).
- Kodama, H. & Sasaki, M. “Cosmological Perturbation Theory”. 1984, *Prog. of Theor. Phys. Supplement*, 78, 1.
- Komatsu, E., Dunkley, J., Nolta, M. R. et al. “Five-Year Wilkinson Microwave Anisotropy Probe Observations: Cosmological Interpretation”. 2009, *ApJS*, 180, 330. [arXiv:0803.0547](#).
- Komatsu, E., Smith, K. M., Dunkley, J. et al. “Seven-year Wilkinson Microwave Anisotropy Probe (WMAP) Observations: Cosmological Interpretation”. 2011, *ApJS*, 192, 18. [arXiv:1001.4538](#).
- Kowalski, M., Rubin, D., Aldering, G. et al. “Improved Cosmological Constraints from New, Old, and Combined Supernova Data Sets”. 2008, *ApJ*, 686, 749. [arXiv:0804.4142](#).
- Kuo, C. L., Ade, P. A. R., Bock, J. J. et al. “Improved Measurements of the CMB Power Spectrum with ACBAR”. 2007, *ApJ*, 664, 687. [arXiv:astro-ph/0611198](#).
- Larson, D., Dunkley, J., Hinshaw, G. et al. “Seven-year Wilkinson Microwave Anisotropy Probe (WMAP) Observations: Power Spectra and WMAP-derived Parameters”. 2011, *ApJS*, 192, 16. [arXiv:1001.4635](#).
- Laureijs, R. “Euclid Assessment Study Report for the ESA Cosmic Visions”. 2009, *ArXiv e-prints*. [arXiv:0912.0914](#).

- Lemaître, G. “Un Univers homogène de masse constante et de rayon croissant rendant compte de la vitesse radiale des nébuleuses extra-galactiques”. 1927, *Annales de la Societe Scietifique de Bruxelles*, 47, 49.
- Lewis, A., Challinor, A. & Lasenby, A. “Efficient Computation of Cosmic Microwave Background Anisotropies in Closed Friedmann-Robertson-Walker Models”. 2000, *ApJ*, 538, 473. [arXiv:astro-ph/9911177](#).
- Lewis, A. & Bridle, S. “Cosmological parameters from CMB and other data: A Monte Carlo approach”. 2002, *Phys. Rev. D*, 66, 10, 1.
- Liddle, A. R. “An Introduction to Cosmological Inflation”. In A. Masiero, G. Senjanovic, & A. Smirnov, editor, “High Energy Physics and Cosmology, 1998 Summer School”, 1999, 260. [arXiv:astro-ph/9901124](#).
- Liddle, A. & Lyth, D. *Cosmological inflation and large-scale structure*. Cambridge University Press, 2000.
- Linder, E. V. “Exploring the Expansion History of the Universe”. 2003, *Phys. Rev. Letters*, 90, 9, 091301. [arXiv:astro-ph/0208512](#).
- MacTavish, C. J., Ade, P. A. R., Bock, J. J. et al. “Cosmological Parameters from the 2003 Flight of BOOMERANG”. 2006, *ApJ*, 647, 799. [arXiv:astro-ph/0507503](#).
- Manera, M. & Gaztanaga, E. “The Local Bias Model in the Large Scale Halo Distribution”. 2009, *ArXiv e-prints*. [arXiv:0912.0446](#).
- Masjedi, M., Hogg, D. W., Cool, R. J. et al. “Very Small Scale Clustering and Merger Rate of Luminous Red Galaxies”. 2006, *ApJ*, 644, 54. [arXiv:astro-ph/0512166](#).
- Matarrese, S. & Pietroni, M. “Resumming cosmic perturbations”. 2007, *JCAP*, 6, 26. [arXiv:astro-ph/0703563](#).
- Matarrese, S. & Pietroni, M. “Baryonic Acoustic Oscillations via the Renormalization Group”. 2008, *Mod. Phys. L. A*, 23, 25. [arXiv:astro-ph/0702653](#).
- Matsubara, T. “Correlation Function in Deep Redshift Space as a Cosmological Probe”. 2004, *ApJ*, 615, 573. [arXiv:astro-ph/0408349](#).
- Matsubara, T. “Resumming cosmological perturbations via the Lagrangian picture: One-loop results in real space and in redshift space”. 2008a, *Phys. Rev. D*, 77, 6, 063530. [arXiv:0711.2521](#).
- Matsubara, T. “Nonlinear perturbation theory with halo bias and redshift-space distortions via the Lagrangian picture”. 2008b, *Phys. Rev. D*, 78, 8, 083519. [arXiv:0807.1733](#).
- McDonald, P. “Clustering of dark matter tracers: Renormalizing the bias parameters”. 2006, *Phys. Rev. D*, 74, 10, 103512.

- McDonald, P. “Dark matter clustering: A simple renormalization group approach”. 2007, *Phys. Rev. D*, 75, 4, 043514.
- Montesano, F., Sánchez, A. G. & Phleps, S. “A new model for the full shape of the large-scale power spectrum”. 2010, *MNRAS*, 408, 2397. [arXiv:1007.0755](#).
- Montesano, F., Sánchez, A. G. & Phleps, S. “Cosmological implications from the full shape of the large-scale power spectrum of the SDSS DR7 luminous red galaxies”. 2011, submitted to *MNRAS*. [arXiv:1107.4097](#).
- Montroy, T. E., Ade, P. A. R., Bock, J. J. et al. “A Measurement of the CMB $\langle EE \rangle$ Spectrum from the 2003 Flight of BOOMERANG”. 2006, *ApJ*, 647, 813. [arXiv:astro-ph/0507514](#).
- Moresco, M., Jimenez, R., Cimatti, A. & Pozzetti, L. “Constraining the expansion rate of the Universe using low-redshift ellipticals as cosmic chronometers”. 2011, *JCAP*, 3, 45. [arXiv:1010.0831](#).
- Norberg, P., Baugh, C. M., Hawkins, E. et al. “The 2dF Galaxy Redshift Survey: luminosity dependence of galaxy clustering”. 2001, *MNRAS*, 328, 64. [arXiv:astro-ph/0105500](#).
- Norberg, P., Baugh, C. M., Hawkins, E. et al. “The 2dF Galaxy Redshift Survey: the dependence of galaxy clustering on luminosity and spectral type”. 2002, *MNRAS*, 332, 827. [arXiv:astro-ph/0112043](#).
- Opik, E. “An estimate of the distance of the Andromeda Nebula.” 1922, *ApJ*, 55, 406.
- Peebles, P. J. & Ratra, B. “The cosmological constant and dark energy”. 2003, *Reviews of Modern Physics*, 75, 559. [arXiv:astro-ph/0207347](#).
- Percival, W. J., Sutherland, W., Peacock, J. A. et al. “Parameter constraints for flat cosmologies from cosmic microwave background and 2dFGRS power spectra”. 2002, *MNRAS*, 337, 1068. [arXiv:astro-ph/0206256](#).
- Percival, W. J., Verde, L. & Peacock, J. A. “Fourier analysis of luminosity-dependent galaxy clustering”. 2004, *MNRAS*, 347, 645. [arXiv:astro-ph/0306511](#).
- Percival, W. J., Cole, S., Eisenstein, D. J., Nichol, R. C., Peacock, J. A., Pope, A. C. & Szalay, A. S. “Measuring the Baryon Acoustic Oscillation scale using the Sloan Digital Sky Survey and 2dF Galaxy Redshift Survey”. 2007, *MNRAS*, 381, 1053. [arXiv:0705.3323](#).
- Percival, W. J., Reid, B. A., Eisenstein, D. J. et al. “Baryon acoustic oscillations in the Sloan Digital Sky Survey Data Release 7 galaxy sample”. 2010, *MNRAS*, 401, 2148. [arXiv:0907.1660](#).

- Perlmutter, S., Aldering, G., Goldhaber, G. et al. “Measurements of Omega and Lambda from 42 High-Redshift Supernovae”. 1999, *ApJ*, 517, 565. [arXiv:astro-ph/9812133](#).
- Phleps, S., Peacock, J. A., Meisenheimer, K. & Wolf, C. “Galaxy clustering from COMBO-17: the halo occupation distribution at $\langle z \rangle = 0.6$ ”. 2006, *A&A*, 457, 145. [arXiv:astro-ph/0506320](#).
- Piacentini, F., Ade, P. A. R., Bock, J. J. et al. “A Measurement of the Polarization-Temperature Angular Cross-Power Spectrum of the Cosmic Microwave Background from the 2003 Flight of BOOMERANG”. 2006, *ApJ*, 647, 833. [arXiv:astro-ph/0507507](#).
- Pietroni, M. “Flowing with time: a new approach to non-linear cosmological perturbations”. 2008, *JCAP*, 2008, 10, 036.
- Pillepich, A., Porciani, C. & Hahn, O. “Halo mass function and scale-dependent bias from N-body simulations with non-Gaussian initial conditions”. 2010, *MNRAS*, 402, 191. [arXiv:0811.4176](#).
- Press, W. H. & Schechter, P. “Formation of Galaxies and Clusters of Galaxies by Self-Similar Gravitational Condensation”. 1974, *ApJ*, 187, 425.
- Reichardt, C. L., Ade, P. A. R., Bock, J. J. et al. “High-Resolution CMB Power Spectrum from the Complete ACBAR Data Set”. 2009, *ApJ*, 694, 1200. [arXiv:0801.1491](#).
- Reid, B. A. & Spergel, D. N. “Constraining the Luminous Red Galaxy Halo Occupation Distribution Using Counts-In-Cylinders”. 2009, *ApJ*, 698, 143. [arXiv:0809.4505](#).
- Reid, B. A., Spergel, D. N. & Bode, P. “Luminous Red Galaxy Halo Density Field Reconstruction and Application to Large-scale Structure Measurements”. 2009, *ApJ*, 702, 249. [arXiv:0811.1025](#).
- Reid, B. A., Percival, W. J., Eisenstein, D. J. et al. “Cosmological constraints from the clustering of the Sloan Digital Sky Survey DR7 luminous red galaxies”. 2010a, *MNRAS*, 404, 60. [arXiv:0907.1659](#).
- Reid, B. A., Verde, L., Dolag, K., Matarrese, S. & Moscardini, L. “Non-Gaussian halo assembly bias”. 2010b, *JCAP*, 7, 13. [arXiv:1004.1637](#).
- Reid, B. A. & White, M. “Towards an accurate model of the redshift space clustering of halos in the quasilinear regime”. 2011, *ArXiv e-prints*. [arXiv:1105.4165](#).
- Riess, A. G., Filippenko, A. V., Challis, P. et al. “Observational Evidence from Supernovae for an Accelerating Universe and a Cosmological Constant”. 1998, *AJ*, 116, 1009. [arXiv:astro-ph/9805201](#).
- Riess, A. G., Strolger, L., Tonry, J. et al. “Type Ia Supernova Discoveries at $z > 1$ from the Hubble Space Telescope: Evidence for Past Deceleration and Constraints on Dark Energy Evolution”. 2004, *ApJ*, 607, 665. [arXiv:astro-ph/0402512](#).

- Riess, A. G., Macri, L., Casertano, S. et al. “A Redetermination of the Hubble Constant with the Hubble Space Telescope from a Differential Distance Ladder”. 2009, *ApJ*, 699, 539. [arXiv:0905.0695](#).
- Riess, A. G., Macri, L., Casertano, S. et al. “A 3% Solution: Determination of the Hubble Constant with the Hubble Space Telescope and Wide Field Camera 3”. 2011, *ApJ*, 730, 119. [arXiv:1103.2976](#).
- Samushia, L., Percival, W. J. & Raccanelli, A. “Interpreting large-scale redshift-space distortion measurements”. 2011, *ArXiv e-prints*. [arXiv:1102.1014](#).
- Sánchez, A. G., Baugh, C. M., Percival, W. J., Peacock, J. A., Padilla, N. D., Cole, S., Frenk, C. S. & Norberg, P. “Cosmological parameters from cosmic microwave background measurements and the final 2dF Galaxy Redshift Survey power spectrum”. 2006, *MNRAS*, 366, 189. [arXiv:astro-ph/0507583](#).
- Sánchez, A. G. & Cole, S. “The galaxy power spectrum: precision cosmology from large-scale structure?” 2008, *MNRAS*, 385, 830. [arXiv:0708.1517](#).
- Sánchez, A. G., Baugh, C. M. & Angulo, R. “What is the best way to measure baryonic acoustic oscillations?” 2008, *MNRAS*, 390, 1470. [arXiv:0804.0233](#).
- Sánchez, A. G., Crocce, M., Cabré, A., Baugh, C. M. & Gaztañaga, E. “Cosmological parameter constraints from SDSS luminous red galaxies: a new treatment of large-scale clustering”. 2009, *MNRAS*, 400, 1643. [arXiv:0901.2570](#).
- Schlegel, D., White, M. & Eisenstein, D. “The Baryon Oscillation Spectroscopic Survey: Precision measurement of the absolute cosmic distance scale”. In “astro2010: The Astronomy and Astrophysics Decadal Survey”, volume 2010 of *Astronomy*. 2009, 314. [arXiv:0902.4680](#).
- Soccimarro, R. “Redshift-space distortions, pairwise velocities, and nonlinearities”. 2004, *Phys. Rev. D*, 70, 8, 083007. [arXiv:astro-ph/0407214](#).
- Seo, H.-J. & Eisenstein, D. J. “Probing Dark Energy with Baryonic Acoustic Oscillations from Future Large Galaxy Redshift Surveys”. 2003, *ApJ*, 598, 720. [arXiv:astro-ph/0307460](#).
- Seo, H.-J. & Eisenstein, D. J. “Improved Forecasts for the Baryon Acoustic Oscillations and Cosmological Distance Scale”. 2007, *ApJ*, 665, 14. [arXiv:astro-ph/0701079](#).
- Seo, H.-J., Siegel, E. R., Eisenstein, D. J. & White, M. “Nonlinear Structure Formation and the Acoustic Scale”. 2008, *ApJ*, 686, 13. [arXiv:0805.0117](#).
- Serra, P., Cooray, A., Holz, D. E., Melchiorri, A., Pandolfi, S. & Sarkar, D. “No evidence for dark energy dynamics from a global analysis of cosmological data”. 2009, *Phys. Rev. D*, 80, 12, 121302. [arXiv:0908.3186](#).

- Seo, H.-J., Eckel, J., Eisenstein, D. J. et al. “High-precision Predictions for the Acoustic Scale in the Nonlinear Regime”. 2010, *ApJ*, 720, 1650. [arXiv:0910.5005](#).
- Sheth, R. K. & Tormen, G. “Large-scale bias and the peak background split”. 1999, *MNRAS*, 308, 119. [arXiv:astro-ph/9901122](#).
- Sheth, R. K., Mo, H. J. & Tormen, G. “Ellipsoidal collapse and an improved model for the number and spatial distribution of dark matter haloes”. 2001, *MNRAS*, 323, 1. [arXiv:astro-ph/9907024](#).
- Shoji, M., Jeong, D. & Komatsu, E. “Extracting Angular Diameter Distance and Expansion Rate of the Universe From Two-Dimensional Galaxy Power Spectrum at High Redshifts: Baryon Acoustic Oscillation Fitting Versus Full Modeling”. 2009, *ApJ*, 693, 1404. [arXiv:0805.4238](#).
- Sievers, J. L., Mason, B. S., Weintraub, L. et al. “Cosmological Results from Five Years of 30 GHz CMB Intensity Measurements with the Cosmic Background Imager”. 2009, *ArXiv e-prints*. [arXiv:0901.4540](#).
- Silk, J. “Cosmic Black-Body Radiation and Galaxy Formation”. 1968, *ApJ*, 151, 459.
- Smith, R. E., Peacock, J. A., Jenkins, A. et al. “Stable clustering, the halo model and non-linear cosmological power spectra”. 2003, *MNRAS*, 341, 1311. [arXiv:astro-ph/0207664](#).
- Smith, R. E., Scoccimarro, R. & Sheth, R. K. “Scale dependence of halo and galaxy bias: Effects in real space”. 2007, *Phys. Rev. D*, 75, 6, 063512. [arXiv:astro-ph/0609547](#).
- Smith, R. E., Scoccimarro, R. & Sheth, R. K. “Motion of the acoustic peak in the correlation function”. 2008, *Phys. Rev. D*, 77, 4, 043525. [arXiv:astro-ph/0703620](#).
- Smith, R. E. “Covariance of cross-correlations: towards efficient measures for large-scale structure”. 2009, *MNRAS*, 400, 851. [arXiv:0810.1960](#).
- Smith, R. E., Hernández-Montegudo, C. & Seljak, U. “Impact of scale dependent bias and nonlinear structure growth on the integrated Sachs-Wolfe effect: Angular power spectra”. 2009, *Phys. Rev. D*, 80, 6, 063528. [arXiv:0905.2408](#).
- Somogyi, G. & Smith, R. E. “Cosmological perturbation theory for baryons and dark matter: One-loop corrections in the renormalized perturbation theory framework”. 2010, *Phys. Rev. D*, 81, 023524.
- Spergel, D. N., Verde, L., Peiris, H. V. et al. “First-Year Wilkinson Microwave Anisotropy Probe (WMAP) Observations: Determination of Cosmological Parameters”. 2003, *ApJS*, 148, 175. [arXiv:astro-ph/0302209](#).

- Spergel, D. N., Bean, R., Doré, O. et al. “Three-Year Wilkinson Microwave Anisotropy Probe (WMAP) Observations: Implications for Cosmology”. 2007, *ApJS*, 170, 377. [arXiv:astro-ph/0603449](#).
- Sugiyama, N. “Cosmic Background Anisotropies in Cold Dark Matter Cosmology”. 1995, *ApJS*, 100, 281. [arXiv:astro-ph/9412025](#).
- Sullivan, M., Guy, J., Conley, A. et al. “SNLS3: Constraints on Dark Energy Combining the Supernova Legacy Survey Three Year Data with Other Probes”. 2011, *ArXiv e-prints*. [arXiv:1104.1444](#).
- Takahashi, R., Yoshida, N., Takada, M. et al. “Simulations of Baryon Acoustic Oscillations. II. Covariance Matrix of the Matter Power Spectrum”. 2009, *ApJ*, 700, 479. [arXiv:0902.0371](#).
- Taruya, A. & Hiramatsu, T. “A Closure Theory for Nonlinear Evolution of Cosmological Power Spectra”. 2008, *ApJ*, 674, 2, 617.
- Taruya, A., Nishimichi, T., Saito, S. & Hiramatsu, T. “Nonlinear evolution of baryon acoustic oscillations from improved perturbation theory in real and redshift spaces”. 2009, *Phys. Rev. D*, 80, 12, 123503. [arXiv:0906.0507](#).
- Taruya, A., Nishimichi, T. & Saito, S. “Baryon acoustic oscillations in 2D: Modeling redshift-space power spectrum from perturbation theory”. 2010, *Phys. Rev. D*, 82, 6, 063522. [arXiv:1006.0699](#).
- Tegmark, M., Silk, J. & Blanchard, A. “On the inevitability of reionization: Implications for cosmic microwave background fluctuations”. 1994, *ApJ*, 420, 484. [arXiv:astro-ph/9307017](#).
- Tegmark, M., Blanton, M. R., Strauss, M. A. et al. “The Three-Dimensional Power Spectrum of Galaxies from the Sloan Digital Sky Survey”. 2004, *ApJ*, 606, 702. [arXiv:astro-ph/0310725](#).
- Tinker, J. L. “Redshift-space distortions with the halo occupation distribution - II. Analytic model”. 2007, *MNRAS*, 374, 477. [arXiv:astro-ph/0604217](#).
- Tinker, J. L., Sheldon, E. S., Wechsler, R. H. et al. “Cosmological Constraints from Galaxy Clustering and the Mass-to-Number Ratio of Galaxy Clusters”. 2011, *ArXiv e-prints*. [arXiv:1104.1635](#).
- Tsujikawa, S. “Modified Gravity Models of Dark Energy”. In G. Wolschin, editor, “Lecture Notes in Physics, Berlin Springer Verlag”, volume 800 of *Lecture Notes in Physics, Berlin Springer Verlag*. 2010 99–145. [arXiv:1101.0191](#).
- Vikhlinin, A., Kravtsov, A. V., Burenin, R. A. et al. “Chandra Cluster Cosmology Project III: Cosmological Parameter Constraints”. 2009, *ApJ*, 692, 1060. [arXiv:0812.2720](#).

- Wang, Y. “Dark Energy Constraints from Baryon Acoustic Oscillations”. 2006, *ApJ*, 647, 1. [arXiv:astro-ph/0601163](#).
- Warren, M. S., Abazajian, K., Holz, D. E. & Teodoro, L. “Precision Determination of the Mass Function of Dark Matter Halos”. 2006, *ApJ*, 646, 881. [arXiv:astro-ph/0506395](#).
- Xu, X., White, M., Padmanabhan, N. et al. “A New Statistic for Analyzing Baryon Acoustic Oscillations”. 2010, *ApJ*, 718, 1224. [arXiv:1001.2324](#).
- York, D. G., Adelman, J., Anderson, J. E., Jr. et al. “The Sloan Digital Sky Survey: Technical Summary”. 2000, *AJ*, 120, 1579. [arXiv:astro-ph/0006396](#).
- Yoshikawa, K., Taruya, A., Jing, Y. P. & Suto, Y. “Nonlinear stochastic biasing of galaxies and dark halos in cosmological hydrodynamic simulations”. 2001, *ApJ*, 558, 2, 520.
- Zehavi, I., Blanton, M. R., Frieman, J. A. et al. “Galaxy Clustering in Early Sloan Digital Sky Survey Redshift Data”. 2002, *ApJ*, 571, 172. [arXiv:astro-ph/0106476](#).
- Zwicky, F. “On the Masses of Nebulae and of Clusters of Nebulae”. 1937, *ApJ*, 86, 217.

Acknowledgments

I would like thanks to Raul Angulo and Carlton Baugh for providing us with the L-BASICC II numerical simulations and the LasDamas project for releasing publicly the mock catalogues

Funding for the SDSS and SDSS-II has been provided by the Alfred P. Sloan Foundation, the Participating Institutions, the National Science Foundation, the U.S. Department of Energy, the National Aeronautics and Space Administration, the Japanese Monbukagakusho, the Max Planck Society, and the Higher Education Funding Council for England. The SDSS Web Site is <http://www.sdss.org/>.

The SDSS is managed by the Astrophysical Research Consortium for the Participating Institutions. The Participating Institutions are the American Museum of Natural History, Astrophysical Institute Potsdam, University of Basel, University of Cambridge, Case Western Reserve University, University of Chicago, Drexel University, Fermilab, the Institute for Advanced Study, the Japan Participation Group, Johns Hopkins University, the Joint Institute for Nuclear Astrophysics, the Kavli Institute for Particle Astrophysics and Cosmology, the Korean Scientist Group, the Chinese Academy of Sciences (LAMOST), Los Alamos National Laboratory, the Max-Planck-Institute for Astronomy (MPIA), the Max-Planck-Institute for Astrophysics (MPA), New Mexico State University, Ohio State University, University of Pittsburgh, University of Portsmouth, Princeton University, the United States Naval Observatory, and the University of Washington.

I acknowledge Carlton Baugh and Martin Crocce for their comments. I thank Raul Angulo, Martin Crocce, Eiichiro Komatsu, Shaun Cole and Andrés Balaguera-Antolínez for useful discussions. I thanks Lodovico Coccato, Maximilian Fabricius and Ralf Köhler for the technical help and Friedrich Röpke and Sandra Benitez for the clarifications about SNIa

For part of this work I have been supported through SFB-Transregio 33 “The Dark Universe” by the Deutsche Forschungsgemeinschaft (DFG).

Curriculum Vitae

Max-Planck-Institut für Extraterrestrische Physik
Giessenbachstrasse
85748 Garching
Germany
Phone: +49 (0)89 30000 3770
Fax: +49 (0)89 30000 3569
Email: montefra@mpe.mpg.de

Private address:
Gotthardstrasse 54
80689 München
Germany

Personal

Born on 18th November 1982 in Varese, Italy
Nationality: Italian

Current position

Max-Planck-Institut für Extraterrestrische Physik
Post-doctoral position in the “Optical and Interpretative Astronomy” group
November 2011 - present

Education

Ludwig–Maximilians–Universität, Munich, Germany
Max-Planck-Institut für Extraterrestrische Physik
Doctoral degree in Astronomy, 28th October 2011. Mark: *Magna cum Laude*
The full shape of the large-scale galaxy power spectrum: modelling and cosmological implications

Supervisors: Dr. Ariel Sánchez, Dr. Stephanie Phleps, Prof. Ralf Bender

Università degli Studi di Milano, Milano, Italy
Master degree in Physics, 11th July 2007. Mark: 109/110

Quintessence fluctuations and large scale structures in cosmology.

Supervisors: Prof. Carlo Baccigalupi (SISSA), Dr. Davide Maino

Università degli Studi di Milano, Milano, Italy

Bachelor degree in Physics, 16th September 2004. Mark: 110/110

Research

Research Interests

Modelling of the large scale power spectrum of matter and galaxy distribution. Extraction of cosmological information from the combination of the galaxy clustering with other experiments.

Publications

Montesano F., Sánchez A. G. & Phleps S., *Cosmological implications of the full shape of the large-scale power spectrum of the SDSS DR7 luminous red galaxies*, arXiv:1107.4097

Montesano F., Sánchez A. G. & Phleps S., *A new model for the full shape of the large-scale power spectrum*, MNRAS, 2010, 408, 2397

Conference and seminar contributions

Presentation: 07 June 2011; Excellence Cluster Research Area E Science Day, Garching, Germany; *Cosmological constraints from the large-scale power spectrum of the luminous red galaxies.*

Presentation: 24-26 March 2011; BOSS Collaboration Meeting, Croudcroft, NM, USA; *Cosmological constraints from the full shape of the power spectrum.*

Presentation: 23 February 2011; University Observatory Munich Colloquium, Munich, Germany; *Cosmological constraints from luminous red galaxies in the SDSS data release 7.*

Poster and presentation: 16th-18th September 2010; SDSSIII general meeting, Paris, France; *A new model for the full shape of the large scale non-linear power spectrum.*

Presentation: 14 June 2010; Excellence Cluster Research Area E Science Day, Garching, Germany; *Modelling the full shape of the matter power spectrum.*

Poster: 7-11 October 2008; 3rd Biennial Leopoldina Conference on Dark Energy, Munich, Germany; *BAO distortions in the Non Linear Power Spectrum.*

Schools attended

26-29 January 2009: Corse Grained Universe, Firenze, Italy

30 June - 4 July 2008: Cosmology: an astrophysical perspective, Heraklion, Crete, Greece

2-8 December 2007: First TRR33 Winter school: Theory for observers, Passo del Tonale, Italy

Conferences and workshops attended

13-16 August 2011, SDSSIII meeting, Nashville, TN, USA

27-29 July 2009: SDSSIII general meeting, Princeton, NJ, USA

Software skills

Computer programming

C/C++, Python, Bash, Fortran77/90, IDL, Gnuplot.

Productivity applications

L^AT_EX, iWork, Microsoft Office, OpenOffice.org

Operating systems

Mac OS X, Linux, Microsoft Windows

Languages

Common European Framework of Reference (CEF) level

Italian: mother tongue

English: proficient user

German: independent user

French: basic user

References

Prof. Carlo Baccigalupi, Astrophysics department, SISSA/ISAS, Trieste, Italy,
bacci@sissa.it

Prof. Ralf Bender, Max-Planck-Institut für Extraterrestrische Physik,
bender@mpe.mpg.de

Prof. Hans Böringer, Max-Planck-Institut für Extraterrestrische Physik,
hxb@mpe.mpg.de

Dr. Ariel Sánchez, Max-Planck-Institut für Extraterrestrische Physik,
arielsan@mpe.mpg.de